Dissertation
Tomasz Jüngst

Establishing and Improving Methods for Biofabrication

Dissertation zur Erlangung des naturwissenschaftlichen Doktorgrades der
Julius-Maximilians-Universität Würzburg

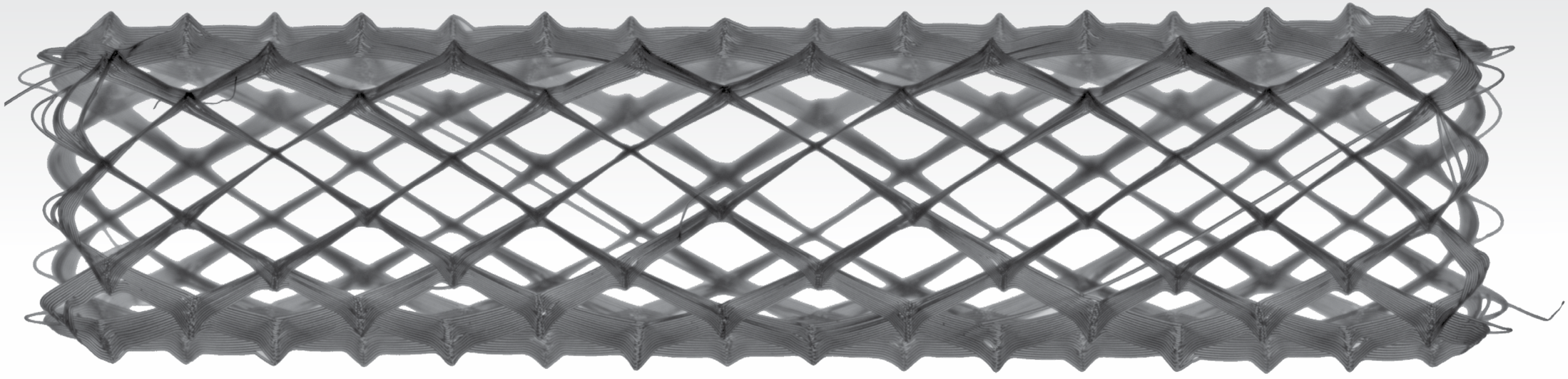

Establishing and Improving
Methods for Biofabrication

vorgelegt von
Tomasz Jüngst
aus Ostrów Wielkopolski

Würzburg 2018

Establishing and Improving Methods for Biofabrication

Dissertation zur Erlangung des naturwissenschaftlichen Doktorgrades der Julius-Maximilians-Universität Würzburg

vorgelegt von

Tomasz Konrad Jüngst

aus Ostrów Wielkopolski

Würzburg 2018

Eingereicht bei der Fakultät für Chemie und Pharmazie am

_____

Gutachter der schriftlichen Arbeit

1. Gutachter: _____
2. Gutachter: _____

Prüfer des öffentlichen Promotionskolloquiums

1. Prüfer: _____
2. Prüfer: _____
3. Prüfer: _____

Datum des öffentlichen Promotionskolloquiums

_____

Doktorurkunde ausgestellt am

_____

Table of Contents

Table of Contents

Table of Contents

Chapter 1

Scope of the thesis

Additive manufacturing (AM), also known as 3D printing, is a computer-controlled process that allows the creation of complex three-dimensional (3D) constructs in a layer-by-layer fashion based on digital models. The manufacturing process is comparable to the generation of a 3D computer tomography model from single 2D images. In AM, existing digital models are sliced into 2D print-patterns defining the print path for the manufacturing device. These slices are sent to the printer and, by assembling and joining each slice sequentially, complex 3D structures are created exploiting for example a localized solidification or melting of the material used to generate the constructs.[1] The main benefits of AM are the high flexibility of the process and the enormous freedom in geometrical design; it allows the creation of constructs not able to be manufactured by conventional, subtractive manufacturing techniques. Because of these benefits, AM is considered to be a leading technology for a new industrial revolution.[2] Although this revolution is just starting, 3D printing has already changed some niches of industrial production that strongly rely on flexibility and freedom in geometrical design such as prototyping and medical applications, especially where patient specific implants are needed. One example for such patient specific implants are already clinically applied metallic hip-implants[3] created by a AM process called selective laser sintering. Besides using purely inorganic materials, one could also imagine fabricating fully organic constructs made from biologically interesting or even living materials. Combined with the freedom of design accompanying 3D printing, constructs mimicking the complex geometry and the hierarchy of human tissues could be fabricated one day.[4] These constructs could for example be used to generate functional tissue replacements or better tissue analogues for *in vitro* drug testing.

These considerations are strongly related to the definition of a new research field called biofabrication, where additive manufacturing processes are used to fabricate "biologically functional products with structural organization from living cells, bioactive molecules, biomaterials, cell aggregates".[5] Such products, created by

automated processes like 3D printing, can generally be divided into cell-free and cell-containing constructs, based on the approach how the functional tissue is generated. In the case of cell-free structures, the combination of material and construct geometry must support tissue maturation towards hierarchical constructs after seeding cells onto it. In the case of cell-containing structures, the cells can for example be directly placed in a structure mimicking the natural hierarchy of human tissue. Both approaches, cell-free and cell-containing, can lead to artificially created tissue replacements but there is still a long way to go and biofabrication must first prove that it can achieve this ambitious goal. As a first step towards this goal, the automated processes and the materials used need to be tested and improved.

Within this thesis, two such automated processes are explored and advanced to create 3D constructs following the principles of biofabrication. These processes are melt electrospinning writing (MEW) and extrusion-based bioprinting (also called robotic dispensing). As the process temperature used for MEW was above 37 °C in order to obtain the polymer melts, only cell-free structures could be generated. In contrast, extrusion-based bioprinting was performed between ambient temperature and 37 °C and thus cell-free as well as cell-containing constructs were realized.

In Chapter 2 a general introduction into the field of biofabrication is given and the two main printing techniques used for scaffold generation in the scope of this thesis, MEW and extrusion-based bioprinting, are described. Their current status of development is revealed by a comprehensive literature overview.

Chapter 3 is focusing on using MEW to create tubular constructs from thin polymer fibers (roughly 12 µm) in a cell-free approach. In contrast to most of the work done within the field of MEW, here instead of collecting material onto a flat collector the material is deposited onto rotating cylindrical collectors. This enables printing of tubular constructs having potentially numerous applications in scaffold based TE like blood vessels or peripheral nerves. Within this chapter, first the general behavior of the molten, charged material (also called jet) impinging on a round collector is

studied. Further, the impact of the diameter of the collector on the collected structures, both for stationary collectors and collectors that only rotate, is shown. In a second step, the collectors are rotated and translated to generate predefined structures as shown in a previous publication.[6] In contrast to the previous work, the tube diameter is reduced from the cm to an mm range. Using a 2 mm diameter collector, it is possible to print constructs with winding angles between 5° and 60°. The printed samples can be generated with very high repeatability and control of fiber deposition.

For the cell-free approach discussed in **Chapter 4**, extrusion-based bioprinting is used to process hydrogel inks. Hydrogels are 3D cross-linked hydrophilic polymer networks that can swell (up to 99%[7]) but do not dissolve in water. They can be loaded with drugs or bioactive substances that can induce tissue maturation towards a desired tissue by influencing the cellular behavior when seeded with cells. This chapter explored the possibility to mix printable hydrogel inks with mesoporous silica nanoparticles (MSN) that can, upon release from the hydrogel, deliver drugs directly to cells after being taken up by them.[8] Hereby, the release kinetics are a crucial part that could be altered by varying the charge of the particles. As the ink that contained hyaluronic acid reveals a negative charge, likely charged MSN functionalized with a carboxy-group (MSN-COOH) were released faster than positively charged MSN functionalized with an amino-group (MSN-NH_2). In the case of structures composed of sub-structures made from inks containing either MSN-COOH or MSN-NH_2 an effect of the construct geometry on particle migration and mixing within the strands is discovered. It is shown that in the case of a construct with direct contact between the different sub-structures, the MSN-NH_2 could migrate faster into the structure previously only containing MSN-COOH than in the case of constructs with no direct contact between the sub-structures.

In **Chapter 5** a cell-containing approach was performed using hydrogel inks from spider silk produced by a biotechnological process. Biotechnology uses for example

living organisms to generate reproducible and predesigned molecules.[9] In this case, bacteria (*Escherichia coli*) is modified to produce proteins. The proteins, so-called recombinant proteins, mimic sequences that are present in the dragline silk of the European garden spider (*Araneus diadematus*). It could be shown that hydrogels made from recombinant spider silk are printable without the need of thickeners or post process cross linking. Furthermore, cells (human fibroblast cell line) can be mixed with the material and printed without affecting the print fidelity enabling the fabrication of 3D structures. In addition, it was possible to change the cell material interactions with the hydrogel by modifying the proteins with RGD-sequences the cells could interact with.

Chapter 2

Background

Chapters 2.3.2 and 2.3.3 are based on the review article:

Jüngst, T.*; Smolan, W.*; Schacht, K.; Scheibel, T.; Groll, J. Strategies and molecular design criteria for 3D printable hydrogels. *Chemical Reviews* **2016**, *116* (3), 1496-1539.

*Willi Smolan and Tomasz Jüngst contributed equally.

The part of the review article presented within this thesis is based on Chapter 2 and 3 of the original review article. These chapters were designed and written by Tomasz Jüngst. The original text was modified to improve readability.

The author contributions to the original review article are as follows:

Contributor	Contribution
Tomasz Jüngst	Main contribution to chapter 2 and 3; conception and design of the manuscript; revised and provided feedback on the manuscript
Willi Smolan	Main contribution to chapter 4 and 5; revised and provided feedback on the manuscript
Kristin Schacht	Main contribution to chapter 6; revised and provided feedback on the manuscript
Thomas Scheibel	Revised and provided feedback on the manuscript
Jürgen Groll	Conception and design of the manuscript; revised and provided feedback on the manuscript;

Chapter 2.1: Biofabrication for tissue engineering and regenerative medicine

With biofabrication being a rapidly growing research field, more and more attention has been placed on it and the number of publications has significantly increased over the last years. Nevertheless, biofabrication is still a very young field of research and was first defined only about eight years ago.[10] Due to this, the terminology within the literature published on the topic is not consistent, calling for a "Need for Definitions & Norms".[11] The International Society for biofabrication recently addressed this need, revising the definition of biofabrication.[5] Groll *et al*. suggested the following definition focusing on biofabrication for Tissue Engineering and Regenerative Medicine:

Biofabrication is "*the automated generation of biologically functional products with structural organization from living cells, bioactive molecules, biomaterials, cell aggregates such as micro-tissues, or hybrid cell-material constructs, through Bioprinting or Bioassembly and subsequent tissue maturation processes.*"[5]

This definition shall be discussed in more detail, starting with the term "automated generation". It shows the importance of additive manufacturing (AM) in the research field of biofabrication. In contrast to other fields such as Tissue Engineering, which is increasingly utilizing AM techniques to improve control over construct architecture and reproducibility, their application in biofabrication is crucial. Furthermore, this importance gets even more evident at the end of the definition by reducing the AM techniques to two classes, bioprinting and bioassembly. Bioprinting was defined by Guillemot *et al*. in 2010 as "*the use of computer-aided transfer processes for patterning and assembling living and non-living materials with a prescribed 2D or 3D organization in order to produce bioengineered structures serving in Regenerative Medicine, pharmacokinetic and basic cell biology studies*".[12] As an example, robotic dispensing, that will be explained in more detail in Chapter 2.2 and Chapter 2.3, belongs to the group of bioprinting. The second class of AM

techniques used within the definition is bioassembly and was defined as "*the fabrication of hierarchical constructs with a prescribed 2D or 3D organization through automated assembly of preformed cell-containing fabrication units generated via cell-driven self-organization or through preparation of hybrid cell-material building blocks, typically by applying enabling technologies, including microfabricated molds or microfluidics*".[5] Because it is beyond the scope of this work, bioassembly will not be described in more detail and the interested reader is referred to a recent and excellent review on this topic by Schon *et al*.[13] Examinations of the reappraised definition of biofabrication reveal that not only the methods used to create constructs but also the aim to create "*biologically functional products with structural organization*"[5] distinguishes it from other research fields. The aim conveys the central hypothesis on which biofabrication is based. Namely, the rationale that using printed structures with a biomimetic, hierarchical spatial orientation improves the development of the constructs into biologically functional products. Especially because the materials were not restricted to more than "*living cells, bioactive molecules, biomaterials, cell aggregates such as micro-tissues, or hybrid cell-material constructs*"[5] this part of the definition gets even more important because it also allows to separate biofabrication from other research areas such as scaffold-based Tissue Engineering. For example, constructs fabricated using AM that are seeded with cells post-fabrication can only be declared as biofabricated if they induce a tissue-equivalent structure. Another crucial point defining biofabrication is the inclusion of the "tissue maturation process" itself which follows construct fabrication. Although this process is crucial, it was not specified more closely and "*may occur either in vitro with a culture phase – typically adopting the use of bioreactor technology – or conceivably in vivo after transplantation*".[5]

Due to the definition just described, biofabrication can have more facets and two of them will be described in the following sections:

1. Cell free approaches: using MEW to generate designed scaffold architectures potentially influencing cells maturating towards tissue equivalent structures and applying robotic dispensing to generate or induce structural organization
2. Cell-loaded approaches: using robotic dispensing to print cells embedded within an ink allowing for structural organization by directly placing the cells into different areas of the designed constructs

Chapter 2.2: Melt Electrospinning Writing – a new tool for Biofabrication

Mainly by getting affordable for private users due to open source projects like RepRap or Fab@Home, fused deposition modeling (FDM) is one of the most common AM techniques. In FDM, a filament made of thermoplastic material is melted in a heater and, on demand, pushed through a fine nozzle. 3D structures are built in a layer-by-layer fashion, exploiting the solidification of the extruded material by the temperature drop experienced by the material when it leaves the nozzle. The design for the print path of each layer is generated from 3D computer aided drawings that are sliced into 2D subunits (layers). This procedure is similar to obtaining 3D images from 2D computer tomography slices. The resolution of FDM systems is mainly limited by the nozzle diameter and typically lies in the range of about 400 µm, taking into account desktop-based private user devices. Melt Electrospinning Writing (MEW) is related to FDM but in addition to material extrusion a high voltage in the range of several kV is connected to the nozzle. This voltage charges the polymer melt and leads to stretching and thus thinning of the dispensed molten polymer (this process is called Melt Electrospinning). Due to the electrical potential, Melt Electrospinning (ME) allows the reduction of the filament diameters to the sub-micron range.[14] By collecting the filament onto a moving, computer-controlled collector, it is possible to deposit the material along a predefined path and thus generate constructs in the same way as FDM (layer-by-layer). This mode of ME is called MEW.

Figure 1 shows an overview of the different setups of ME used for MEW devices. The setup used within this work is marked by the underlined components. Generally, all systems have five zones in common which shall be discussed in the following part of this chapter from both a general process-based and a device-based view:

1. material feed/supply zone,
2. melting/heating zone,
3. electrical charging/jet initiation zone,
4. spinning zone,
5. material collection zone.

The supply zone is needed to generate a material feed through the spinneret – in electrospinning that is the general term used for the capillary or orifice the material is dispensed though.[15] The most important task within this zone is to generate a constant material supply and researchers mainly use pressurized air[16] or mechanical extrusion, either using a syringe pump[17-19] or a stepper/servo motor-based system.[20,21] Some groups also used screw-based systems for extrusion to generate the melt feed needed for the process.[22,23] All setups generate material feeds suitable for melt processing and thus there is no preferred mode. Nevertheless, extrusion-based systems are, from a manufacturing point of view, the most complex setup and compared to other hardware, such as a syringe pump, more expensive and therefore less common.

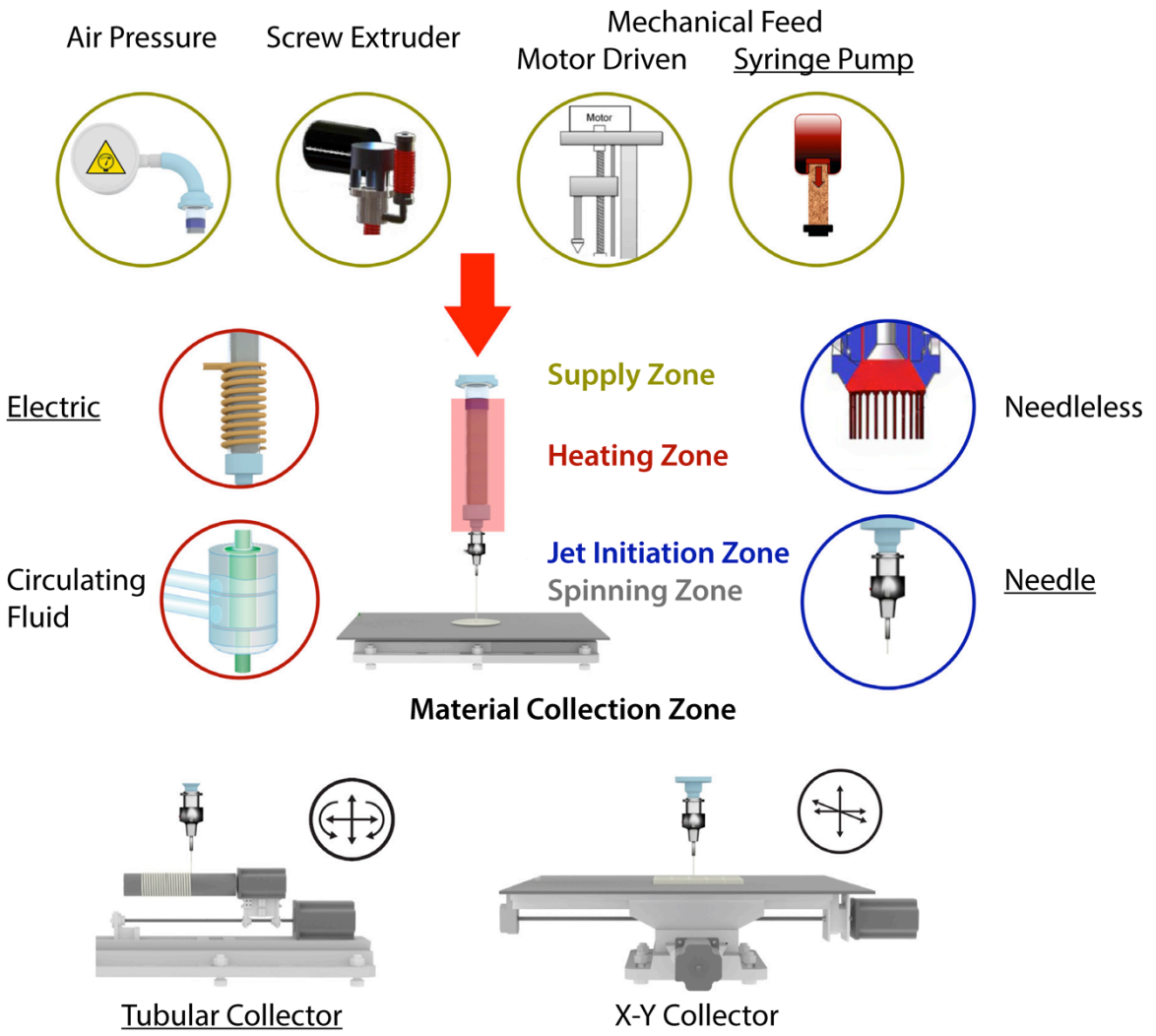

Figure 1: Melt electrospinning setups. The underlined parts have been used within this work. A color code is used to display the possible modifications within the different zones. Adapted with permission from [15]. Copyright (2016) Elsevier.

The second important zone of ME is the heating zone. Here, circulating fluids[24,25] or electrical heating systems[14,16,18,19] are mainly used to melt the material. Using an electrical heater is more complex in terms of insulating the charged spinneret from other components but handling is much easier and the response to temperature changes is usually faster making it the most common setup in ME. The most challenging demand on a heating unit is to generate temperatures that are not only high enough to melt the material but also to generate a viscosity that allows pressing the material through a fine spinneret. Because of the high viscosity of polymer melts, especially the latter can be difficult and requires temperatures above the melting or

glass transition temperature of the polymer used, taking into account that usually the viscosity of the polymer decreases with increasing temperature.[26] As an example, poly(*ε*-caprolactone) (PCL) was used in this thesis and melted to a process temperature that was 30-40 °C above the melting point of PCL (about 60 °C) using a resistance heater. At this point, it is important to note that not all materials will tolerate the printing process that can take up to several hours at elevated temperatures. Materials such as polylactic acid (PLA) tend to degrade at temperatures above their melt temperature and thus can be challenging to process.[15] In addition, materials with high melt temperatures such as poly propylene (PP) may require temperatures as high as 320–360 °C[15,27] making processing challenging from an engineering perspective. Furthermore, it is important to mention that from an engineering point of view, matching the temperature set on the device and the temperature of the polymer melt can be difficult. Depending on where the temperature is measured (e.g. within the heating elements or the polymer melt), strong differences can be observed, making the heater and the processing temperature one of the least reliable processing parameters due to the high susceptibility towards errors in measuring and comparability between different systems.

As reviewed by Brown *et al.*[15], most setups used in laboratory scale ME utilize flat-tipped, metallic hypodermic needles as spinnerets. In this electrical charging/jet initiation zone, the metallic needles are connected to a high voltage, and thus the polymer is charged. To protect other components from the high voltage the spinneret itself and the charged material need to be insulated from all other parts of the device. Although other modes are possible, for example Hacker *et al.*[28] proposed using a needless approach containing 64 nozzles to increase throughput in ME, most scientists prefer the ease of purchasing flat-tipped hypodermic needles. Furthermore, many researchers apply positive voltage to the spinneret and ground the collector. In only in a few cases, the voltage is applied to the collector and the feed unit is grounded. This is mainly preferred if the setup used does not allow applying voltage

to the spinneret, as in case of Mota *et al.*[22] who used a screw extruder to feed the material. In all cases, ME is based on charging the molten polymer resulting in repulsive interactions (Coulombic forces) between likely charged carriers. For most polymers, it requires the generation of carriers by the electrical field. This can happen either by injection of electrons into the polymer melt or by its counterpart, the extraction of electrons into the electrode called ion emission.[29] Both carriers can be generated within the polymer and are mobile. If the Coulombic force resulting from the external electrical field in combination with the generated charge carriers overcomes the surface tension, a Taylor cone builds up and a thin charged jet is ejected from the tip of the cone.[30] A phenomenological description of the Taylor cone is depicted in Figure 2 and can be stated as following observation: The droplet that is created by surface tension on the tip of the capillary material is slowly flowing through deforms into a cone shape structure by an applied difference in potential.

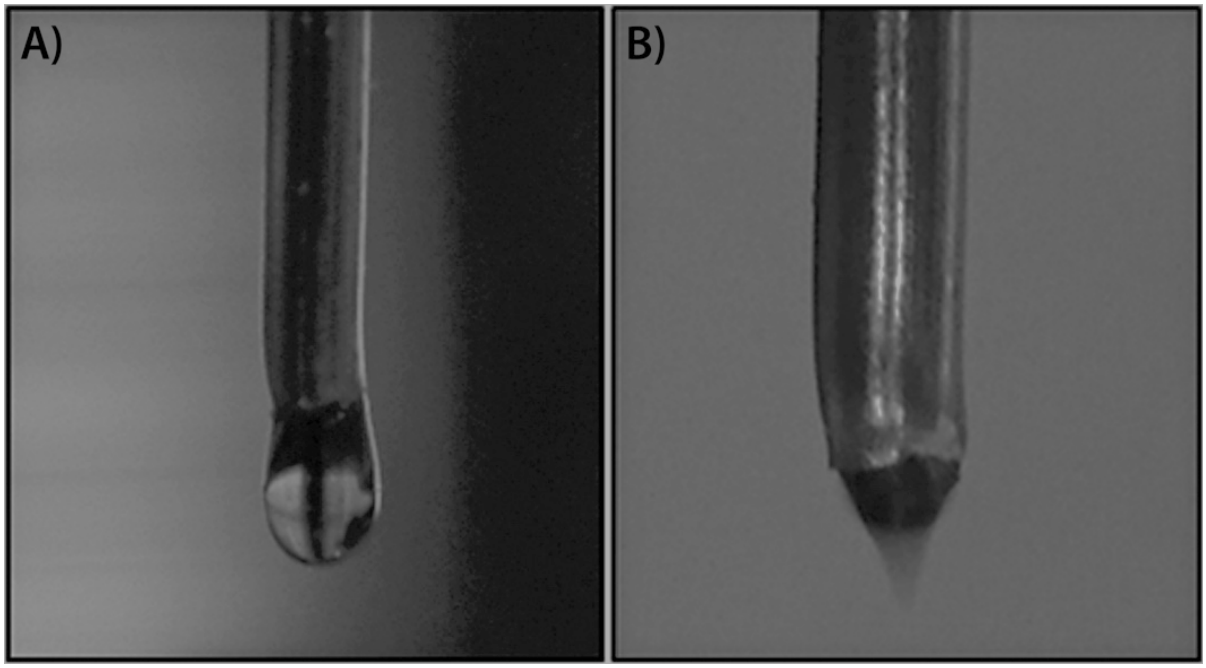

Figure 2: Taylor cone formation by external electrical field. A) shows a dissolved polymer exiting the tip of a cannula with no voltage applied to the tip and B) with a high voltage applied to the tip accompanied by the formation of a Taylor cone. Reproduced with permission from [31]. Copyright (2015) John Wiley and Sons.

Increasing the voltage first deforms the jet until at a critical value[32], a thin jet of charged polymer melt is ejected from the apex of the Taylor cone. On its way to the

collector, this jet is within the spinning zone where the repulsive electrical forces lead to stretching of the jet and a reduction of its diameter. This zone is crucial for ME and strongly depends on material properties and process parameters. The crucial process parameters within the spinning zone are the electrical potential and the distance between spinneret and collector. At a given potential, the distance will influence the electrical field and thus the forces leading to stretching and jet thinning as well as for a given potential and distance the time the jet needs to reach the collector. Taking into account that most systems do not control the temperature within the spinning zone[15], the solidification/quenching of the jet will also be strongly dependent on the spinneret to collector distance. In general, increasing the potential at a given distance will lead to increased stretching of the jet and to jet acceleration. The shorter the travelling time, the less the material can cool and the hotter it will be when it reaches the collector; it is necessary to take into account that by reducing the jet diameter the surface to volume ratio is changed which is also influencing cooling. Increasing the distance at a given potential will decrease the electrical field but increase the time the material can thin. If the material does not solidify or if the viscosity still allows the Coulombic forces to stretch the jet, the jet diameter will be reduced with increasing the collector to spinneret distance. Moreover, the spinning process is dominated by a complex interplay of different variables and is difficult to predict. To suppress bending and buckling instabilities[33] leading to a less focused material deposition on the collector, the distance between collector and spinneret cannot be too big when working in MEW mode. This is why the distances in MEW usually are in the range of several cm to mm.[15] As mentioned before, not only do the process parameters influence the behavior of the jet within the spinning zone, but the material properties also contribute, whereby viscoelastic and electrical properties of the material are most important. The viscoelastic properties of a polymer melt are mainly dictated by the molecular design of the polymers. Furthermore, the molecular weight (M_W) and its distribution influence the melt temperature dramatically. They need to be balanced

in a way that the melt resists jet-breakup but still enables adequate thinning. As reviewed by Brown *et al.*[15], for PCL, the most prominent material in MEW, M_W ranges between 45 and 80 kDa and the processing temperatures between 70 and 120 °C. In regards to electrical properties, one can imagine that if a polymer melt is non-conductive and does not allow to induce charge carriers, the electrical field will not lead to jet thinning. If the conductivity is too high, stretching will be very effective and the jet will most likely break and once it touches the grounded collector it can lead to a short circuit. Due to this, the conductivity of polymer melts used for electrospinning typically rages between 10^{-6} and 10^{-8} S/m.[34] The considerations discussed within this section display the interplay between different parameters, process and material based, that are necessary to generate fibers by ME. Furthermore, it is important to match a balance between the different zones meaning that. For example, for a given temperature and material the feedrate must be adapted to the electrical field drawing the material from the spinneret to the collector. Only if this balance is achieved, a uniform jet can be generated and filament rapture or fiber pulsing, describes the changes in fiber diameter if parameters do not match, be suppressed.[35] These considerations illustrate the importance of understanding the process and the interplay between the zones.

Another crucial zone that strongly influences this interplay is the material collection zone. In conventional ME, material is typically collected onto a stationary, flat, grounded collector. When spinning onto stationary collectors[36], first the material will be collected on a focused spot around the midline (depicted in Figure 3A) between the spinneret center and the collector. The orientation of the fibers is random and focused as shown in Figure 3B (indicated by the pink circle border). After the thickness of this layer overcomes a critical value, fibers start to deposit around that inner circle and generate spirals/circles of oriented fibers around the previously deposited part. If collection continues and the circle reaches a certain value, fibers

start to deposit on the previous structures resulting in a construct with a conical shape (Figure 3C).

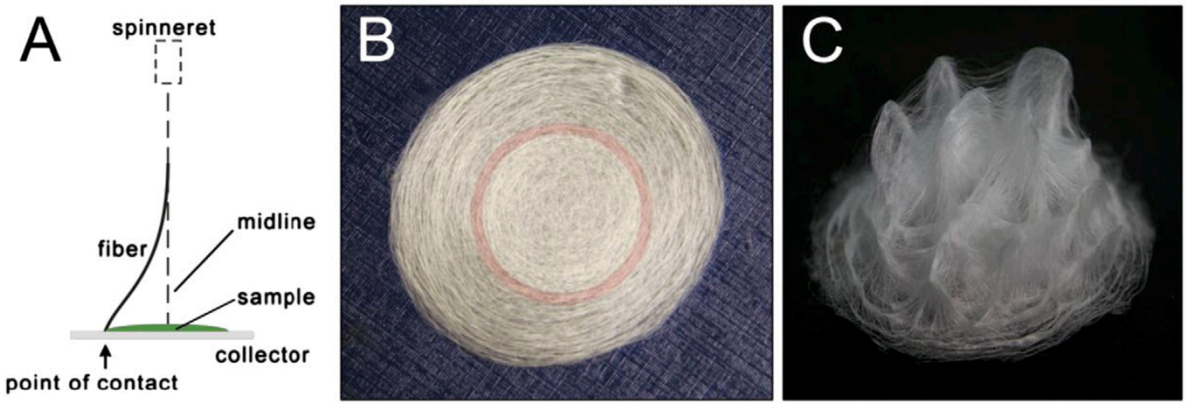

Figure 3: Collecting melt electrospun fibers onto a flat static collector. Reprinted with permission form [36]. Copyright (2014) Elsevier.

This observation can be explained[36] as follows: Initially the material is deposited randomly onto the collector and the viscoelastic properties of the jet in combination with the external electric field lead to a focused deposition. In case of intense thinning, the randomness can be caused by buckling and bending instabilities known from solution electrospinning but even if thinning is not that drastic, the fact that viscous materials will buckle as they impinge on a surface[37] leads to unpredictable orientations. This is a common effect and can be illustrated through a common everyday experience of pouring honey onto bread. As the liquid honey stream touches the bread, it will buckle. As the material continues building up on the collector this area gets less attractive for the next fibers due to the residual charge on the deposited filaments. The jet is bent away from the midline and starts to spin around the previously deposited material – the jet circles around it – because it is less attractive than the grounded collector. Due to the viscoelastic properties and the external field trying to reduce bending of the jet, the diameter of the deposition area is limited and the generated forces overcome the benefit of the material to be deposited on the collector. As a result, material starts to spin on top of the disc.[36] This observation nicely describes how previously deposited fibers influence the next layers due to residual charge. The deposited material can be considered an electret[15] and

the residual charge can dissipate over time depending on the material used, the dissipation process, and the ambient conditions. In case of polymers, the predominant charge dissipation mechanism[15] is connected to the mobility of the polymer chains and thus highly dependent on conditions such as ambient temperature.

Getting familiar with material deposition onto a static collector is a crucial part of understanding deposition in MEW where moving collectors are used. One of the most important observations is the residual charge that will limit the thickness and the quality of the constructs generated the thicker they get. In case all other parameters are given and stable, the collector velocity is a key to generate reproducible constructs in a layer-by-layer fashion. At very low velocities, the collected fibers are coiled and deposit randomly within the circumference described for the static collector. Increasing the collector speed will change deposition into repeating structures as shown in Figure 4B until, at a critical velocity known as the critical translation speed (CTS), is reached and straight fibers can be generated.

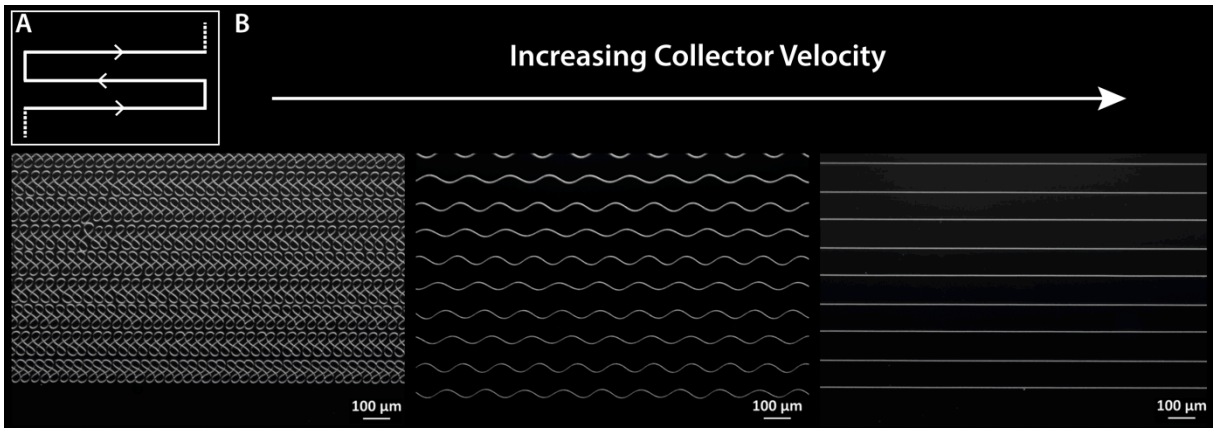

Figure 4: Influence of collector velocity on fiber deposition. Adapted with permission from [35]. Copyright (2016) De Gruyter.

If the collector velocity is increased further, the jet gets mechanically stretched, as shown in Figure 5. The higher the velocity the more the point of deposition will be shifted from its origin, directly below the spinneret. The jet will, in addition to the thinning induced by the electrical field, be mechanically drawn resulting in smaller fiber diameters.[35] Although the fiber diameter can be reduced, the control over

deposition is limited and the quality of the constructs will also be limited, especially at turning points or edges.

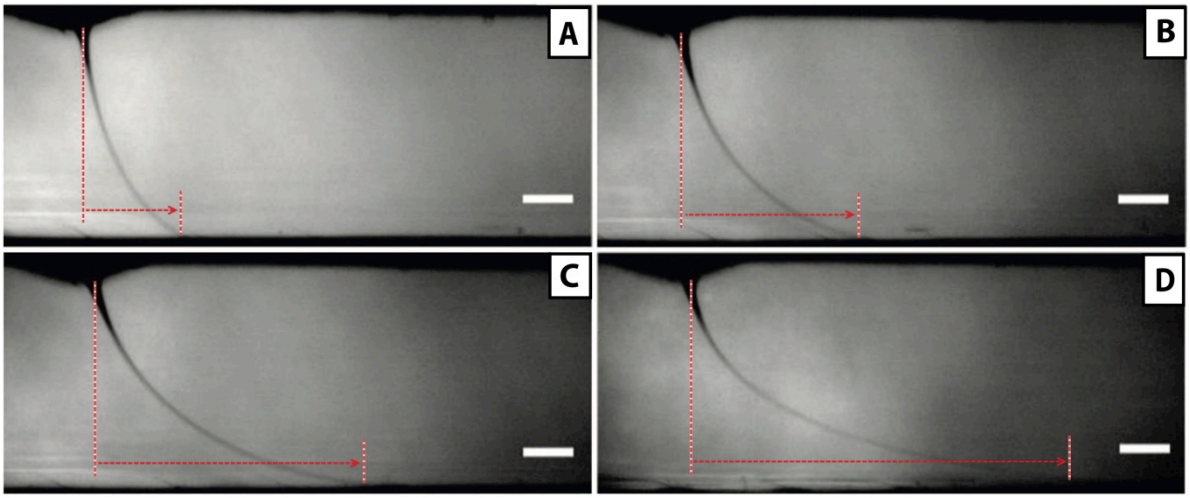

Figure 5: Collector speeds exceeding the critical translation speed. The higher the speed (collector velocity increasing from A to D) the more the deposition point of the fiber lags behind the needle tip as indicated by the red lines. Adapted with permission from [35]. Copyright (2016) De Gruyter.

At velocities above the CTS, but not exceeding it too much, the jet will be deposited close to the midline (see Figure 3A) between spinneret and collector. If the spinneret is now moved in the x-y-plane at these velocities, it enables direct writing because the point of deposition will follow the spinneret. Being able to influence the collection paths in combination with a computer-controlled stage movement is the key for generating predesigned structures in a layer-by-layer fashion. In addition, with MEW it is possible to produce fiber diameters reaching dimensions of cells (µm range) making the process very promising for analyzing cell construct interactions in biomedical applications.[15,38] Moreover, the resolution accompanied by micron-scale fibers in combination with the AM approach is very promising for biofabrication where it might help generating hierarchical constructs or inducing tissue maturation towards the desired one by printing adapted, predesigned geometries. During the last years the research on MEW has been intensified and especially by improving device setups and process properties, the quality of constructs has been drastically enhanced.

As indicated in Figure 1, the fibers can also be collected onto a rotating cylinder as performed within this thesis. The phenomena just discussed for moving, flat collectors mainly also account for cylinders. The CTS determines if a straight fiber is collected and by combining rotation and translation of the cylinder predefined winding angles can be generated. The main benefit is that collection on cylindrical targets enables the generation of tubular structures that potentially have manifold applications in the field of biofabrication such as replacement of blood vessels, urethra, bone tissue regeneration or as nerve guides. Since MEW is a relatively new field and most of the research was focused on flat collectors, the knowledge using tubular collectors is very limited.

Chapter 2.3: Bioprinting

Chapter 2.3.1: Bioinks for bioprinting

One of the major drawbacks in the field of biofabrication is finding compatible materials. From a processing point of view, the most demanding material types are so called bioinks. These are printable materials containing cells and are mainly either cell containing building blocks or cell-laden hydrogels. Within this thesis, the focus was on hydrogel-based bioinks. Printability of such inks is already a large hurdle that needs to be overcome because the materials have to fulfill certain rheological demands due to their innate structure and/or due to external stimuli.[39] These rheological demands will be discussed more detailed in the following chapter and can, simply put, be condensed to a fast solidification after deposition. Because the most common fabrication techniques utilizing bioinks are nozzle-based, the materials must be in a sufficiently liquid state to be readily dispensed through a fine nozzle and they need to solidify rapidly when deposited to ensure shape fidelity. Depending on the application, the shape fidelity needs to be guaranteed until no longer needed. In addition, it is crucial for the solidification mechanisms to be non-toxic to ensure cell survival. Besides being printable, the materials need to be biocompatible[4] and support the encapsulated cells with nutrients as well as enable the removal of waste

products. This can be ensured by an aqueous environment and adequate diffusion properties making hydrogels the most promising candidates for cell-loaded inks.[39] Ideal inks should further allow cells to proliferate and/or even guide them in maturating the constructs towards the desired tissues. In case transplantation is foreseen, the constructs should also not induce negative host reactions. Furthermore, for most applications the materials used need to be biodegradable.[4] Ideally, they should degrade as fast as the cells regenerate and replace the construct, or in a controlled manner without generating negative byproducts. This means that the degradation products should not induce toxic effects in the host by enabling the body to metabolize them or rapidly clear them from the body. This controlled manner of degradation leads to other important scaffold properties; their mechanical properties. They need to be adapted to the tissue aimed at to be replaced, for example, bone substitutes will need to be more stable than constructs used to replace skin, and should not decrease unexpected.

Hydrogels are commonly suited to encapsulate cells and applied for bioinks. The hydrogels used can be divided into natural and synthetic hydrogels. In terms of natural hydrogels, such as gelatin or hyaluronic acid, the main benefit is their innate bioactivity due to naturally occurring binding spots for cells.[40] Furthermore, their degradation products are more likely to be non-toxic. Their good biological properties and the fact that some of them are readily available make them very interesting for scientists working in the field of biofabrication and thus most publications are based on these systems. Nevertheless, they also have downsides. Most notably, they usually are not very well defined; the control over their molecular weight and molecular weight distribution is limited and suppliers often encounter high batch-to-batch variations. To improve their printability, many research groups modify natural polymers. For example, gelatin is often functionalized with a methacrylic group to enable UV or visible light-induced post process cross-linking.[41] In contrast to naturally occurring polymers used to generate hydrogels, synthetic polymers can be

designed and are, from a molecular point of view, very well defined. Due to this, the molecular weight and its distribution can be easily controlled and allow adaptations to influence their rheological properties. In addition, they enable a higher control over chemical and physical properties but functional groups improving their biological response need to be added because they usually lack natural cell attachment sites.[40] Furthermore, there are also hybrid concepts where functionalized synthetic polymers are mixed with unmodified biopolymers. One example for such inks was described by Stichler at el.[42] They used unmodified high molecular weight hyaluronic acid and functionalized polyglycidols that are able to undergo a UV-induced thiol-ene click reaction. The polyglycidols had, compared to the hyaluronic acid, a low molecular weight and could not be printed without the addition of the high molecular weight thickener that dominates the rheological properties.[42] The same group could also demonstrate that hybrid polymers from modified biopolymers and functionalized synthetic polymers can be used to design printable bioinks.[43] They used a thiol-functional hyaluronic acid and an ally-functional polyglycidol that can also undergo a thiol-ene click reaction under the presence of a photoinitiator. Although a dual printing approach where the hydrogel ink is printed within a thermoplastic scaffold made from polycaprolactone was chosen to improve the print fidelity, the biopolymer helped improving the biological properties of the bioink.[43]

After this introduction to bioinks, two specific examples of established ink systems shall be presented and discussed. One of them is alginate, a polysaccharide that is mainly produced from brown seaweed or by bacteria.[44] Being a readily available, low cost material in combination with a good biocompatibility, it is a popular source for scientists working in biofabrication. The most important property contributing to the establishment of alginate as a prominent bioink is its solidification mechanism. Alginate can be cross-linked via a number of mechanisms including calcium ions. The process is very fast and over the years, more and more ways to use this property to ensure shape fidelity after printing have been exploited. As shown in

Figure 6, scientists devised many ideas to exploit the solidification mechanism in a favorable way. One of the first attempts was based on bioplotting,[45] where alginate solutions were printed into a bath of a calcium-containing solution (see Figure 6A). In contact with the solution, alginate solidifies and the solution further supports the shape fidelity of the constructs by a buoyancy effect. Other methods exploit cross-linking directly after the material leaves the nozzle it is dispensed through. Either by using coaxial needles (Figure 6C),[46] where alginate is dispensed through the inner and the calcium containing solution through the outer one, or by using a second nozzle (Figure 6B) that sprays or deposits the cross-linker onto the exiting alginate, the material can be cross-linked to keep its shape exploiting the fast solidification mechanism. Furthermore, it is possible to print pre-cross-linked alginate solutions (Figure 6D)[47] ideally by using a reservoir setting calcium ions free over time enabling a window of printability where the material can be processed. Another possibility especially used in more recent publications is the aerosol cross-linking process (Figure 6E). Here, a fume of ionic solution is sprayed on the deposited alginate cross-linking it and thus improving shape fidelity.[48] This summary of possible printing methods to improve printing fidelity of alginate demonstrates the efforts made by scientist to optimize the printability of the material. As discussed before, shape retention is not the only demand on an ink system. It further needs to support cells. Unmodified alginate shows good shape fidelity but is strongly hydrophilic and thus cells are unable to interact with it.[44] This leads to limited proliferation of encapsulated cells.[44] Scientists also addressed this drawback by modifying alginate with RGD-sequences[49] or by combining it with other materials such as gelatin.[40] The extensive research to make alginate an established bioink demonstrates the interdisciplinary character of biofabrication and mirrors the need to address the manifold demands accompanied with bioink development.

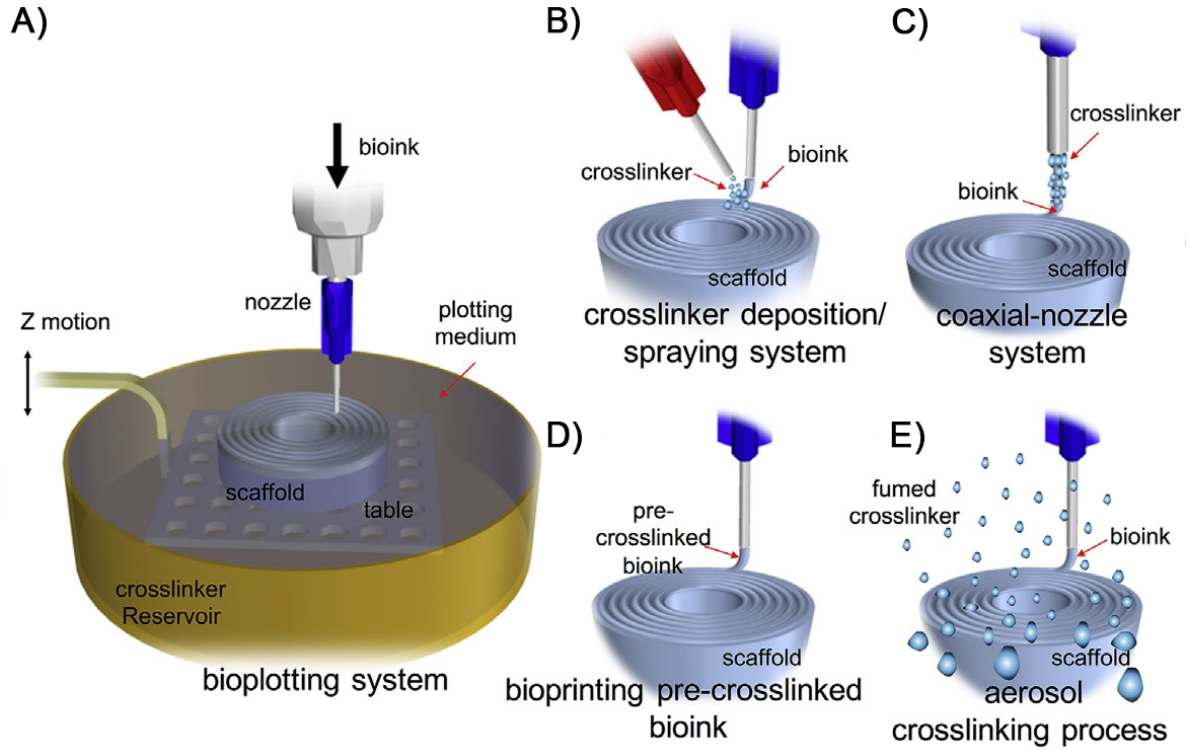

Figure 6: Different ways to introduce ionic cross-linking of alginate. A) shows the principle of bioplotting by directly printing into a bath filled with a calcium containing ionic solution. Alginate is also cross-linked directly after leaving the nozzle using additional nozzles dispensing or spraying ionic solutions onto the dispensed strands (B) or by using coaxial needles (C). In case of using coaxial needles, alginate is dispensed through the core and the cross-linker solution through the needle being further outward. Also printing pre-cross-linked solutions (D) and spraying a fume of binder solution onto the constructs during printing (E) or a combination of both are commonly applied. Partially reproduced with permission from [44]. Copyright (2015) Elsevier.

Another established bioink system is based on gelatin. In contrast to alginate, gelatin is derived from collagen, a material that is present in the human body and is the most abundant protein in humans.[50] Although gelatin sources are derived from porcine or bovine collagen and gelatin itself is denatured collagen, it still contains domains that can be recognized by cells leading to a good biological response. Collagen is also considered to be biocompatible and biodegradable and thus a popular source in 3D cell culture[51] because it supports cell adhesion and proliferation.[50] Because gelatin is water soluble as well as thermoresponsive displaying a reversible sol-gel transition, it can be used as a bioink. Having a critical solution temperature in a range between 25 - 35 °C,[50] it is liquid at higher temperatures (above

35 °C) and solidifies at lower temperatures (below 25 °C). This property is usually exploited by printing material being stored in a cartridge at 37 °C onto a cooled collector. Although its thermoresponsive properties would make the ink printable, it is obvious that using a material that is liquid at body temperature is not ideal in terms of transplantation or cell culture conditions. To enable the application of gelatin in transplantable systems, further modifications are necessary. The most common one introduces methacrylate groups by modifying the primary amines present in gelatin; the modified material typically is abbreviated as gelMA.[50] This allows using free radical polymerization to covalently cross-link gelMA. In one of the most frequently applied systems ultra violet is used to set radicals free from a photoinitiator (Irgacure) resulting in cross-linking and a permanent stabilization of the constructs. Due to this, printing with gelMA exploits a two-step solidification; initial stabilization by temperature decrease and a final stabilization by covalent cross-linking. Although gelatin shows good biological properties combined with printability, it also has disadvantages that are mainly related to poor mechanical properties and to concerns regarding its origin that might lead to transmission of diseases or immunogenic reactions when transplanted. Just as in the case of alginate, scientists are continuously seeking for improvement of gelatin-based bioinks and recent advances lead to inks systems combining different materials. One example was presented by Schuurman *et al*.[52] who added hyaluronic acid to gelMA significantly improving its printability. As shown in Figure 7, the addition of hyaluronic acid changed the rheological properties of the ink making it dispensable as a strand by minimizing its ability to build droplets upon exiting the nozzle. This resulted in a strongly improved print fidelity as shown in Figure 7D. Another example was presented by Melchels *et al*.[53] where high molecular weight gellan gum was used to improve gelMA based ink properties.

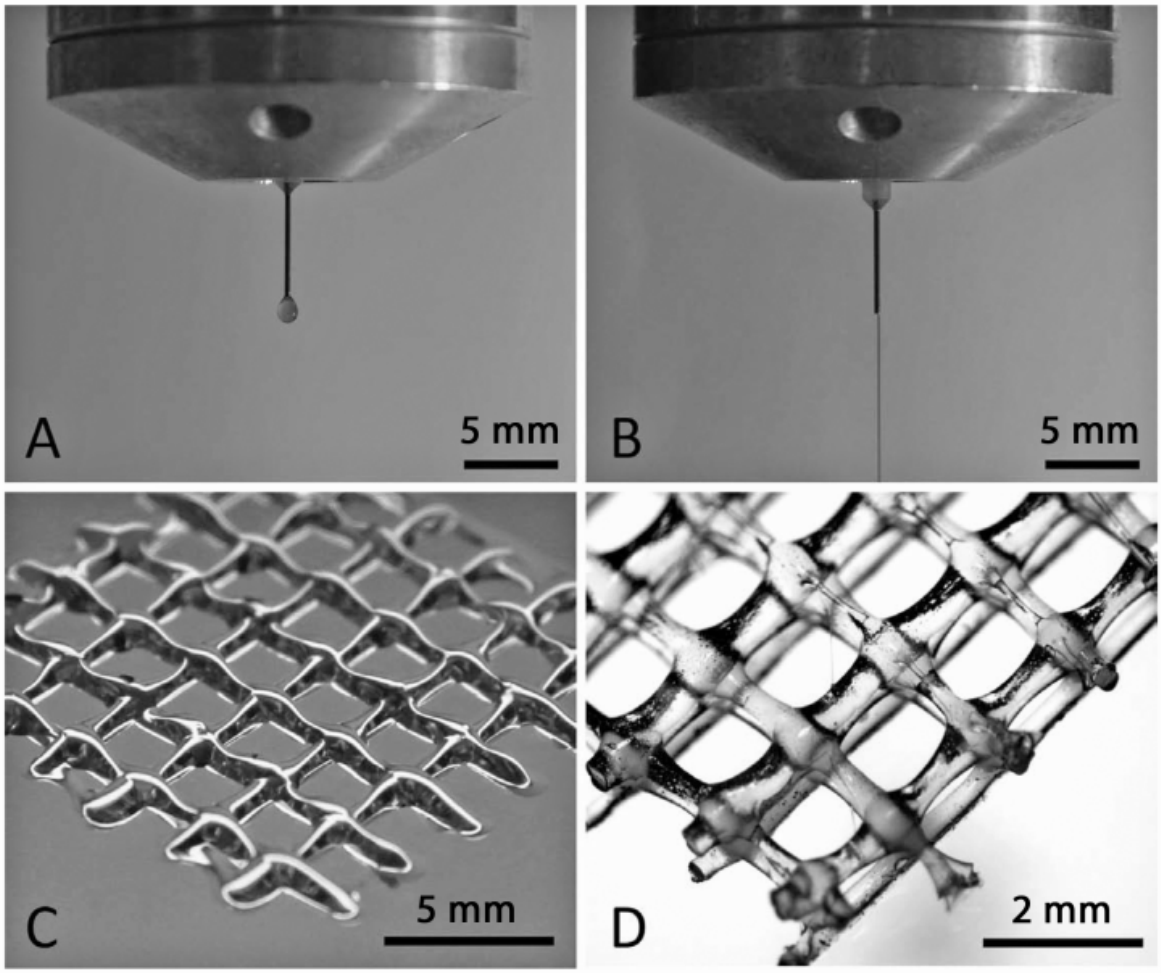

Figure 7: Improving ink printability by addition of a thickener. A) and C) show dispensing of a pure gelMA ink and a construct printed using this ink. In contrast B) shows a gelMA ink substituted with HA being dispensed. The improved shape fidelity of the gelMA/HA ink is shown in D). Reproduced with permission from [52]. Copyright (2016) John Wiley and Sons.

The examples clearly display the direction towards which the field is developing. By combining materials with different properties, ink systems are developed and adjusted to the needs of the multidisciplinary nature of biofabrication. One recent example displays this in a very evident way. Kang *et al*. developed a bioink composed of hyaluronic acid, gelatin, glycerol, and fibrinogen. To improve the mechanical properties of the constructs, the ink was deposited in between strands of a biocompatible thermoplastic material (PCL).[54] This example shows the complexity of current bioink systems and biofabricated constructs making a general discussion more difficult. Nevertheless, there are statements that account for all systems. The most

important properties of bioinks in regard to their printability are their rheological properties that will be discussed in the following chapter.

Chapter 2.3.2: Rheological demands put on bioinks

From a rheological point of view, printing using nozzle-based systems can be considered as material flow through a contraction followed by tube flow. After the material is ejected and deposited onto the collector, it needs to undergo a fast phase transition obligatory to preserve the shape and thus enabling fabrication of 3D structures. Therefore, the rate of this phase transition is crucial for printing. After discussing some fundamentals of liquid dynamics, the next sections will subsequently increase the complexity of the regarded models approaching towards printable inks highlighted with examples of applied ink systems. For further review on the topic of liquid dynamics and polymer rheology the reader is referred to a by far not complete list of excellent literature dealing with this topic.[55-60]

Chapter 2.3.2.1: Rheology of non-Newtonian liquids

Liquids can generally be divided in two categories: Newtonian and non-Newtonian. For Newtonian fluids, the viscosity is independent of the shear rate whereas for non-Newtonian liquids the viscosity tensor exhibits a shear rate-dependent behavior (Figure 8). This dependence can be used to separate non-Newtonian liquids mainly into the following types: shear thinning, shear thickening, thixotropic and rheopectic. A complete list with example systems developing the different properties can be found elsewhere.[57] As shown in Figure 8, shear thinning materials show a decrease of viscosity with increasing shear rates. Despite very low molecular weight materials, most polymer solutions show this behavior. Polymeric liquids further usually exhibit a linear plateau at low shear rates called zero shear viscosity (also low shear viscosity or first Newtonian plateau). Although not displayed in Figure 8, shear thinning polymeric liquids usually evolve a second plateau called high-shear viscosity or second Newtonian plateau.[58] Since in most cases, this plateau

is only slightly higher than the solvent viscosity, the second Newtonian plateau is not relevant for printing processes.

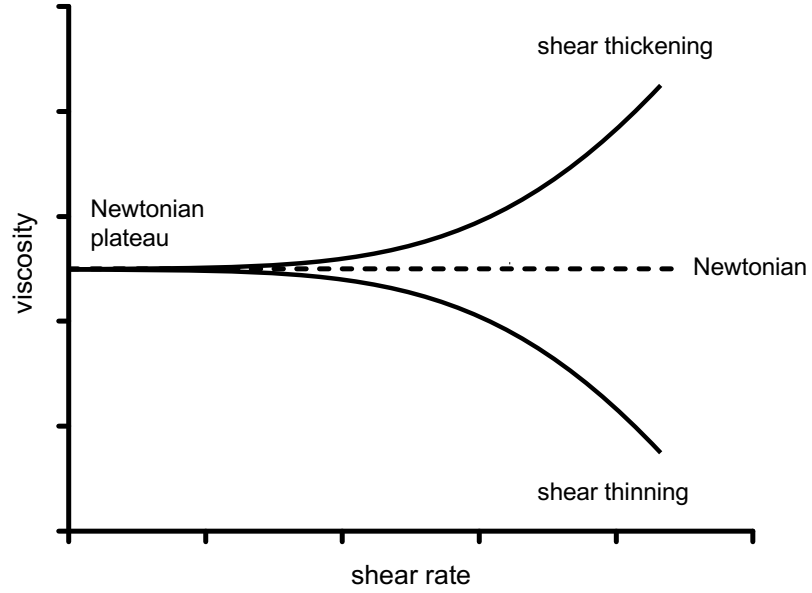

Figure 8: Viscosity against shear rate for Newtonian and different non-Newtonian fluids. Reprinted with permission from [39]. Copyright (2016) American Chemical Society.

Another interesting phenomenon observed for non-Newtonian fluids is thixotropy. Especially when analyzing only limited shear rate ranges, viscosity against shear rate plots of thixotropic materials are often similar to those of shear thinning materials. But there is a very distinct difference: thixotropy is time-dependent whereas shear thinning is not. This becomes evident when the viscosity is plotted against time for a constant shear rate. For shear thinning fluids, the viscosity will be constant but for thixotropic materials it will decrease with time. A detailed discussion of thixotropy and also the hysteresis that can be examined by measuring material properties during increasing and decreasing shear rates is not within the scope of this thesis and described elsewhere.[61,62] In terms of printing, the time-dependent viscosity exhibited by thixotropic materials is important and must be considered as it can contribute to inhomogeneous dispensing.

Shear thickening (see Figure 8) is the opposite effect to shear thinning and is characterized by an increase of viscosity with increasing shear rates. Also, just as shear thinning has shear thickening as counterpart, rheopectic materials display opposite

characteristics to thixotropy. It is obvious that these behaviors both are not favorable for printing applications.

Chapter 2.3.2.2: Important aspects of the printing process

As mentioned above, a very important property for printable hydrogels and a crucial parameter to take into account during ink development is the recovery rate of transition to the solid state after printing. In order to achieve shape fidelity, the material must undergo a rapid structural change and keep its shape after dispensing. The faster the material gelifies after ejection, the higher the resolution of the resulting structure will be. In the case of recovering materials, the interactions between the molecules will strongly influence the transition and the time it takes after flow stops.

Summarizing this discussion, from a rheological point of view an ideal ink for hydrogel printing combines the following characteristics:

- Physical gel formation before printing with a shear thinning but not thixotropic behavior down to a viscosity that allows printing with the selected technology
- Rapid regelation after printing for shape fidelity at high resolution

If cells are part of the formulation, the viscosity before printing must allow mixing and homogeneous 3D distribution of cells throughout the printing process without affecting viability. Cell sedimentation that might lead to nozzle clogging and/or uncontrolled inhomogeneous cell distribution through the printed construct must be avoided. Also, shear forces cannot exceed limits tolerable for cell survival.[63,64] Hence, cell aggregation during the timeframe of printing is usually not beneficial as it affects shear rate sensitivity.

Chapter 2.3.2.3: Underlying molecular concepts – colloidal solutions

In the following sections, some basic particular and molecular concepts and the ideas gained from discussing non-Newtonian fluids shall be introduced. One of the simplest models able to depict non-Newtonian fluid behavior is a so-called hard-

sphere system. This can be considered as monodisperse suspension of spherical particles in a Newtonian fluid not experiencing interparticle and particle-liquid interactions. Although there are few real model systems showing all necessary properties,[65,66] there is some general knowledge one can gain from that model, such as the fact that non-Newtonian characteristics will only be developed when concentrations are high enough.

When interparticle interactions are additionally taken into account, these interactions are manifold and they will strongly influence rheological properties of the particulate systems inducing suspensions to be able to depict all known non-Newtonian behavior.[66] The general character of interparticle interactions can be distinguished using the concept of interaction potential energy[65] that helps describing the resulting forces and relevant length scales. Roughly, these interactions can be categorized into electrostatic, steric, electrosteric and structural. Discussing relevant length scales of these interactions underlines why the properties of suspensions will be concentration dependent. At low solid loadings, the particles will not alter the linearity of the Newtonian fluid because the distances between particles are much bigger than the length scales of interactions. Increasing the loading, interactions will more likely appear. If interparticle interactions dominate over Brownian motions so called rest structures can form.[58] In case of repulsive interactions, this will result in pseudo-lattice structures whereas in case of attractive interactions the particles will aggregate. When shear is applied to those systems and is slowly increased these structures will first withstand the generated forces and then be rearranged due to the reversible character of the interactions. Depending on the interaction properties, this can lead to a macroscopic shear response comparable to a first Newtonian plateau or even induce yield stress. A further increase in shearing results in permanent disintegration of the aggregates and non-restored arbitrary particle distribution after shearing. The shear-induced velocity gradient leads to orientation of the particles that enables them to more freely move over each other. That in turn leads to shear thinning

or, in case of attractive interactions, also to thixotropy.[67] Generally, such systems will depict a second Newtonian plateau if all particles show the orientation and, by disruption of those layer orientations, show shear thickening with further increasing shear rates. If shearing stops, the particles will return to a rest structure.[58] Of course, these descriptions are very pictorial and there are theoretical models that represent the properties of suspension more adequately.[58,68-70] Furthermore, scientific descriptions of colloidal suspensions are also discussed in specialized literature.[65,67] In the next section, an example of how colloidal systems can be exploited for ink development shall be given.

As described, particle interactions are crucial for the properties of suspensions and thus need to be considered when designing colloidal inks as shown by the Lewis Lab. Jennifer Lewis and coworkers transfer knowledge from ceramics science to develop concentrated colloidal gel-based inks for direct writing applications.[71] Over the last years, they have generated inspiring work[72-74] continuously improving their inks by analyzing and controlling interparticle forces. Here, one of their earlier systems[75] shall be discussed as it comprises a model system containing monodisperse silica microspheres that displays their meticulous scientific work on developing printable colloidal inks. Coating the colloids with poly(ethylenimine), they exploited the concept of electrosteric[65] interparticle forces to tailor the viscoelastic properties of the system. Electrostatic interactions between negatively charged silica particles and positively charged poly(ethylenimine) induced strong ionic interactions between the two species. In addition, changing the pH of the solution they were able to vary the zeta potential of the coated particles and found the point-of-zero charge to be at a pH of about 10. At this pH, the absence of electrostatic repulsion between the colloids led to a system strongly flocculated by van der Waals forces and thus to a fluid-to-gel transition. Finally, they added cellulose as thickening agent to increase ink viscosity and reduce flocculation kinetics even enabling fabrication of unsupported

spanning structures that are considered to be the most difficult structures to print using robotic dispensing systems.

Describing ceramic colloid systems for a non-expert it might seem strange that there are only few real systems displaying properties of the hard sphere model. But due to surface charges, even uncoated rigid ceramic particles will depict an interaction potential energy longing for a classification as soft-sphere system.[65] Taking into account that spheres can also be deformable will be the next step approaching towards the description of polymeric systems. As outlined before, low concentrations of hard spheres in a solution will not change the Newtonian characteristics of the liquid in which they are suspended in. Nevertheless, they will increase the viscosity by deviating the fluid flow lines.[58] By shear induced shape adaptation deformable particles will lead to less deviation and thus to a less pronounced viscosity increase considering shear.[66] For higher concentrations, this will result in more pronounced shear thinning. This effect contributes to the extraordinary properties of blood.[76] Under shear, red blood cells will deform[77] enabling blood to flow even through the tiniest capillaries in the human body. For synthetic systems, the particle elasticity also has a major impact on rheological properties as reviewed by Vlassopoulos *et al.*[78] They pointed out that colloid elasticity not only has an impact on flow induced material response but also on the zero-shear viscosity of colloidal suspensions and that the decrease of zero shear viscosity with increasing particle deformability is generally more pronounced at higher volume fractions. The models they considered for their review contained polymer coils and star polymers evolving the lowest elasticity of the discussed systems. Singh *et al.*[79] performed computer simulations of ultrasoft colloids under linear shear flow showing that star polymers deform due to shearing. Further, Huang *et al.*[80,81] used simulations calculating that linear polymers will depict shear induced decoiling and stretching accompanied by orientation along the flow direction. Huber *et al.*[82] visualized tumbling dynamics of semiflexible polymers under shear conditions imaging fluorescently labeled actin molecules.

Chapter 2.3.2.4: Underlying molecular concepts – polymer solutions

Using polymers as model systems for soft colloids leads to the field of polymer solutions. Just as for the hard sphere model, the concentration will be crucial for the rheological response of such systems. At very low volume fractions, the distance between polymer chains will be larger than their size. These systems are called dilute. As already discussed for hard and deformable spheres, at very low concentrations, solvent properties will not be altered significantly. Increasing the concentration results in coil overlap and leads to semidilute solutions. Although the solvent will occupy most of the volume, the coils will overlap and have a considerable impact on the rheological properties. Being able to overlap clearly distinguishes polymeric systems from the suspensions discussed before. Raising the solid loading further will lead to concentrated solutions dominated by coil interactions.[56] Printable hydrogels will usually depict concentrations either in the semidilute or concentrated regime and thus for the following discussions only these systems will be considered. Even early models describing semidilute systems, not taking into account other interactions than topological, dealt with coil overlap and with the concept of entanglements.[83] Although used in one context it shall be mentioned that overlap and entanglement should not be put on one level. Semidilute and concentrated solutions are defined by coil overlap but do not need to be entangled.[66] For the chains to entangle they will need to be long and sufficiently flexible. Experimental results have shown that there is a critical molecular weight for the formation of entanglements that depends on the flexibility of the polymer backbone.[58,66] Entanglement can, however, only occur in semidilute or concentrated solutions. If chains are separated from each other they will not be able to interact. To some extent, these findings are related. The longer the chains are, the bigger their interaction potential will be and the higher the number of entanglements at the same concentration. Connecting the entanglement density to rheological properties the concept of entanglements drastically changed the scientist understanding of polymers. Accompanied by the model of reptation researchers were

able to relate macroscopic polymer properties to the microscopic behavior of single molecules. Due to that, the concept of entanglements is an excellent example of how theoretical models can enrich and evolve general understanding. As the focus here should not be on models, the interested reader is referred to excellent reviews dealing with this topic[84,85] and the argumentation describing general factors influencing the properties of semidilute and concentrated polymer solutions shall be continued.

Aside of entanglements and the movement of polymer chains within semidilute/concentrated solutions, intermolecular interactions have to be taken into account. In general, an increase of concentration will increase the amount of interactions and thus polymer concentrations in solutions will have an influence on the rheological properties. As shown in Figure 9, a general observation dealing with polymer solutions is that with increasing concentration the zero-shear viscosity is raised and the onset of shear thinning is shifted towards lower values.[69] With increasing load volume, the viscoelastic properties will be more pronounced and lead to a bigger difference between first and second Newtonian plateau values.[58] Another aspect is the influence of the molecular weight distribution on rheological properties of polymeric liquids. Generally, it can be observed[66] that increased polydispersity influences the transition from Newtonian to non-Newtonian behavior. Solutions with a broader molecular weight distribution will exhibit non-Newtonian properties at lower shear rates but shear thinning will not be as pronounced. The decrease of viscosity against shear rate will be shifted to higher shear rate values.

Recently, researchers have exploited this concept for designing printable materials. Although using materials with a broader molecular weight distribution was not the only aspect influencing the rheological behavior of the inks, they could also tune the flow properties of their systems by either mixing batches of different molecular weight distributions of identical materials[74] or by combining two types of materials with different distributions.[53] These examples show that modern inks usually are, from a rheological point of view, complex systems. The complexity is mainly

introduced by interactions between the molecules and by molecule liquid interactions. Due to the huge number of interactions, a closer rheological discussion is outside the scope of this thesis. It was rather intended to present and analyze simplified basic views of rheological concepts aiming for a more generalized understanding of the possible system variations allowing controlling the rheological properties.

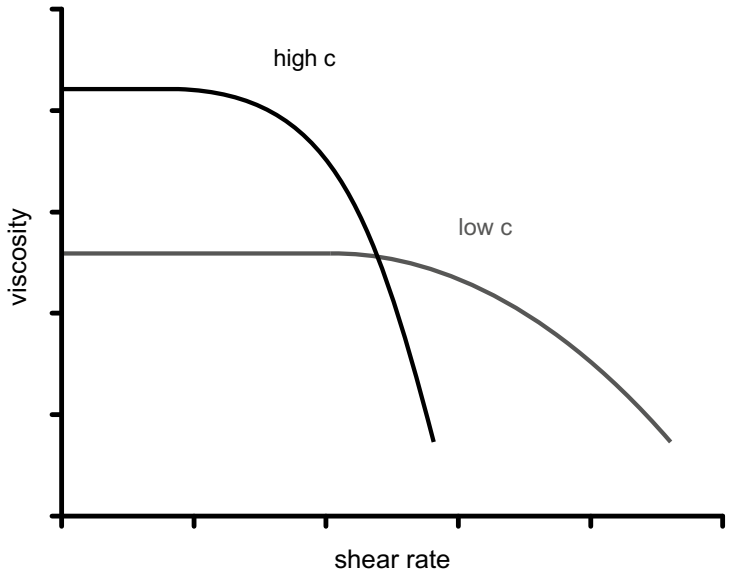

Figure 9: Viscosity against shear rate for high and low polymer concentrations c of a homopolymer solution in a good solvent. Reprinted with permission from [39]. Copyright (2016) American Chemical Society.

Chapter 2.3.3: Fabrication techniques for bioink-based biofabrication

There is a variety of technologies that enable structuring hydrogels, which represent one of the most prominent bioink types, into 3D constructs. Two very interesting processes capable of fabricating complex 3D objects from hydrogels are two-photon polymerization (2PP) and stereolithography (SLA). They both use light to induce spatially limited polymerization and can be used to create well-defined structures. For both processes, the construct is mainly generated by light-induced radical polymerization within a monomer reservoir or light-induced cross-linking of a photopolymer. In 2PP, a femtosecond laser is focused onto a spot within this reservoir,

releasing radicals from a photoinitiator on its path. These radicals start a polymerization/cross-linking reaction leading to solidification of material along the laser track. Usually a drop of material, enclosed between two microscopy glass cover slips with spacers in millimeter range defining the construct thickness, is used as reservoir. Relating the reservoir size to cover slips and taking into account that prints usually are much smaller than the overall size of the slips gives an indication of the producible sample size. Although object size is limited, 2PP offers the possibility to produce constructs with spatial resolutions as small as 100 nm and is thus especially interesting for analyzing cell-construct interactions.[86] SLA enables overcoming the size limitations of 2PP prints easily generating constructs with dimensions in the centimeter range. Although compared to 2PP, the resolution is decreased it still is as high as 80-125 µm.[87] In SLA, the objects are produced in a layer-by-layer fashion. The most frequently applied setup is the bottom-up system where a laser scans and solidifies the top layer of a reservoir. After one layer is created a movable platform lowers the construct further into the resin covering it with the next material layer. Although it they enable the production of geometrically complex structures, the main disadvantage of the light-induced processes introduced in this section is the limited number of suitable resins. Especially when printing structures from cell-containing hydrogels, emphasis needs to be put on cytotoxicity of the photo-initiator.[88]

Due to the large variety of fabrication systems available, the choice of the method mainly depends on the material that shall be processed and the structure (size, architecture, resolution) that needs to be created. As will be discussed, each method has limitations and none of the approaches can be considered better than another one. Because this thesis focuses on bioprinting and biofabrication, the attention shall be put on the three most important and best-established technologies for printing of hydrogels under cell-friendly conditions: laser-induced forward transfer, inkjet printing and robotic dispensing. These techniques will be described in detail

and compared to each other in the following sections, with particular emphasis on robotic dispensing as the primary method used in this thesis.

Chapter 2.3.3.1: Laser-induced forward transfer

The reviews of Chrisey *et al.*,[89] Ringeisen *et al.*[90] and Schiele *et al.*[91] give excellent summaries of laser-induced forward transfers (LIFT) techniques used for cell printing and also show examples of structures being produced with these methods. For biomedical applications, mostly modified-LIFT techniques are applied. Generally, all these systems have the same setup in common and are comprised of three main components; the first is a pulsed laser, the second a donor slide (ribbon) from which the material is propelled and the third is a receiving substrate. The laser is focused onto a laser-absorbing layer evaporating the material and generating a high gas pressure propelling material towards the substrate. By controlled movement of donor and/or substrate, it is possible to build up 2D and 3D structures from material droplets.[92-96] For processing biological materials, two different versions of modified-LIFT are utilized: matrix-assisted pulsed laser evaporation direct writing (MAPLE-DW) and absorbing film-assisted laser-induced forward transfer (AFA-LIFT). The main difference between these two techniques can be found in the donor slide setup. In the most frequently used MAPLE-DW setups, the donor slide comprises two different layers, a laser transparent support layer and a laser absorption layer. If the printing material itself is not absorbing light efficiently it needs to be mixed with a matrix that will adsorb light and transfer the energy. In case of cell printing this matrix usually is a hydrogel, cell media with addition of glycerol or extracellular matrix.[90] In contrast to that in AFA-LIFT and its related versions like biological laser printing (BioLP), the donor contains three different layers, a laser transparent support layer, a laser absorption layer, and a layer with the deposition material (Figure 10A). The laser adsorption layer in general is a thin (about 100 nm) metal coating that absorbs the laser light leading to evaporation of the coating. This evaporation leads to a high-pressure bubble expanding towards the surface and finally to material deposition. Although not

obligatory[97] the receiving substrate in modified-LIFT processes for biomedical applications is mainly coated with a thin (20-40 µm) hydrogel layer that prevents the deposited material from drying and in case of printing cells cushions the impact.[90] In the following section, AFA-LIFT and MAPLE-DW shall be compared in regards of printing hydrogels for biomedical applications.[91]

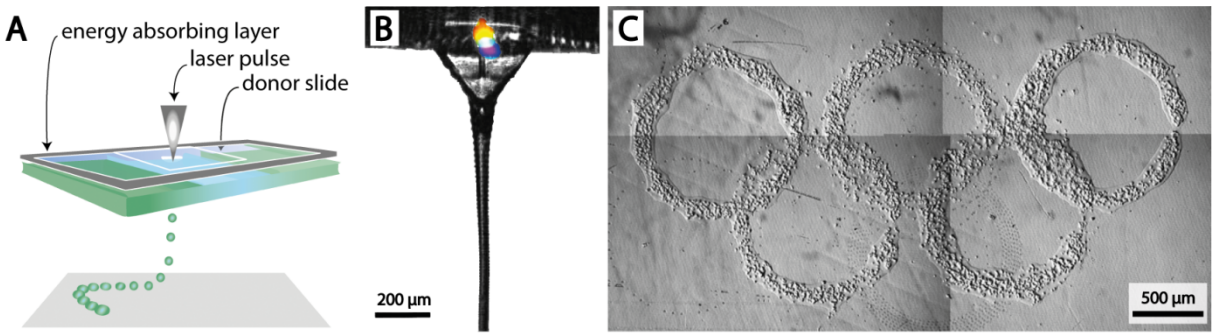

Figure 10: Laser-induced forward transfer (LIFT) A) Schematic drawing of the process. B) Close-up view of the jet generated by the incident laser pulse. C) Cell pattern printed with LIFT. Reprinted with permission from [39]. Copyright (2016) American Chemical Society.

As discussed, the main difference between MAPLE-DW and AFA-LIFT is the ribbon. In MAPLE-DW, the light-absorbing matrix is mixed with the biomedical material. The heating within this layer and the irradiation with light might cause problems when printing sensitive materials but as many researchers could prove it did not seem to have negative effect on cell viability.[98-100] AFA-LIFT and BioLP use an additional light-absorption layer mainly from Au, Ti or TiO_2.[94,101,102] This layer protects the underlying biological layer from radiation-induced damage but being evaporated will contaminate the printed material. It could be shown that by using an energy conversion layer the reproducibility and resolution is enhanced (Figure 10C shows a 2D pattern printed with LIFT). Furthermore, this additional layer increases the selection of possible printing materials.[90]

Chapter 2.3.3.2: Inkjet printing

The process of inkjet printing is well known from desktop applications. Many private users have printed 2D graphical printouts and maybe even refilled cartridges unwittingly gaining experiences potentially useful for biofabrication. The first printers

used modified desktop setups and especially have cleaned and reused cartridges originally produced for desktop applications.[103] This straightforward approach, in combination with the accessibility for printers, led to a profound understanding of the inkjet printing process for biomedical applications. The following section gives a basic overview of the different setups. For more detailed discussion of inkjet printing the reader is referred to a variety of excellent reviews dealing with the inkjet technology and material properties for inkjet printing.[104-111]

Inkjet printing can generally be operated in two modes. In continuous inkjet (CIJ) processes, the on-going generation of drops creates a jet. Usually, these drops are individually charged and deflected by a second pair of electrodes for printing. Droplets that are not needed for printing are collected in a gutter and can be reused. CIJ is primarily used as a fast process for marking and coding of products. The second inkjet printing mode is drop-on-demand (DOD) printing. Here, drops are only generated when needed for printing. DOD is the setup well known from consumer inkjet printers used for 2D graphical printouts. The working principle is based on an actuator generating triggered pulses leading to the ejection of a defined material volume from a reservoir. Ideally on its way to the substrate the ejected material will transform into a single drop being collected on a predefined position on the substrate. As shown in Figure 11A, there are two common driving forces for pulse generation applied for DOD printing. In thermal inkjet printers, a heater is used to evaporate its surrounding ink generating a vapor bubble that leads to ejection of material. Simply put, the droplet generation is triggered by an electrical pulse leading to temperature increase in the heater accompanied by ink evaporation and material ejection. Material is also expelled from the reservoir using piezoelectric actuators. Here, the applied voltage will generate a distortion of a piezoelectric crystal leading to triggered ejection of material. In the next two sections, the benefits and disadvantages of the different inkjet printing methods described above shall be discussed with a focus on hydrogel printing for biomedical applications.

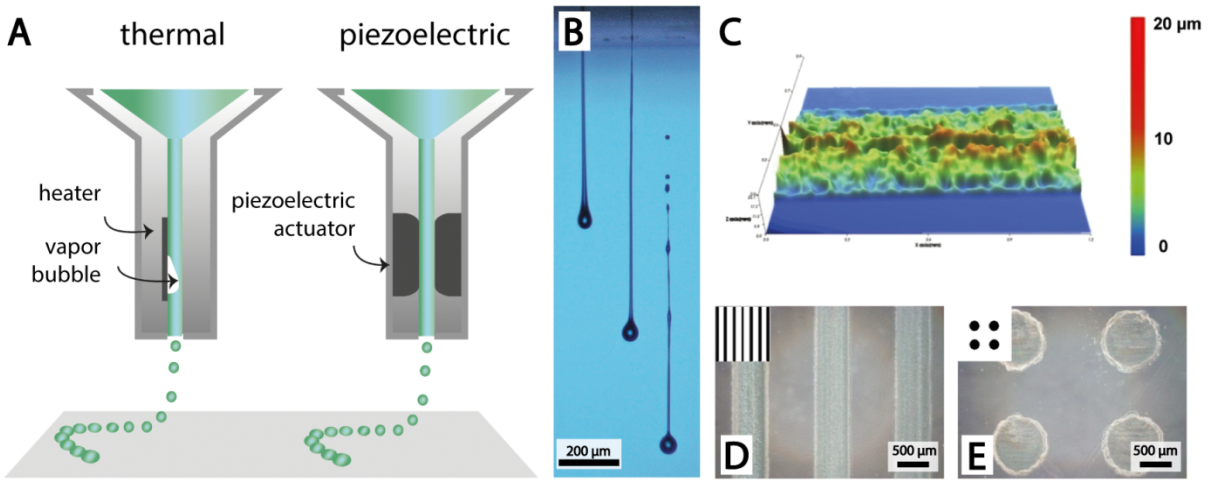

Figure 11: Inkjet printing A) Schematic drawing of the process. B) Example for propelled material after ejection at different time points using a drop-on-demand printer. C) Surface profile of a linear pattern printed with inkjet-printed PLGA; D) and E) Different patterns of PLGA printed with a piezoelectric inkjet. Reprinted with permission from [39]. Copyright (2016) American Chemical Society.

The main disadvantage of CIJ for laboratory scale and biomedical applications is the high material throughput accompanied by the continuous stream of drops. Compared to other printing methods used for these applications, more material is needed and concerns regarding sterility and potential material property changes due to processing might arise when the material is reused. In contrast, the DOD process is using material very efficiently and can also handle small batch sizes making it highly interesting for small-scale and non-industrial applications. In addition, the spatial resolution of DOD inkjet printers is higher than CIJ systems.[108]

In thermal inkjet printers, the temperature of the heated resistor can reach about 300°C.[105] Nevertheless, Xu *et al.*[112] and other groups, as reviewed by Boland,[104] were able to print viable cells using thermal DOD printers. It is believed that the short duration of heating pulses in the range of several microseconds only leads to a slight temperature increase (a few degrees) of the bulk material not negatively influencing cell viability.[112] Setti *et al.*[113] could also print enzymes with negligible loss of activity using a thermal inkjet. As identified by Saunders *et al.*,[110] further research on the influence of thermal damage while printing biomolecules needs to be undertaken to establish thermal inkjet printing in the field of biomedicine. Due to these concerns,

most researchers working with inkjet printers for biomedical application use piezoelectric DOD inkjet systems to avoid ink property changes by heat exposure. Another important benefit of piezoelectric actuators in contrast to thermal is that it allows for an easy change of the piezoelectric crystal distortion and thus in the pulsing. This again enables controlling the ejected material volume and velocity of the created drop making the process more flexible to parameter adjustment depending on material characteristics.[108]

Chapter 2.3.3.3: Robotic dispensing

Especially during the last years, a large number of great reviews dealing with technologies applied in biofabrication were published.[4,114-120] All of these reviews also discuss the process of robotic dispensing displaying how promising this comparatively new technique is for the field of biofabrication. This is mainly due to the fact that robotic dispensing facilitates the production of 3D objects with sizes and dimensions relevant for biomedical applications in short processing times. In the following section, an introduction to the different setups (Figure 12A) used for biomedical applications termed robotic dispensing is given.

Robotic dispensing is primarily used for printing 3D constructs from continuous filaments. Material is loaded into a reservoir and dispensed through a nozzle. By automated movement of the nozzle relative to the build plate constructs can be generated in a layer-by-layer fashion. The driving mechanism of dispensing can generally be either pneumatic or mechanical. In the most frequent pneumatic-driven setup, the valve triggering material ejection is placed between the inlet of the pressurized air and the material. Mechanically driven dispensing is mainly screw- or piston-based. Piston-based systems eject material triggered by controlling the linear displacement of a plunger. The displacement of the piston can directly be related to the dispensed volume. In screw-driven systems, rotation of the screw transports the material to the nozzle and is thus responsible for dispensing. The material feed cannot only be controlled by screw rotation speed but also by screw design.[117] All robotic

dispensing systems share the common process of material dispensing through a fine nozzle determining the resolution of the process.[118] Consistent with industrial dispensing applications, the design of the nozzle has a big effect on the dispensing homogeneity. Because most printer setups for biomedical application use disposable and interchangeable needles, it is important to choose the right needle with respect to given ink properties. In their latest review, Dababneh *et al.*[119] stated that further improving nozzle design might be necessary in the field of bioprinting. Combining the fundamentals of the work of Yan *et al.*,[63] who mathematically modeled the forces cells experience during printing with nozzle design, dependent shear stress analysis during dispensing might help improving cell survival. In the next section the different robotic dispensing modes explained above shall be described focusing on processing of hydrogels for biomedical applications.

Figure 12: Robotic dispensing A) Schematic drawing of robotic dispensing showing the different mechanisms of ejection. B) Magnified view showing material dispensing from the needle and collection onto a substrate; C) Stereomicroscopic image of a printed Pluronic F127 construct. Reprinted with permission from [39]. Copyright (2016) American Chemical Society.

Utilizing a concept known from thermo-polymer extrusion, screw-driven systems are the most favorable choice for processing high viscosity materials because they are able to generate high pressures for material dispensing. Tailoring the screw design helps adjusting the process in regards to feedrate and dispensing homogeneity. Having the most complicated setup, in addition to being able to generate the highest shear stresses, makes screw driven systems the least applied approach in biofabrication. From an engineering point of view, pneumatically driven systems have

the easiest setup. Nevertheless, applying high pressures typically makes pneumatically driven systems more suitable for processing higher viscosity materials than piston driven systems.[118] Being able to deal with a broad range of pressures and thus with a broad range of material viscosities makes pneumatic dispensing the most versatile robotic dispensing mode. Using pressurized gas to apply dispensing force also implies its biggest disadvantage. The gas used for dispensing is compressible what will result in a delay between material flow start/stop signal and actual dispensing start/stop. This problem can be addressed either by applying a time delay before reaching printing position and a vacuum to stop dispensing or by using a valve sitting just in front of the orifice. Piston driven systems have the most direct control over dispensing. As described above, the linear piston displacement directly leads to material ejection. Because most printers use disposable syringes made from plastics the maximum dispensing pressure is limited by the stability of the piston and the quality of the sealing between piston and barrel. Taking into account that at laboratory scale dealing with small batch sizes might be necessary, piston and pneumatic systems using disposable barrels that can be emptied nearly entirely are preferential to screw driven systems where material will remain in the system.

Robotic dispensing puts specific demands on material properties. In contrast to inkjet printing, where single droplets are required, in robotic dispensing collecting of a continuous strand is crucial (Figure 12). The material properties need to be designed in a way that avoids strut break-up.[120] Schuurman *et al.*[52] could influence drop formation of low-viscous gelatin methacrylamide solutions by introducing high molecular weight hyaluronic acid. Using 20 % w/v gelatin methacrylamide solutions resulted in drop formation at the needle tip. Adding 2.4 % w/v hyaluronic acid changed the viscoelastic properties of the ink and strands could be generated highly improving printing fidelity. As mentioned by Lewis,[121] printing functional 3D structures using robotic dispensing places high demands on the inks. Ideally the inks should even self-support when spanning features need to be printed. When it comes to

building 3D construct layer-by-layer the interaction of substrate and the first layer is crucial and wetting behavior needs to be adjusted. This can be done by choosing the right material combination, the right ink composition,[52] or by surface modification.

Chapter 3

Melt electrospinning onto cylinders: effects of rotational velocity and collector diameter on the morphology of tubular structures

This chapter was already published as original research article:

Jungst, T.; Muerza-Cascante, M. L.; Brown, T. D.; Standfest, M.; Hutmacher, D. W.; Groll, J.; Dalton, P. D. Melt electrospinning onto cylinders: Effects of rotational velocity and collector diameter on morphology of tubular structures. *Polymer International* 2015, *64* (9), 1086-1095.

The original text was slightly modified to improve readability.

The experiments were performed at the Institute for Health and Biomedical Innovations (Queensland University of Technology, Brisbane, Australia). The exchange program was supported by the German Academic Exchange Service (DAAD).

The author contributions to the original research article are as follows:

Contributor	Contribution
Tomasz Jüngst	Designed and performed the experiments; designed and co-built tubular collector; co-wrote and revised manuscript content; provided feedback on the manuscript
Maria L. Muerza-Cascante	Performed part of the characterization with SEM; revised manuscript content; provided feedback on the manuscript
Toby D. Brown	Designed and built melt electrospinning device; revised and provided feedback on the manuscript
Marco Standfest	Designed and co-built tubular collector
Dietmar W. Hutmacher	Revised and provided feedback on the manuscript
Jürgen Groll	Revised and provided feedback on the manuscript
Paul D. Dalton	Conceived and designed experiments; co-wrote, revised and provided feedback on the manuscript

Chapter 3.1: Introduction

There are various routes to the manufacture of tubular structures for biomedical engineering.[122,123] Extrusion,[124] molding,[125,126] dip-coating[127] and solution electrospinning[128,129] are all common approaches for making tubes while lesser used techniques such as centrifugal casting,[130] lithography[131] and more recently biofabrication[132] have also been established. Tubes are key structures for many tissue engineers as they mimic the various anatomical constructions (e.g. blood vessels, urethra,[133] intestine,[134] larynx[135]) of the body.[136] Furthermore, they are employed in clinical strategies, such as stents,[137] bone defects,[138] and nerve guides.[139] Each manufacturing process has its strengths and limitations, from their biological efficacy to challenges in gaining regulatory approval for translation into the clinic.

Solution electrospinning has been one recent processing technique subject to extensive research as a method for design and fabrication of scaffolds for a variety of tissue engineering (TE) applications, including tubes.[134,135,140] To produce a tube by solution electrospinning, a fast-rotating cylindrical collector is commonly implemented to the spinning instrument, and an electrospun mesh is removed after a period of collection time. Due to the dynamic bending instabilities of the solution electrospun jet, the tube walls typically have a random fiber orientation, unless the rotational speed is sufficiently high or an alignment process is used to minimize whipping in one of the planes.[141-144] Nevertheless, collecting fibers on a rotating mandrel is a common approach to produce electrospun tubular scaffolds for research in TE and many workgroups gained initial promising results.[145-147]

Melt electrospinning writing (MEW) can produce both straight and coiled fibers, depending on the translation speed of the collector. It was previously shown that straight fibers can be melt electrospun written onto cylindrical collectors larger than 6 mm diameter for applications in bone TE, when the collector speed is faster than the speed of the jet.[6]

In this chapter, melt electrospinning onto different diameter collectors is performed, and the collector is rotated both below and above the critical transition speed that results in straight fibers. The morphology and structures generated under these conditions are investigated and the dimensions of the fabricated structures are analyzed. Via combining cylinder translation and rotation, tubes with different morphologies and mechanical properties are produced. The aim of this chapter is to identify and analyze the main parameters influencing fiber orientation and structure of tubular melt electrospun scaffolds over a broad range of processing conditions.

Chapter 3.2: Materials and methods

Materials

Medical grade poly(ε-caprolactone) (PCL, Purasorb PC 12) was sourced from Purac Biochem (Gorinchem, NL). The polymer was selected due to its biomedical history, biodegradability and processing capacity. Moreover, the surface properties of PCL as well as its degradation kinetics can be tailored by physical, chemical and biological modifications.[148]

Electrospinning device

A custom-made MEW device was used to fabricate the structures reported in this study (overview shown in Figure 13A). The medical grade PCL pellets were heated in a glass syringe (Hamilton, Reno, USA) with an electrical heater (Watlow Electric Manufacturing Company, St. Louis, USA) mounted to a tailor-made polyether ether ketone (PEEK) housing. A high voltage of 11.5 kV (EMCO High Voltage Corporation, Sutter Creek, USA) was applied and directly measured with a high voltage probe (Tenma Instruments, Springboro, USA). The high voltage was applied to the flat tip of a spinneret and the polymer flow was regulated by a syringe pump (World Precision Instruments, Sarasota, USA) with a feed rate of 15 µL/h. A flat tipped 23 G hypodermic needle was used as the spinneret. The distance between the spinneret and surface of the rotating collector was 20 mm. The melt electrospinning components were

enclosed in a Perspex box fitted with a magnetically coded interlocked door to prevent accidental electrical shocks.

Electrospun melt preparation

The as-received medical grade PCL pellets were placed into a 5 mL syringe and heated up to 100 °C for 2 h to ensure a homogeneous polymer melt. Before sample preparation the material was collected for 30 min on a grounded plate in order to establish a constant and stable jet.

Electrospun fiber collection

Steel piano leadwire (Albion Alloys Ltd, Bournemouth, UK) was used as a rotating cylindrical collector, with different diameters (0.5, 1.0, 1.5, 2.0, 3.0, 4.76 mm). This high-carbon steel was chosen due to its consistent diameter and excellent mechanical properties particularly important for the low diameter collectors. The grounded collectors were rotated by a DC motor (Leadshine Technology Co. Ltd., Shenzhen, China) (Figure 13B) mounted on top of a linear slide (Velmex Inc, Bloomfield, USA). The translation and rotation of the collector was controlled and automated by G-code based CNC software (Mach3, ArtSoft, Newfangled Solutions LLC, Fayette, USA). Collections with rotation only (no translation of the collector) were performed (n=5) with up to four different rotational speeds on one collector (Figure 14B).

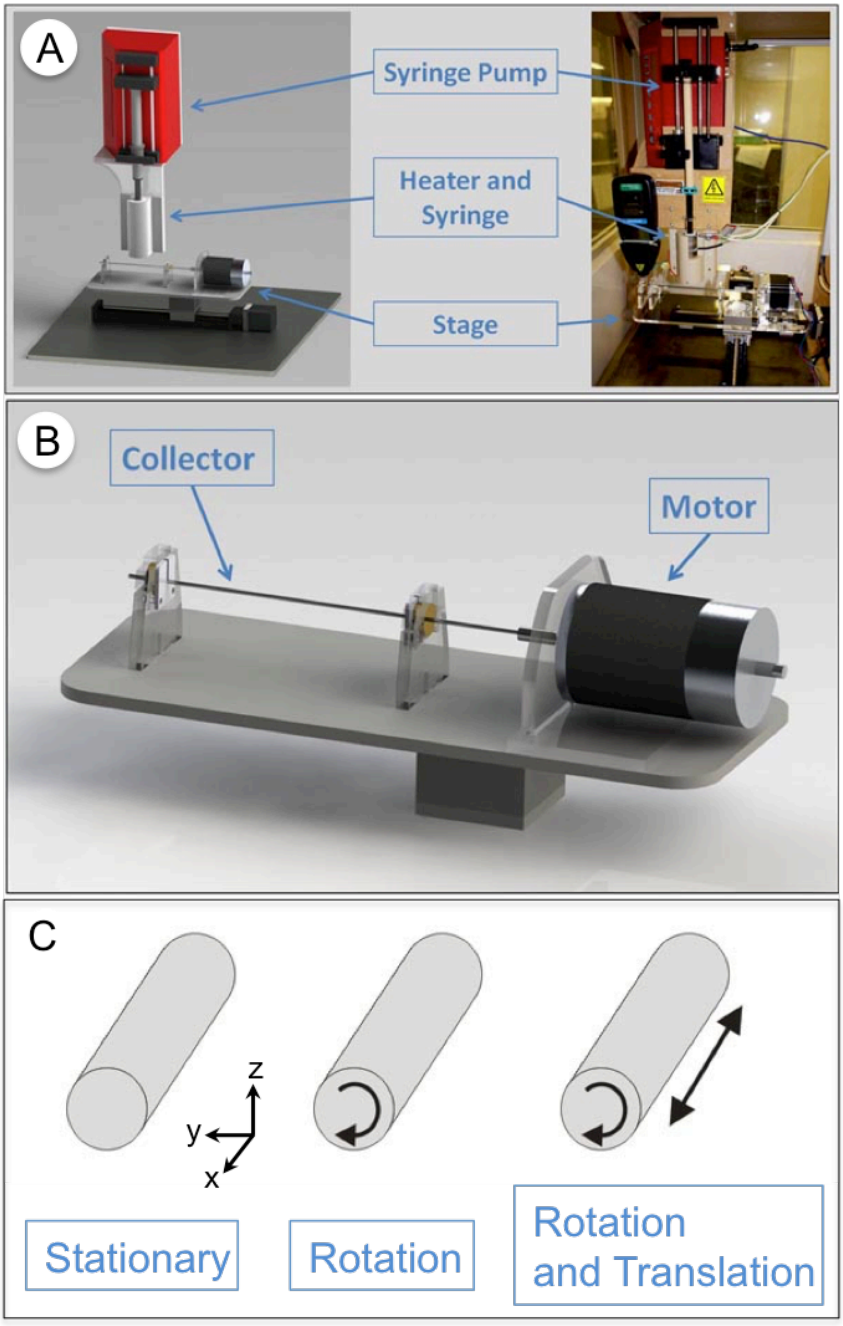

Figure 13: A) Overview Melt Electrospinning Device. A syringe pump was used to dispense the molten material through a spinneret mounted to a heated syringe. The high voltage was applied to the spinneret and the collector was grounded. B) The rotating collector was connected to a computer-controlled DC motor mounted onto a stage and a linear slide. C) The collection was performed with three different modes and varying parameters. The first mode was stationary. No rotation and/or translation was applied. For the second mode the collector was rotated only. For the third mode rotation and translation along the x-axis was undertaken. Reprinted with permission from [18]. Copyright (2017) John Wiley and Sons.

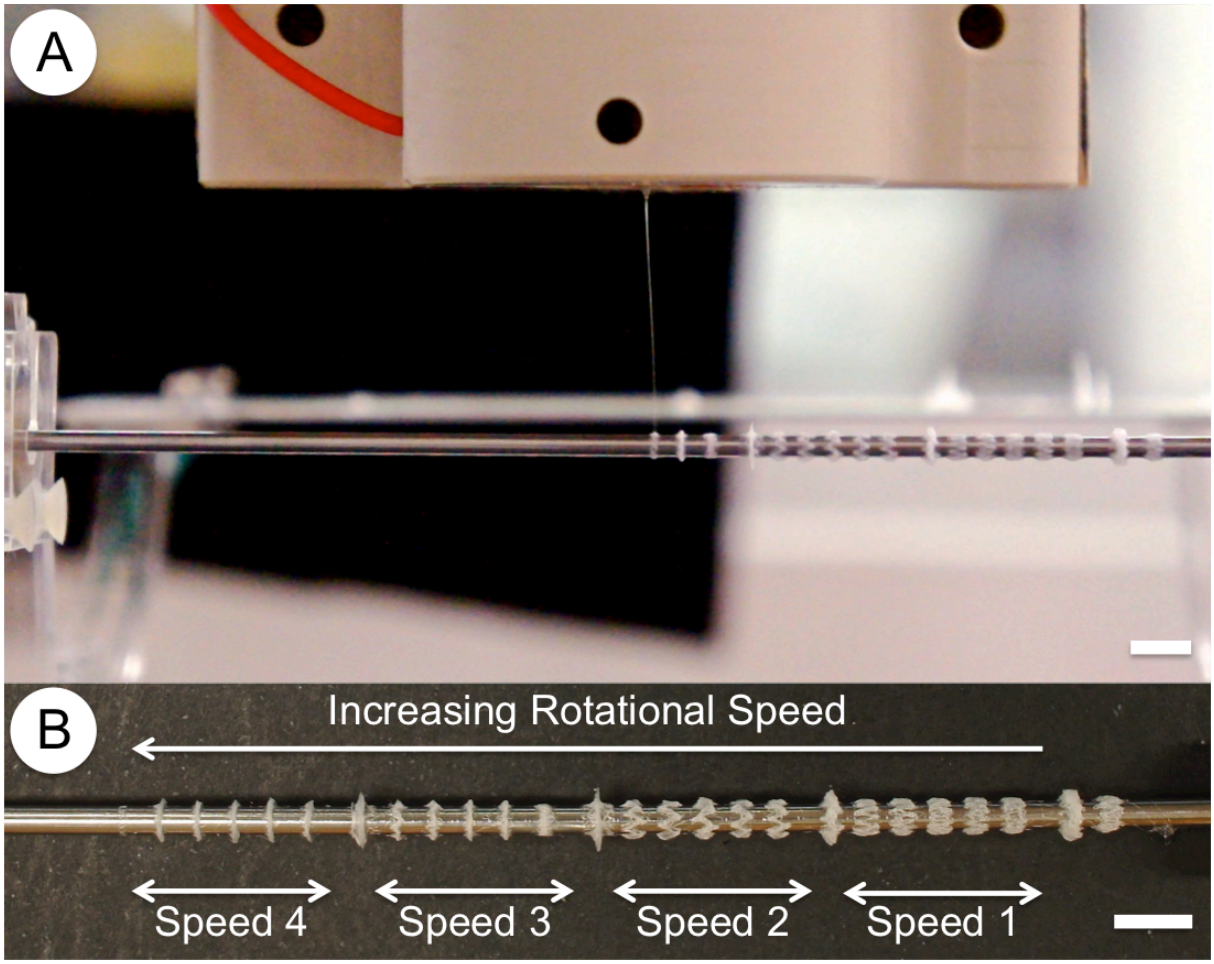

Figure 14: Collection with rotation only. A) The jet of molten polymer was collected onto a rotating rod. After the sample was finished the stage was translated and the next sample was generated. B) Samples with up to four different rotational speeds could be collected in quintuplicates onto one rod. Before collection with a different rotational speed material was collected for two minutes to ensure an adjustment of the jet to the new conditions. Scale bars are 6 mm. Reprinted with permission from [18]. Copyright (2017) John Wiley and Sons.

Visualization of tubular structures

Samples were mounted on SEM aluminum stubs and gold coated with a sputter coater (Leica Microsystems EM SCD005, Leica Microsystems GmbH, Wetzlar, Germany). Then scanning electron microscopy (SEM) was performed with an FEI Quanta 200 Environmental SEM (FEI Company, Hillsboro, United States) at a voltage of 10 kV and a tabletop SEM (TM3000, Hitachi, Tokyo, Japan) at a voltage of 15 kV. Optical images were taken with a SteREO Discovery.V20 Stereomicroscope (Carl Zeiss, Oberkochen, Germany). Images were prepared and processed using Photoshop CS5 12.1 (Adobe, San Jose, USA).

Fiber diameter, orientation and tube width measurement

SEM images were imported into Image J software (National Institute of Health, USA). The fiber diameter for each line was measured at 10 random locations. Similarly, the tube width and the length of the stationary collections were measured using a square drawn along the edges of the tubes to define the outer bounds. The orientations of the fibers were also analyzed drawing lines along the fibers and detecting the angle between the lines at 10 random positions. The calculated errors correspond to the standard deviation of the measurements.

Chapter 3.3: Results and discussion

Results

The polymer and instrument conditions used in this study produced a straight electrified jet that had minimal or no bending instabilities (often described as "whipping") (Figure 14A). Instead the electrified molten jet moved directly towards the collector with fiber coiling due to buckling instabilities associated with a viscoelastic liquid impinging onto a solid surface. For all experiments, if the voltage to the spinneret is turned off, then the molten electrified jet would break down and fiber collection would stop.

Stationary fiber collection

The fiber preferentially deposits along the flat part of a stationary cylindrical collector (along the length of the cylinder). The deposited fiber loops back to the mid-line once it reaches a certain distance from the mid-line, due to the viscoelasticity of the molten PCL jet. This back and forth fiber deposition along the collector is continuously repeated and the result is a stacked object (Figure 15).

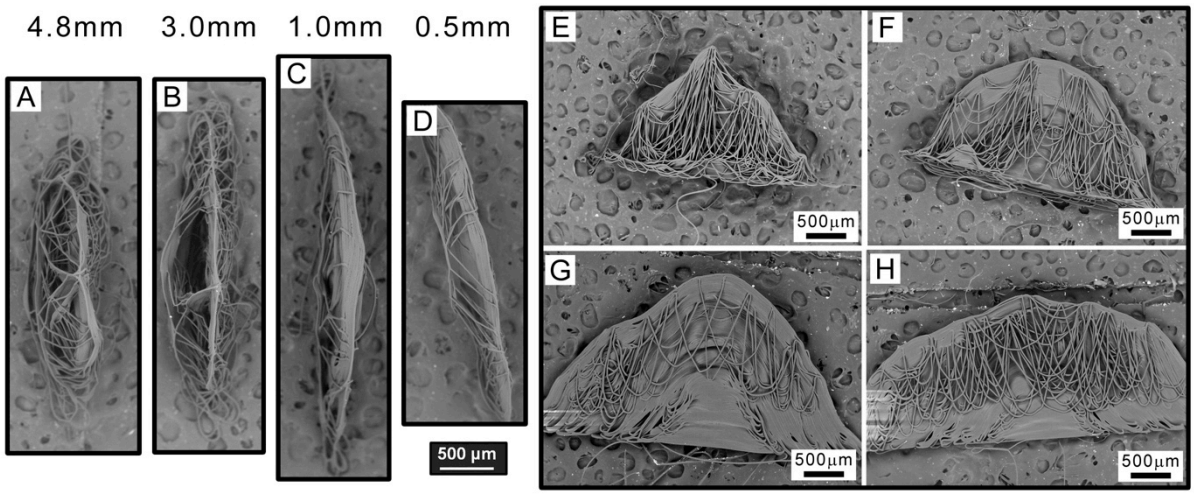

Figure 15: Melt electrospun PCL after 60 s of collection onto stationary collectors of varying diameter. The largest diameter collector (4.8 mm) produced an oval shaped collection (A) with many fibers not stacking well upon each other. The side-view (E) reveals a collected mesh with numerous dangling fibers. This is also seen for the 3.0 mm collector (B/F), however for the 1.0 mm (C/G) and the 0.5 mm (D/H) there was far more accurate stacking. The collected mesh became longer and the accuracy of the fiber stacking improved, until a certain height after which dangling fibers can be seen coming from the sides of the object. Reprinted with permission from [18]. Copyright (2017) John Wiley and Sons.

The melt electrospun fiber morphology, but not the fiber diameter (Figure 16B), is influenced by the collector diameter. The collected material (Figure 15) has dimensional differences that reflect the effect of collector curvature on the deposition behavior. All collections are anisotropic and have an oval shape when viewed from above. As the collector diameter increases, the length of the deposited construct decreases. As shown in Figure 16A the length of the constructs decreased from 1.99 ± 0.13 mm for the 0.5 mm collector diameter to 1.22 ± 0.04 mm for a 4.8 mm diameter. Furthermore, the deposited material width increases with collector diameter (Figure 15).

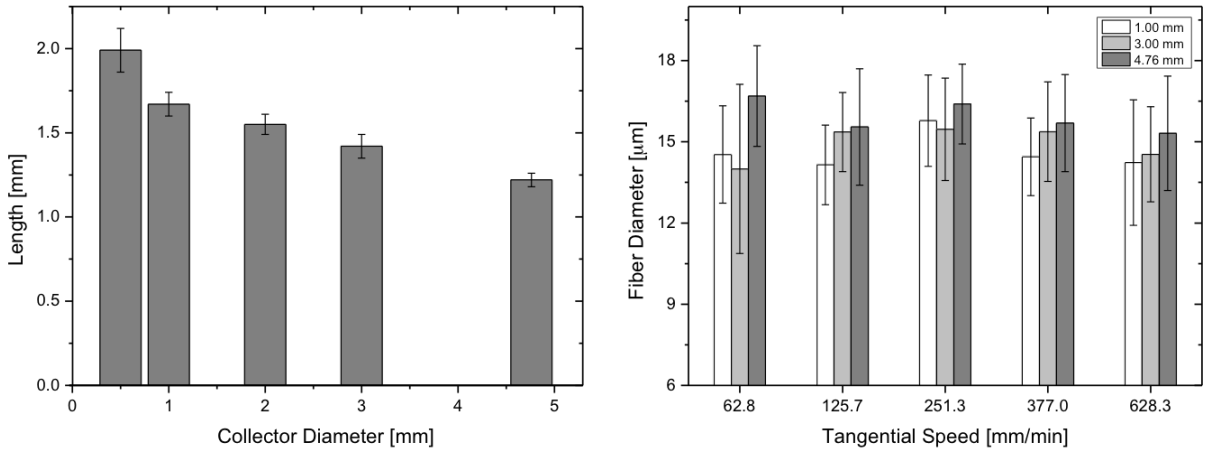

Figure 16: A) Construct length of samples collected under static conditions (no rotation, no translation). With increasing collector diameter, the length of the constructs decreases. B) Fiber diameter in dependence of the transverse speed for the collector diameters 1.00 mm, 3.00 mm, and 4.76 mm. Within the errors of the measurement there is no difference of the fiber diameter according to the collector diameter and the tangential speed. Reprinted with permission from [18]. Copyright (2017) John Wiley and Sons.

Rotational velocities below the critical translation speed

When the collector is rotated without stage translation in the x direction (Figure 13C), the melt electrospun fibers were produced as a "ring" that could be readily removed from the collector. These structures had morphologies that were dependent on the rotational velocity. Figure 17 and Figure 18 show the trend of changes for 4.8 mm and 3.0 mm diameter collectors. While not as defined, the same morphological trend could be observed for 1.0 mm and 0.5 mm diameter collectors (Figure 19). There appear to be two distinct phases within the fiber morphology if processed below the critical translation speed. The first, observed at low rotational speeds is the "figure of eight" looping (Figure 17 and Figure 18 lines A and B), where the rotation is slow enough to allow translation along the collector to occur. The next phase is a sinusoidal fiber pattern which occurs as the collector rotational velocity increases towards the critical translation speed of the fiber and the forces on the fiber due to rotation are increased (Figure 17 and Figure 18 lines C and D).

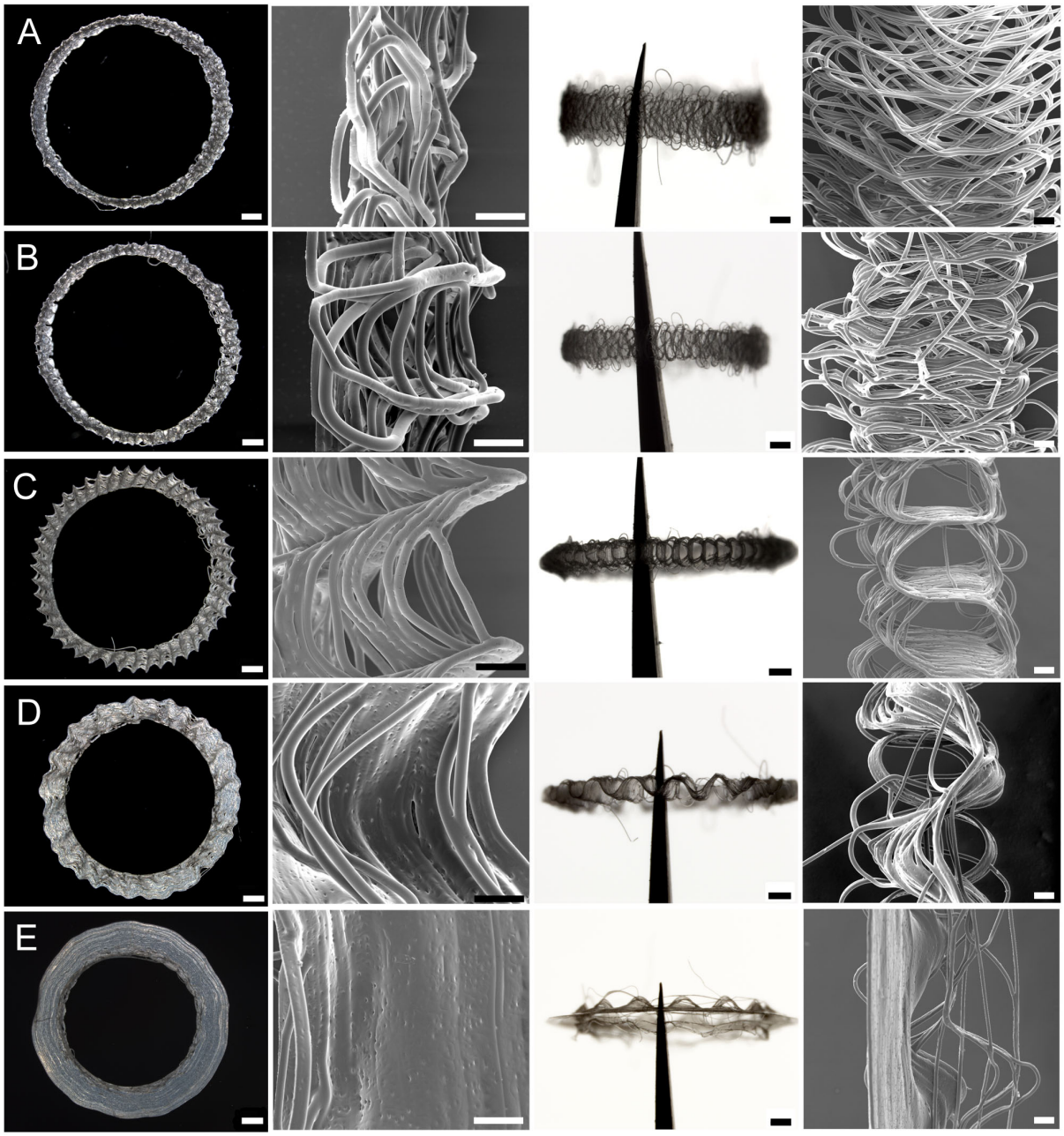

Figure 17: Effect of rotation speed on the collected material. Collector diameter 4.8 mm. Each line shows samples collected under the same conditions from different views. The rotational speeds starting from line A to line E are: 0.4 rpm, 4.2 rpm, 8.2 rpm, 16.8 rpm, 25.2 rpm, 42.0 rpm. Each column shows samples collected at different rotational speeds from the same view. The views starting from left to right are: stereomicroscopic image with overview from the side, SEM image with close up view on the sample from the side, stereomicroscopic image from the top, SEM image with close up view on the sample from the top. Scale bars are 500 µm, 100 µm, 500 µm and 100 µm for each column starting from left to right. Reprinted with permission from [18]. Copyright (2017) John Wiley and Sons.

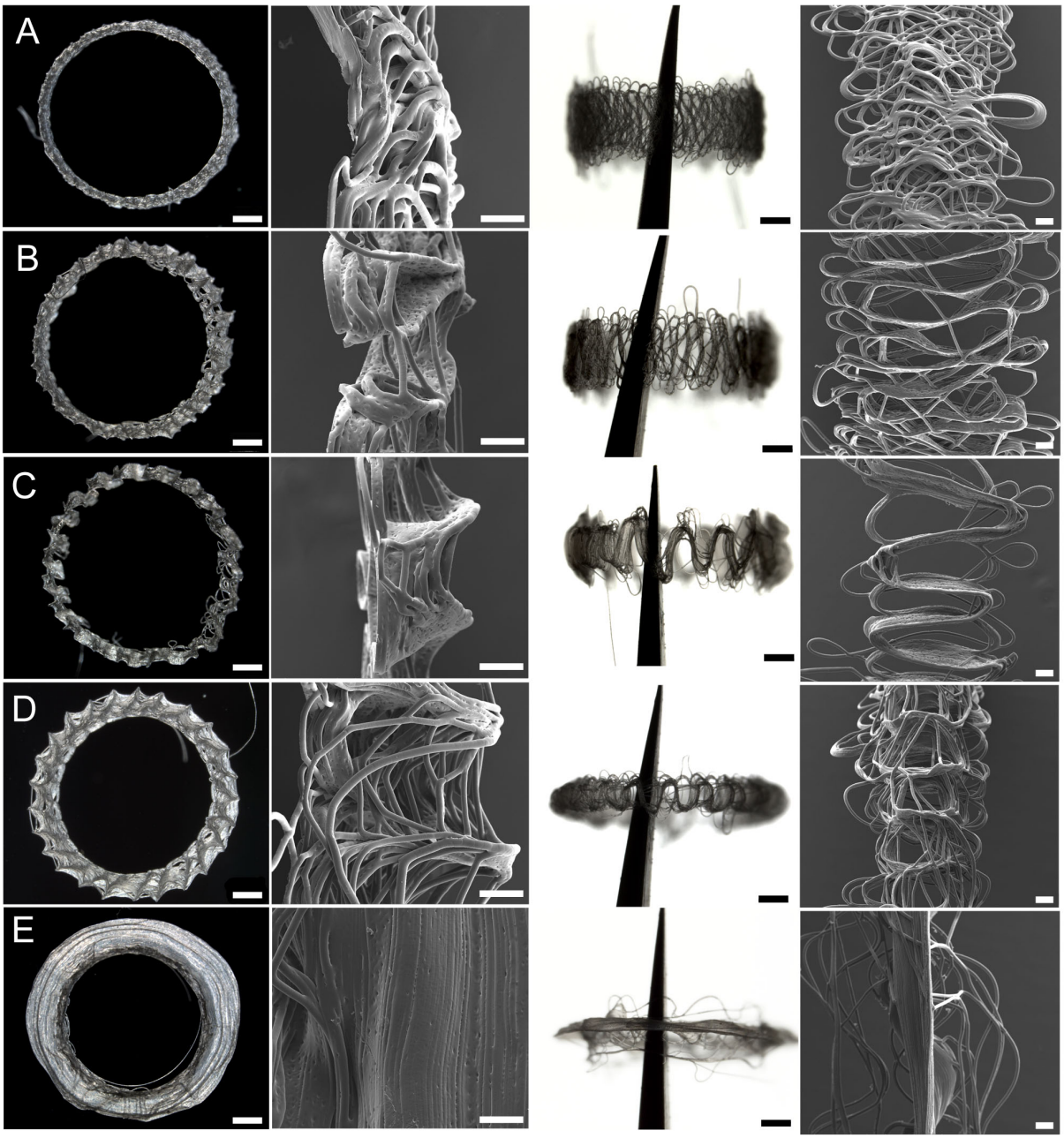

Figure 18: Effect of rotation speed on the collected material. Collector diameter 3.0 mm. Each line shows samples collected under the same conditions from different views. The rotational speeds starting from line A to line E are: 0.7 rpm, 6.7 rpm, 13.3 rpm, 26.7 rpm, 40.0 rpm, 67.0 rpm. Each column shows samples collected at different rotational speeds from the same view. The views starting from left to right are: stereomicroscopic image with overview from the side, SEM image with close up view on the sample from the side, stereomicroscopic image from the top, SEM image with close up view on the sample from the top. Scale bars are 500 µm, 100 µm, 500 µm and 100 µm for each column starting from left to right. Reprinted with permission from [18]. Copyright (2017) John Wiley and Sons.

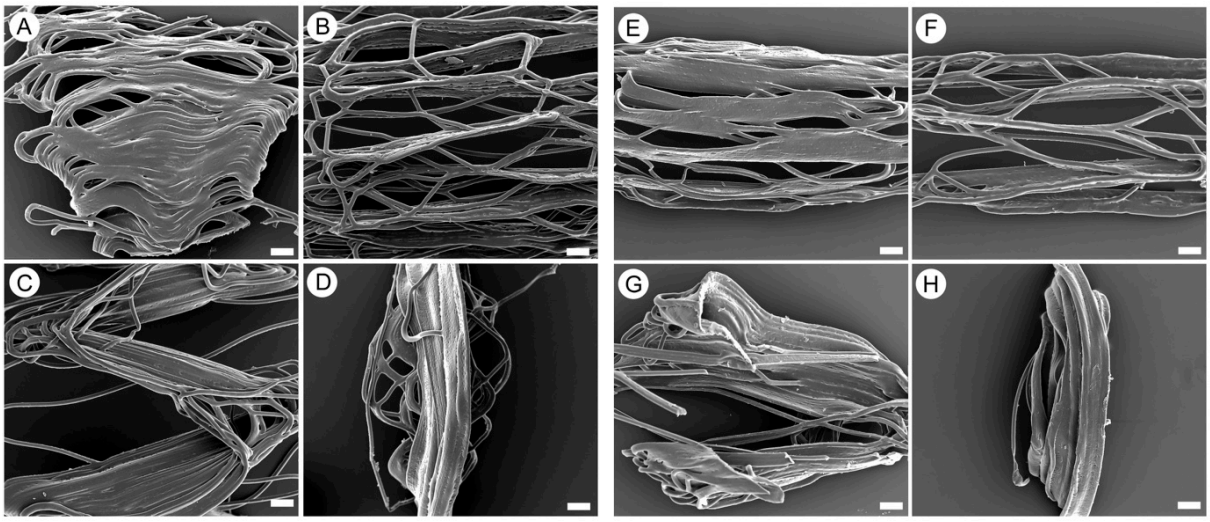

Figure 19: Effect of rotation speed on the collected material. A-D show magnifications of samples collected onto 1.0 mm diameter rods from the top. The rotational speeds from A-D are 2 rpm, 20 rpm, 80 rpm and 200 rpm. Images E – H show samples collected onto a 0.5 mm collector with rotational speeds from E – H of 4 rpm, 40 rpm, 160 rpm, 400 rpm. Scale bar is 100 µm. Reprinted with permission from [18]. Copyright (2017) John Wiley and Sons.

Rotational velocities above the critical translation speed

At higher angular velocities, the critical translation speed is passed and the electrified molten jet is deposited as a linear fiber onto the collector (Figure 17 and Figure 18 line E). However, the stacking of fibers occurs very rapidly, and the structure is built very quickly. This is reflected in Table 1 where the dimensions of the collected "ring" material are displayed. There is a substantive reduction in the width of the ring as speeds are increased and stacking occurs (Table 1). Surprisingly, and as shown in Figure 15B the fiber diameter did not decrease even for constructs collected above the critical speeds. The increased mechanical drawing of the fiber is therefore believed to increase the mass flow to the spinneret, and in the course of this inquiry the fiber diameter is maintained.

Table 1: Width of collected rings. This table shows the measured width of the rings collected with rotation only for different collector diameters and different tangential speeds.

tangential speed [mm/min]	1.00 mm collector diameter [mm]	3.00 mm collector diameter [mm]	4.76 mm collector diameter [mm]
62.8	1.56 ± 0.12	1.23 ± 0.08	1.27 ± 0.09
125.7	1.61 ± 0.09	1.16 ± 0.13	1.13 ± 0.11
251.3	1.49 ± 0.13	1.04 ± 0.12	0.70 ± 0.10
377.0	1.25 ± 0.16	0.71 ± 0.08	0.62 ± 0.06
628.3	0.38 ± 0.06	0.51 ± 0.06	0.50 ± 0.06

Combining rotation above the critical translation speed with collector movement

To produce defined tubes with linear filaments, the x-direction translation was performed in combination with collector rotation. As shown in Table 2 for a 2.0 mm diameter collector the winding angle could be varied between 6 ± 1° and 61 ± 6° by changing the combination of translational and rotational speed. Within the errors, all calculated angles corresponded to the measured winding angles. When the rotation/translation of the collector was controlled so that the fiber is predicted to deposit evenly across the surface, then a defined tubular structure could be formed (Figure 20). Increasing the rotational speed in combination with low translation speeds even further results in a compact tube with low porosity (Figure 21). These dense walled tubes were tightly wound around the 1.5 mm collector, however could be readily released from the metal collector by using 70% ethanol. The tubes had an outer diameter of 2.13 ± 0.06 mm and an inner diameter of 1.43 ± 0.03 mm, corresponding to an average wall thickness of 0.35 ± 0.04 mm. The maximum length

of the tubes produced was 60 mm, and the average fiber diameter was 11.19 ± 0.77 µm.

Table 2: Parameters for created tubes. Tubes were collected with different combinations of rotation and translation of the collector. Each combination resulted in a calculated winding angle that, within the errors, corresponded to the measured angle.

collector diameter [mm]	calculated angle [degrees]	effective velocity [mm/min]	rotational speed [rpm]	tangential speed [mm/min]	translational speed [mm/min]	measured angle [degrees]
2.0	5	600	8	52	598	6 ± 1
2.0	15	600	25	155	580	16 ± 3
2.0	30	600	48	300	520	30 ± 2
2.0	45	600	68	424	424	46 ± 3
2.0	60	600	83	520	300	61 ± 6

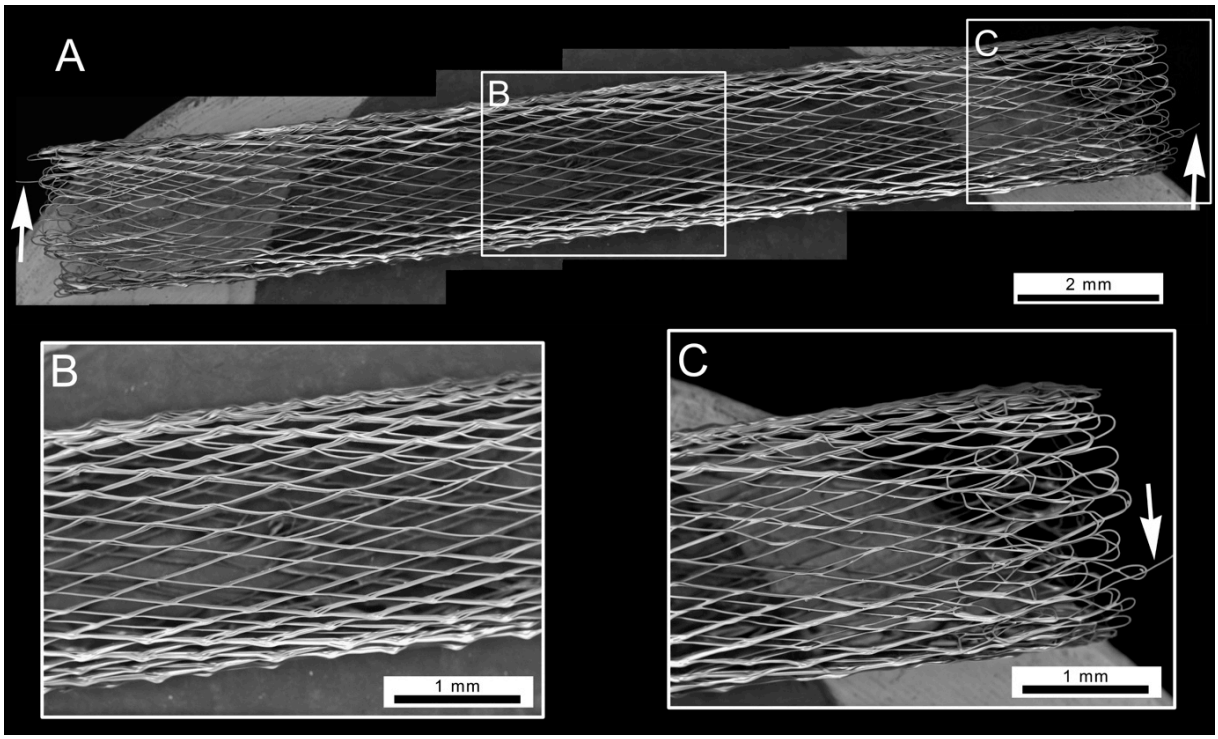

Figure 20: Collection with rotation and translation. The image shows a tube collected onto a 2.0 mm diameter rod. The calculated winding angle was 5°. The tube was created by repeatedly stacking one continues fiber on top of itself using translation and rotation of the collector. The white arrows indicate the incoming and outgoing fiber. A) Overview image of the tube. B) Magnification of the center part of the tube. C) Magnification of one of the edges of the tube. Reprinted with permission from [18]. Copyright (2017) John Wiley and Sons.

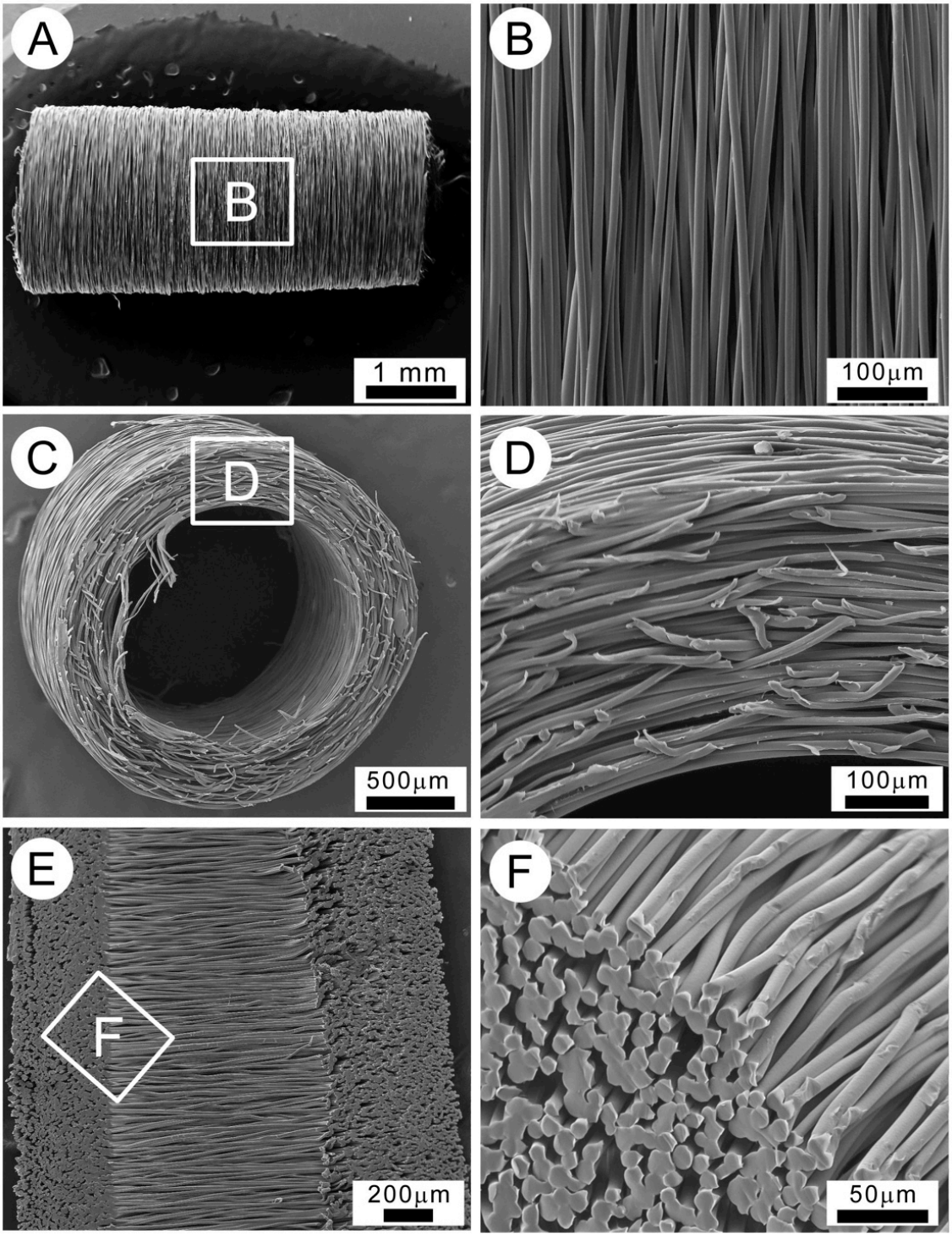

Figure 21: SEM images of a melt electrospun tube manufactured at high rotations speeds (6600 rpm) onto a 1.5 mm diameter collector. A) Overview image of the tube. B) Magnification of the tube showing fiber alignment. C) Top view image and D) magnification image of the top view showing oriented fibers compacted into a dense wall. E) Cross-section and F) magnification of the tube showing fusion between the oriented fibers. Reprinted with permission from [18]. Copyright (2017) John Wiley and Sons.

Discussion

In the context of this study, it is important to emphasize that the electrified jet takes a direct path from the spinneret to the collector, with minimal deviation from the mid-line (until right at the collector). The resultant coiling is therefore due to the buckling of a viscoelastic liquid (the molten jet) as it impacts the collector, similar to how other viscoelastic materials (such as honey) coil and buckle as they land onto a surface.[149] When this electrified viscous, molten jet is moved across a surface with increasing speed, the coiling is reduced until it produces a straight fiber.[38] However, when deposited upon a stationary, flat surface for a period of time, the collection is typically circular in shape, often with fibers collected in rings forming radially outwards from the center.[36]

Stationary collection

The fiber deposition onto a stationary cylindrical collector is significantly different from that of a flat surface. The fibers will tend to deposit along the length of the cylinder due to electrostatic forces attracting the jet to the highest point on the collector. Once the deposited fiber reaches a certain distance away from the mid-line, retractile forces in the electrified jet draw back the filament along the collector to the midline. At the point of retraction, the fiber makes a small loop on the collector, indicated in Figure 15. When at the mid-line the depositing fiber continues to the opposing side of the collector, along the length of the cylinder until retractile forces cause the fiber to loop again and return to the mid-line.

It was observed that larger collectors have more oval shaped collections, while the smallest diameter collectors produce a "fin" that is built via a series of stacked fibers. By measuring the length of the collected constructs, it could be shown that as the diameter of the collector increases the length of the constructs decreases (Figure 16A). SEM images taken of the side of the sample show that stacking of the fiber is more pronounced at smaller collector diameters, fibers often failed to deposit upon

each other and so "draped" themselves on the side of the collected material (Figure 15).

Rotating the collector only

The surface of the collector, when rotated, allows the viscous jet to be collected in a more controlled manner. At low rotation speeds, the fiber is now pulled in two axes (x-y) rather than the x axis only. Similar to the stationary collection, the diameter has an effect on the morphology of the melt electrospun material when the collector is rotating. To analyze this effect, experiments with the same tangential speed of the collector surfaces in relation to its rotational axis were performed. For all investigated collector diameters increasing the speed led to linear stacking of the fibers. As previously mentioned, moving the collector at tangential speeds lower than the critical translation speed led to "figure of eight" looping (Figure 17 and Figure 18 lines A and B). Increasing the speed further resulted in a sinusoidal pattern for the collected fibers. When the rotation speed is such that one full rotation of the collector led to an inversely phased deposition of sinusoidal fibers, cylindrical pores resulted (Figure 17C). Collecting fibers with tangential speeds higher than the critical translation speed led to aligned and stacked fibers. Increasing the speed lead to more aligned fibers and thus to a decrease in the width of the collected ring (Table 1). Comparing the structures made with the same tangential speed on collectors with different diameters shows that below the critical translation speed an increasing collector diameter decreases tube width. This observation also fits to the observations made for stationary collections. The influence of the collector diameter becomes particularly prevalent when comparing the structures where the tangential speed generates sinusoidal fibers. The smaller the collector diameter, the bigger the amplitude of the sinusoidal fibers (Figure 17 and Figure 18 lines C and D, Table 1 tangential speeds 251.3 and 377.0 mm/min) due to the electrostatic forces that drive the fibers to the highest point of the collector. This allows a limited control of the self-orientation of the fibers into shapes and structures. Comparing the tube width for the

smallest tangential speeds listed in Table 1 for each diameter respectively show no/or only small reduction in tube width. Here the rotational speed was too small to force the fibers in y-direction (Figure 13C) to a level where the tube width is reduced significantly. Comparing e.g. Figure 18 lines A and B that correspond to the tangential speed of 62.8 and 125.7 mm/min for the 3.0 mm mandrel in Table 1 shows that while the values for the tube width are similar, the morphology of the rings changes significantly. At a velocity of 125.6 mm/min the "figure of eight" shape was distinct; more fibers stacked upon each other rather than next to the previous layer due to the increased tangential speed compared to 62.8 mm/min. At tangential speeds underneath the critical translation speed the deposition of fibers is not forced in a distinct direction but by changing the conditions (collector diameter, tangential speed) during collection it is possible to gain control over the shape and structure of the rings. The change of conditions shows clear trends illustrated by the conversion of the shapes could also be seen when using smaller diameter collectors (0.5 and 1.0 mm) (Figure 19). The "figure of eight" shapes where not as distinct as for the bigger diameter collectors (3.0 and 4.8 mm) because the electrostatic forces made the fibers tend to deposit along the length of the cylinders for longer. When rotating slowly fibers preferentially stacked on top of each other suppressing the clear "figure of eight" collection. Nevertheless, a conversion into sinusoidal (Figure 19 C and G) and linear shapes was observed (Figure 19 D and H).

Figure 22B shows a magnification of a construct collected onto a 2.0 mm diameter collector rotated at 10 rpm (Figure 22A). It can be seen that the collected fibers were still molten and could fuse with the underlying fibers. This fusion increased the stability of the constructs and helped preserve their shape. Hierarchical effects can also be seen in Figure 22C and D. Both constructs were collected under the same conditions and are shown from the same perspective. The construct shown in Figure 22C was collected for 60 s whereas the construct in Figure 22D was collected for approximately 30 min. These experiments were performed under a constant rotational

speed, and the tangential speed increased during collection with increasing construct thickness. To suppress these additional influences the collection time was adapted to the collector diameter ensuring that the mandrel rotated the same number of times for each diameter and initial tangential speed.

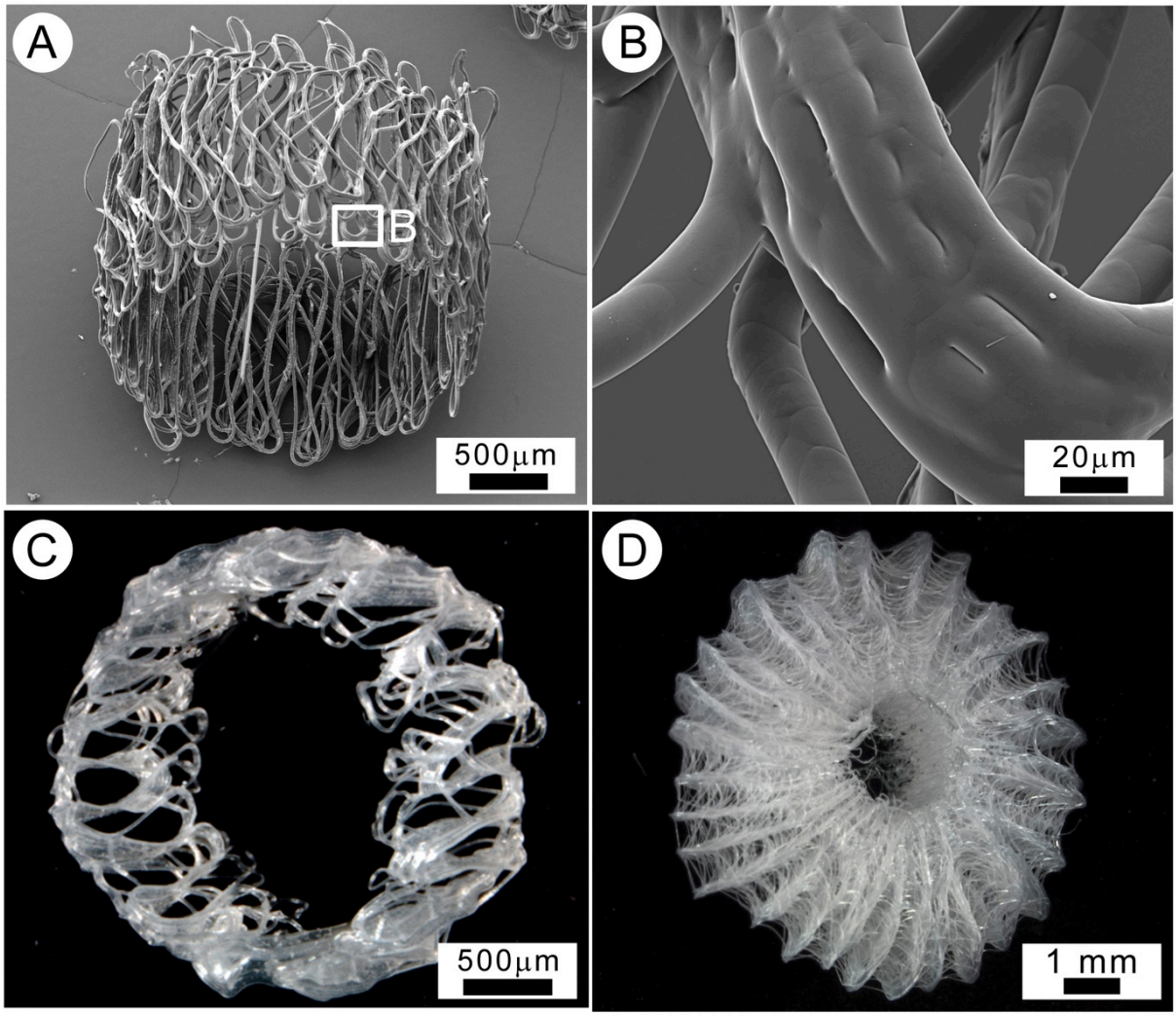

Figure 22: Collection onto 2.0 mm diameter collectors with rotation only. Image A and B show different magnification of a tube collected at 10 rpm. As visible in magnification B the fibers can melt together after being collected on top of each other. C and D show images of constructs collected at a rotational speed of 20 rpm for different times. C was collected for 60 s while D was collected for about 30 min. Reprinted with permission from [18]. Copyright (2017) John Wiley and Sons.

Rotation and translation of the collector

If the tangential speed of the tube was reduced relative to the translational speed by reducing the rotational speed, as shown in a previous work[6] different

combinations of rotation and lateral translation speeds of the tube resulted in a varied effective velocity vector, comprised of a winding speed and winding angle (i.e. the angle between the fiber direction and the axis of collector rotation). Table 1 demonstrates for a 2 mm diameter tube with a programmed length of 15 mm that different combinations of rotational and translational speed could be used in order to achieve a desired effective winding angle, for tubes fabricated using a 16 ± 2 μm diameter fiber. In contrast to previous work,[6] it was possible to adapt the real tube width to the measured one by laying down the fibers at effective speeds that are just as high as the translation speed (about 600 mm/min). Further, it was demonstrated that the design and fabrication of tubular scaffolds via direct writing in a melt electrospinning mode is viable with significantly reduced fiber diameters (from 60 μm down to 16 μm) and for smaller structures (tubular construct diameter reduced from 6 mm to 2 mm), where tailoring of the pore architecture to suit a specific TE application is maintained.

The permutations of combining rotation/translation are considerable and their full characterization is beyond the scope of this chapter. However, melt electrospinning at high tangential speeds and low translational speeds results in fiber orientations that are almost perpendicular to the rotational axis. Figure 21 shows the cross section of a tube with 350 ± 40 μm thick walls fabricated at high rotating speeds to create aligned fibers. In this case the structure has been melt electrospun on a 1.5 mm diameter tube, where the rotational speed of the tube (6600 rpm) is significantly higher relative to the translational speed 1500 mm/min of the tube. The high rotational speeds lead to a mechanical drawing of the fibers that have been wound closely together to create a tightly packed structure that would likely limit the penetration of cells/tissue. For such tubes, the inner diameter of the tube was 1.43 ± 0.04 mm.

Chapter 3.4: Conclusion

While MEW has primarily been performed on flat surfaces, in this investigation cylindrical collectors were used. The deposition behavior of the melt electrospun fibers onto cylinders differs from that typically seen with solution electrospinning. In particular, the fiber will tend to deposit along the length of the collector due to curvature of the cylindrical collector. Using a static collector (no rotation or translation), fibers can be readily observed to align along the length of the cylinder. This effect is seen for all the cylindrical collectors used in this study, from 0.5 mm up to 4.76 mm. In comparison, fibers collected upon flat surfaces will form a circular deposit of fibers.[36]

Slowly rotating the collector results in a "figure of eight" morphology, which is believed to be assisted by the surface curvature. Increasing the rotational speed further induces a sinusoidal pattern within the collected material. A further increase to rotational speeds that exceed the critical translation speed of the jet leads to aligned fibers. It could be shown that the diameter of the cylindrical collector has a significant influence on the collected rings. The large collector diameters resulted in thinner rings. The width of the rings further decreased with increasing rotational speeds. At tangential speeds above the critical translation speed (experiments run at 628.3 mm/min) the tube width started to equilibrate due to the collection of linear fibers (see Table 1).

When translating the collector during rotation at medium speeds it was possible to adjust the winding angle between 6 ± 1° and 61 ± 6°. Collecting at effective velocities about the critical translation speed of the jet enabled building constructs with different mesh geometries predefined by the winding angle. Further increasing the rotational speed led to fibers that were aligned almost perpendicular to the axis of rotation. The resultant constructs were wound closely together creating tightly packed structures.

In summary, it was possible to influence the structure of tubular constructs by changing the rotational speed of the collector, by additionally translating the collector, and by choosing the correct collector diameter. The resulting tubular structures had a unique architecture not previously described and have potential to be studied in different areas of TE such as bone, vascular and nerve regeneration.

Chapter 4

Printable hydrogels as nanoparticle release systems

This chapter was published as original research article:

Baumann, B.*; Jungst, T.*; Stichler, S.; Feineis, S.; Wiltschka, O.; Kuhlmann, M.; Linden, M.#; Groll, J.# Control of nanoparticle release kinetics from 3D printed hydrogel scaffolds. *Angewandte Chemie International Edition* 2017, *56* (16), 4623-4628.

* Bernhard Baumann and Tomasz Jüngst contributed equally.

Mika Linden and Jürgen Groll share corresponding authorship.

The article was re-written and supplemented with additional experiments to represents the work that was performed by Tomasz Jüngst.

The author contributions to the original research article are as follows:

Contributor	Contribution
Tomasz Jüngst	Designed and performed printing experiments as well as rheological analysis; co-wrote and revised manuscript content; provided feedback on the manuscript
Bernhard Baumann	Designed and performed mesoporous silica nanoparticle release and cell uptake studies; co-wrote and revised manuscript content; provided feedback on the manuscript
Simone Stichler	Functionalized pre-polymers; developed and prepared hydrogel-based inks
Susanne Feineis	Functionalized gold-nanoparticles; designed and performed gold-nanoparticle release study
Oliver Wiltschka	Performed 2D cell culture and assisted in uptake studies; provided feedback on the manuscript
Matthias Kuhlmann	Synthesized pre-polymers for ink systems; revised and provided feedback on the manuscript
Mika Linden	Conceived and designed experiments; revised and provided feedback on the manuscript
Jürgen Groll	Conceived and designed experiments; revised and provided feedback on the manuscript

Chapter 4.1: Introduction

Nanoparticles can be used to deliver drugs directly to cells. As shown by Wiltschka *et al.*,[150] cells can take up mesoporous silica nanoparticles (MSN) that are loaded with drugs and the MSN can then release the drugs directly into the cells. The same group could further prove that the released drug can influence the cellular behavior as shown by Mamaeva *et al.*,[8] where enhanced glucose uptake by tumor-initiating cells, in this case breast cancer stem cells, was used to address the uptake of glucose functionalized MSN. The particles were further loaded with Notch activity inhibitors, γ-secretase inhibitors, that were released after uptake based on recognition of the particles by glucose receptors present in glycolytic cancer cells. Mamaeva *et al.* also show that these MSN reduced the cancer stem cell pool in vivo. Although this example shows an elegant method of controlled delivery and release of bioactive molecules, the controlled temporal release of drug vectors still remains a challenge in the field of Nanomedicine.

This challenge is addressed within this chapter where differently charged MSN – used as model systems for drug vectors – were combined with a printable hydrogel system containing negatively charged hyaluronic acid. This ink was synthesized as described in literature.[42] Within this work, it was shown that the electrostatic interactions between the nanoparticles and the hydrogel can be used to control the temporal release of MSN. Furthermore, the electrostatic interactions also changed the diffusion/migration properties of the particles within the hydrogel ink and thus enabled a control of particles species concentrations based on direct contact of printed strands and thus on the geometry. It was proved that the geometry of the constructs made from differently charged particles could be used to control particle concentrations within the strands and thus the printability of the materials offers an additional control over release kinetics. Because charged nanoparticles are known to alter rheological properties of hydrogels,[151,152] a crucial part of this chapter was also the rheological evaluation of the MSN-loaded ink systems and the analysis of the

impact of the particles on the ink´s printability. Maintaining the printability of MSN loaded inks is also highly interesting for the field of biofabrication where it could be used to generate gradients of different particle and drug concentrations introducing a hierarchy and potentially altering the tissue maturation properties. Printability in combination with controlled release of drug vectors could further help developing inks that determine post-printing fate of cells that are either within the ink or influenced by the released particles and drugs.

Chapter 4.2: Materials and methods

The MSN were produced by Bernhard Baumann as described in Baumann *et al.*[153] The silica particles had an average diameter of about 400 nm at a mesopore diameter of about 3 nm. They were functionalized either with carboxy- or with ammino-groups covalently coupled to the inorganic particles. The MSN-COOH had a zeta-potential of -21 mV and the MSN-NH_2 a potential of +20 mV measured in 25 mM phosphate-buffer saline (PBS) solution. Furthermore, covalently label particles were produced. Both MSN-types were labeled with ATTO dyes, ATTO 488-NHS and ATTO 647N-NHS, for fluorescence analysis.

The polymers were synthesized and characterized by Simone Stichler as described previously.[153] The two synthesized polymers, linear Poly(allyl glycidyl ether-*co*-glycidyl) (P(AGE-*co*-G)) and thiol functionalized poly(glycidol) (PG-SH), enable a UV induced cross-linking via thiol-ene click reaction in the presence of a photoinitiator (Irgacure 2959).

For the ink preparation, the MSN were suspended in PBS at a concentration of 10 mg/mL. The first half of the suspension was mixed with P(AGE-*co*-G) and the photoinitiator (final concentration of 0.05 wt.-%). Then, PG-SH was added to the other half of the MSN suspension. Afterwards, both solutions were mixed together and 3.5 wt.-% hyaluronic acid (1.36 MDa) was added as purchased to adjust the ink viscosity and thus to increase shape fidelity for printing. The amount of polymer

needed for the thiol-ene click reaction added to the final ink was adjusted to result in an equimolar functional group ratio and was 17 wt.-%. Using this method three different MSN-inks were prepared: an ink containing MSN-COOH only, one containing only MSN-NH_2, and one containing both species.

Printing of the MSN-inks was performed with a 3DDiscovery bioprinter (regenHU). The device was equipped with two print heads enabling processing of hydrogel inks. One of them works on a time-pressure principle (syringe dispenser, DD-135N) and was equipped with a flat tipped precision needle (0.33 mm inner diameter, 23 G, 6.35 mm length, Nordson EFD). The pressure used to dispense the material was set to be 1.5 bars. The other print head was an electromagnetic valve dispenser (cell friendly print head, CF-300N/H) dispensing material through a 0.30 mm flat tipped needle (regenHU). Printing was performed at valve opening times of 800 µs, a dosing distance of 45 µm, and a feed pressure of 3.4 bars. Both print heads were operated at 15 mm/min and the syringe dispenser was only used in case of two component constructs. Cross-linking of the deposited material was achieved by irradiating the dispensed material with UV-light using an hönle UV source at 60 % intensity (bluepoint 4, 320-390 nm filter). The illumination pulses had durations of 2 sec and were applied 7 times per construct during printing. Shape fidelity was analyzed with a Carl Zeiss SteREO Dicsovery.V20 optical microscope post-fabrication. More detailed shape fidelity analysis via 3D reconstruction as well as particle release and migration within the two component constructs was performed by confocal microscopy using a Leica TCS SP8 STED.

The rheological properties of the different MSN containing inks were analyzed and compared to the particle free ink system measuring them with an Anton Paar Physica MCR301 rheometer in a cone-plate setup (60 mm diameter, 0.5°, gap 0.058 mm). A solvent trap was used to minimize evaporation and material changes during testing at room temperature. To acquire detailed information about the

material, both rotating and oscillating measurements were performed. Following tests were performed on each ink-system:

- viscosity versus shear rate in a range from 0.01 to 10 s^{-1} (at the beginning and after all experiments to detect possible changes during measurements),
- rotational recovery tests with alternating (each 100 sec) high (5 s^{-1}) and low shear rates (0.01 s^{-1}),
- amplitude sweep (at 10 Hz from 0.01 to 10 % strain),
- frequency sweep (at a strain of 1 % from 0.1 to 1000 Hz),
- oscillating recovery tests with alternating (each 100 sec) high (100 %) and low strain (0.01 %).

Chapter 4.3: Results and discussion

One of the primary research questions of this chapter was if the nanoparticles will influence the printing properties of the ink when combined. To test this, MSN containing inks were prepared as described in Chapter 4.2 and rheological tests on them were performed. It is important to mention that the experiments were performed with inks that were not cross-linked and did not contain the photoinitiator to ensure that the samples do not change during testing. For characterization, MSN-inks were tested and compared to a non-MSN containing ink with the same composition. Both, oscillation and rotational experiments were performed to ensure complete characterization.

Based on an amplitude sweep shown in Figure 23A, the deflection for the frequency sweeps was chosen to be 1% because this value was in the linear viscoelastic region. The frequency sweeps shown in Figure 23B revealed that the material was viscoelastic. At low frequencies, the viscous properties dominated elastic properties of the material. After a cross-over point at about 1 s^{-1}, the elastic properties began to dominate. This revealed that at low deflections, no permanent changes

occur to the material, the inks showed a time dependent behavior. The differences between the MSN loaded inks and the particle-free reference were very small showing that the differently charged particles do not drastically change the viscoelastic material properties over the whole tested frequency range from 0.1 to 800 s^{-1} during cyclic loading. Further, the response of the material to alternating high deflection (100%) and low deflection (0.1%) was tested over a period of 18 cycles. Based on the experience with particle-free inks, the deflection of 100% is not in the linear viscoelastic region and thus in contrast to the low deflection, leads to changes in the material. Due to this, these tests reveal how the material recovers after being exposed to oscillating structural changes. As shown in Figure 23C the materials recovered quickly and the plateau levels for storage and loss modulus did not change even over a period of 18 cycles indicating self-healing properties of the material after cyclic loading.

In contrast to most oscillating rheological experiments, rotational experiments mainly induce structural changes and are therefore better suited to mimic the conditions the materials are subjected to when dispensed. Therefore, rotational experiments were used to characterize the materials when exposed to various rotational velocities and different shear rates. Measuring the viscosity over a shear rate interval from 0.01 to 5 s^{-1}, it was possible to show that the materials were shear thinning. As shown in Figure 24, MSN-containing inks lead to a small shift in the curve but did not alter the shear thinning properties of the materials. One possible explanation for this shift would be Coulomb interactions between the charged particles and the polymers in the ink. The main component influencing the viscoelastic properties in a non-cross-linked state is the hyaluronic acid. It contains COOH groups leading to a negative charge. Due to this, hyaluronic acid is charged the same way as the MSN-COOH and has the opposite charge as the MSN-NH_2 (zeta-potentials in PBS were measured in Ulm [153]). One would expect that likely charged components lead to repulsive forces and thus to a decreased viscosity whereas differently charged

components attract each other and thus increase the viscosity. Furthermore, the viscosity versus shear rate graph should show a sign of attractive interaction breaking, for example a change in the slope, in case of differently charged particles.

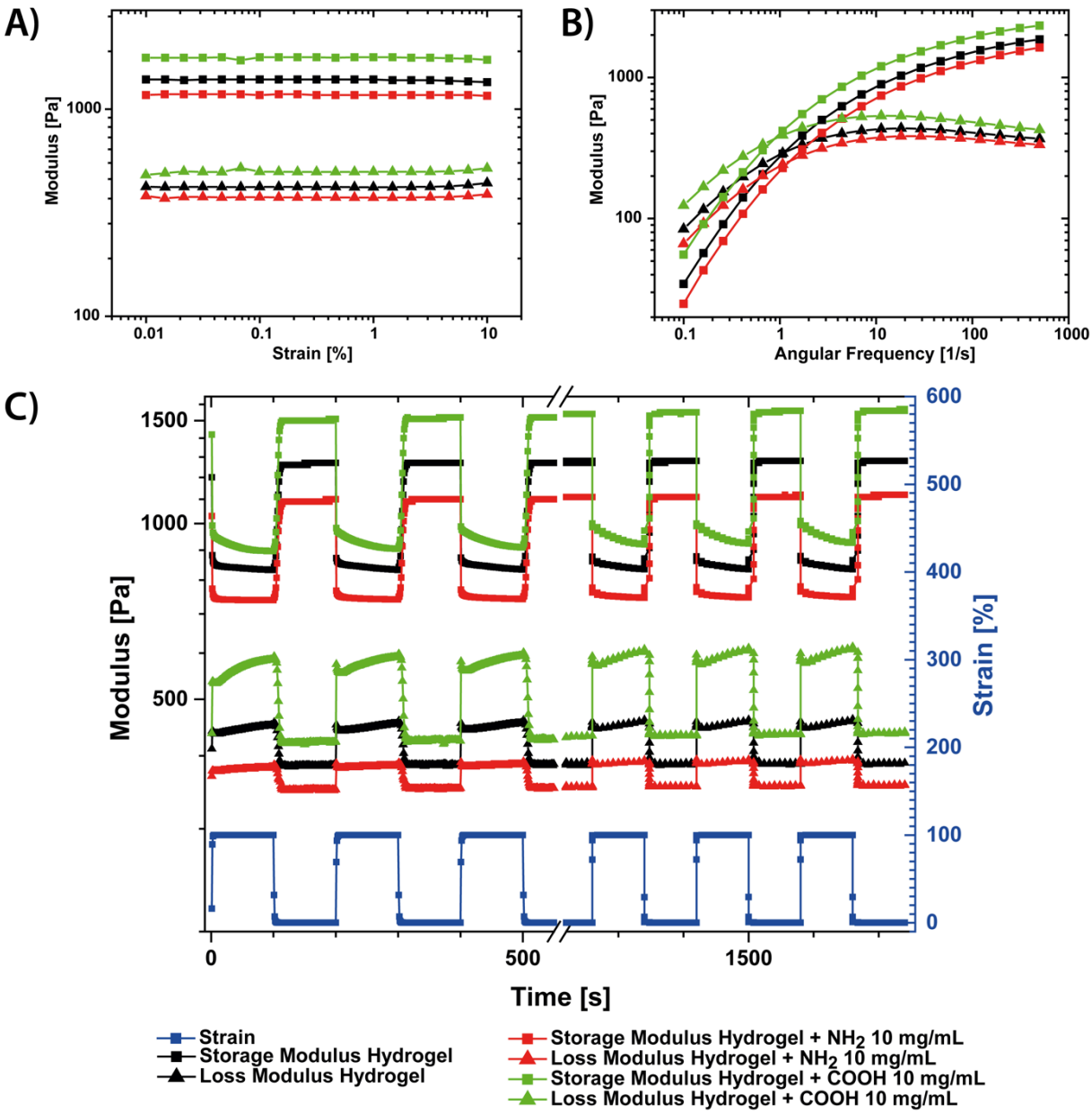

Figure 23: Oscillatory rheological analysis of 10 mg/mL MSN-inks compared to the no-loaded hydrogel component of the ink. A) shows an amplitude sweep, B) shows the data of the frequency sweep, and C) shows the modules for alternating low and high strains. The legend covers all graphs. (A) and B) Reprinted with permission from [153]. Copyright (2018) John Wiley and Sons.)

As shown in Figure 24, the particles did not change the shape of the curves compared to the non-MSN-ink and the shifts are opposite from what would have been expected

based on the charge considerations. This leads to the assumption that the silica nanoparticles do not influence shear thinning properties strongly. To support this conclusion, different concentrations of particles were also tested. Figure 24 only considers concentrations of 10 mg/mL MSN in the PBS stock solution. Figure 25A and Figure 25B further show concentrations of 0.1 and 1.0 mg/mL. Nether MSN-NH_2 nor MSN-COOH containing inks displayed a trend and in combination with the experiments of the 10 mg/mL, it can be concluded that the MSN did not change the shear thinning properties of the ink. To simulate the recovery of the materials after being dispensed, crucial for shape fidelity of printed constructs, experiments with alternating high (5 s^{-1}) and low (0.01 s^{-1}) shear rates were performed as shown in Figure 26. These experiments clearly demonstrate that the materials recovered quickly and for at least 3 cycles, the plateau values did not change. The differences between the MSN-containing and MSN-free inks were small and thus support the conclusion that the particles do not alter the rheological properties of the ink.

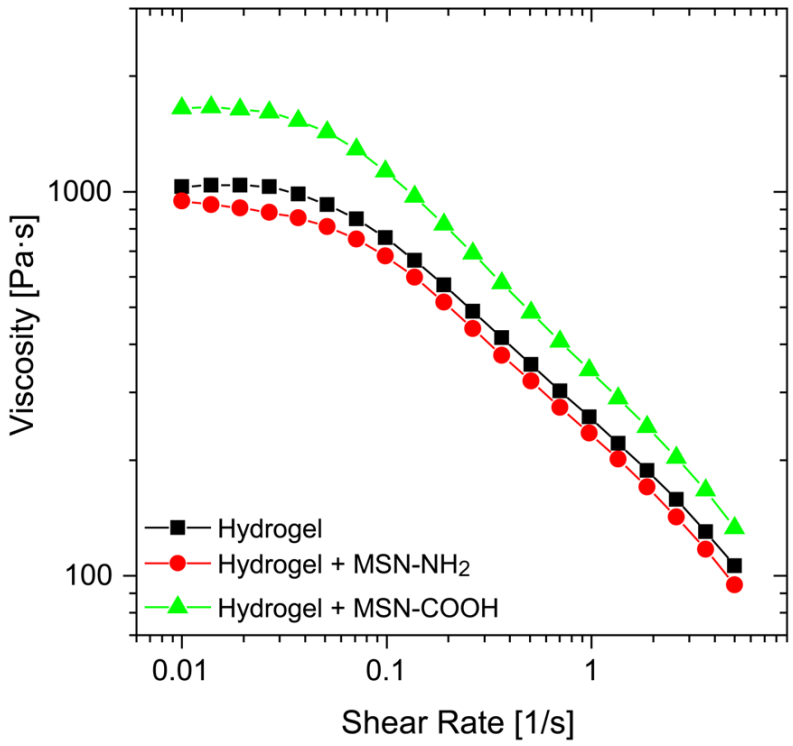

Figure 24: Viscosity over shear rate for MSN-containing and MSN-free inks. Reprinted with permission from [153]. Copyright (2018) John Wiley and Sons.

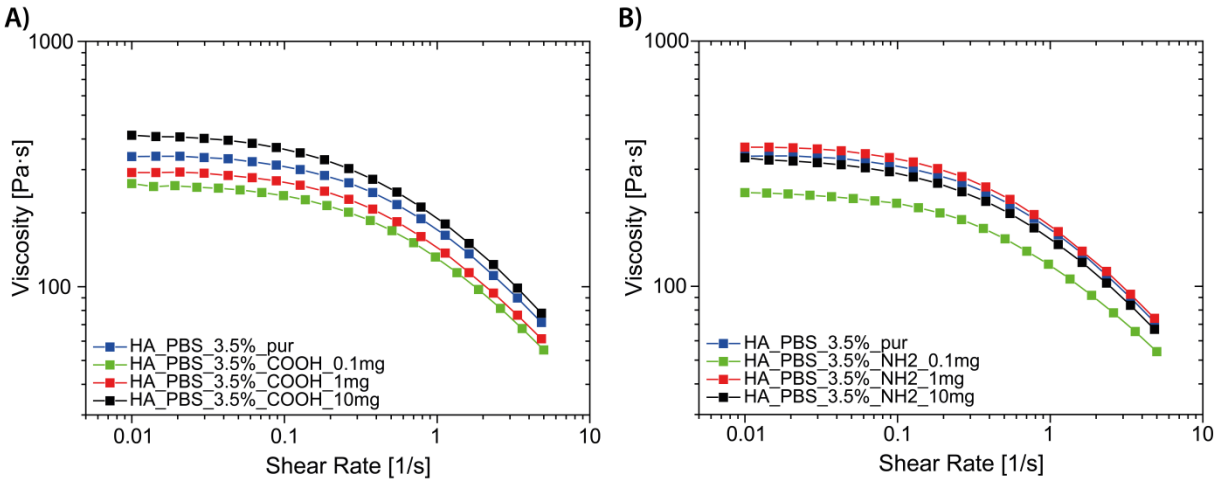

Figure 25: Viscosity over shear rate for MSN-inks and particle free inks. A) depicts viscosity measurements for different concentrations of MSN-COOH containing inks, B) shows MSN-NH_2 inks.

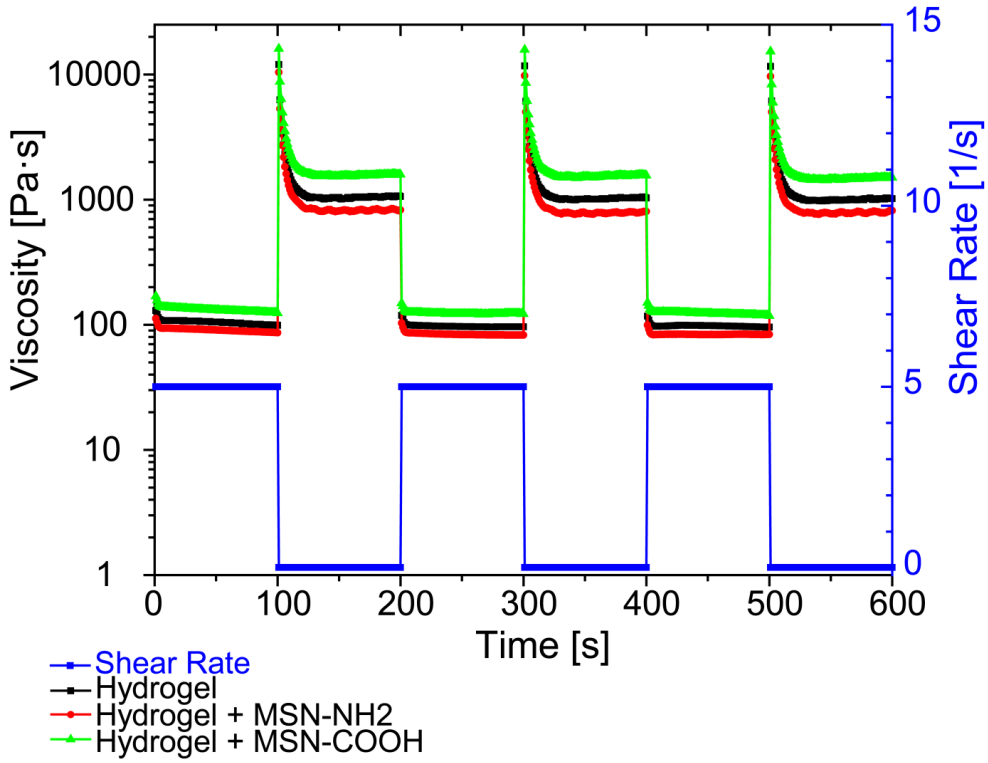

Figure 26: Viscosity at alternating high and low shear rates. Reprinted with permission from [153]. Copyright (2018) John Wiley and Sons.

Taking into account all rheological experiments, one would not expect that the nanoparticles change the printability of the material. Nevertheless, a critical consideration shall be given. A primary concern in terms of testing the MSN-inks can be related to the air bubbles which could not be eliminated completely. An example of the influence of air bubbles is given in Figure 27. It shows the viscosity over shear rate for hyaluronic acid only. One sample was centrifuged to eliminate air bubbles, the other one was tested as prepared with air bubbles. There was a shift but no change in the profile of the curve, indicating the error of the rheological experiments. Although larger air bubbles were destroyed using a spatula before testing, smaller air bubbles could not be eliminated because the centrifugal forces may have influenced the particle distribution within the ink and also influenced the following experiments. Therefore, this could not be performed during printing and it was decided to accept this drawback and the discussion was made in a very qualitative way. Intentionally, no values were named and also quantitative comparison between the inks was waived. A second critical concern is based on literature reviews as indicated by Jungst *et al.*[39] Because there is no accordance for testing printable materials it is difficult to compare rheological results between the different researchers and even more difficult to decide if a material is printable based on rheological data only. Nevertheless, rheological testing is important and the experiments and conclusions strongly relevant for the characterization of the material.

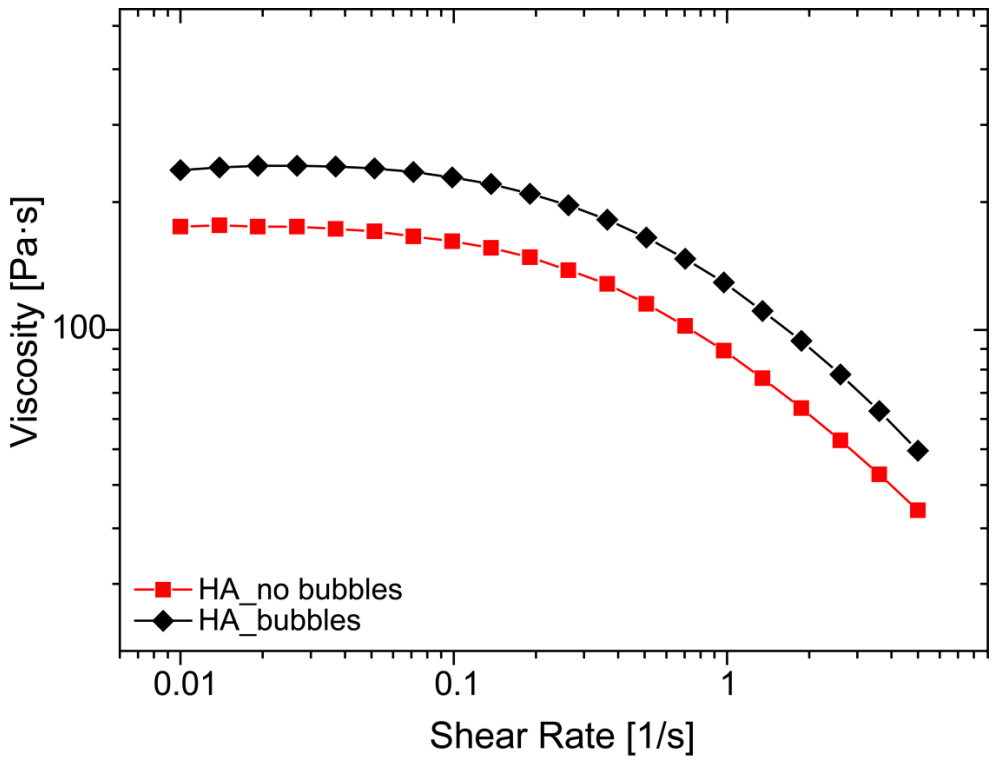

Figure 27: Air bubbles influencing rheological measurements. Viscosity over shear rate for centrifuged and non-centrifuged pure hyaluronic acid (HA).

By printing the material, it was proved that the differences seen in rheological pre-testing did not alter the print properties. Both inks could be processed using the same parameters and also the shape fidelity was not influenced by the MSN. Furthermore, cross-linking via UV light preserved the construct architecture over at least 6 weeks in PBS without excessive swelling or shrinking. It was possible to print constructs as big as 12x12x3 mm^3, 16 layers in total, with a strand-center-to-strand-center distance of 3 mm as shown in Figure 28A. Using a 0.30 mm inner diameter nozzle, it was possible to print strands with a diameter of 627±31 µm, as analyzed based on stereomicroscopic images as shown in Figure 28B. Further, inks containing labeled particles were printed and the constructs were imaged with a confocal microscope. A 3D reconstruction of a section from a printed two-component construct is shown in Figure 29. MSN-NH_2-inks are shown in red and MSN-COOH-inks in green. The figure clearly demonstrates the high print fidelity and the ability to print two-component structures with a precise and predesigned localization of ink/particle types. Nevertheless, this image also reveals one of the limitations that need to be

addressed in future experiments. The dark spots visible within the printed strands correspond to air bubbles within the ink. They were small enough to prevent strand break-up but could limit the ability to print smaller strand diameters and thus limit the achievable resolution. The standard procedure to eliminate air bubbles, centrifugation of the reservoirs before printing, could not be performed because of a possible segregation of particles. In future, other methods will need to be examined in case printing resolution has to be increased.

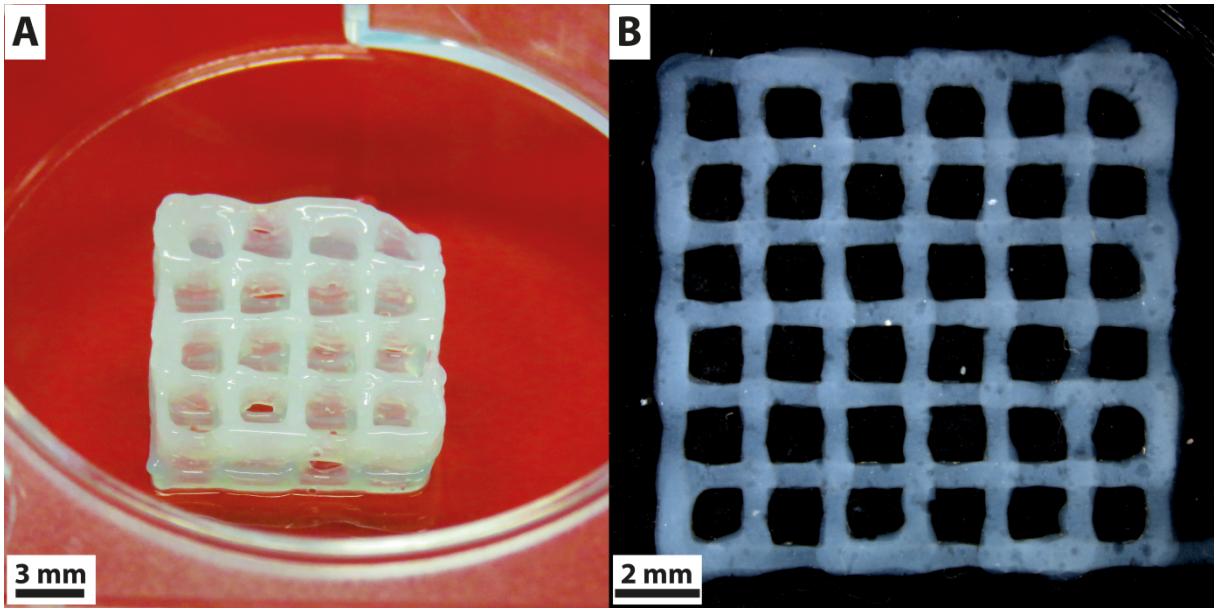

Figure 28: Printed constructs A) shows a construct with an overall size of 12x12x3 mm^3 (16 layers). B) shows a stereomicroscopic image of a top view on a 4-layer construct with a footprint of 12x12 mm^2 and a strand-center-to-strand-center distance of 2.0 mm. Reprinted with permission from [153]. Copyright (2017) John Wiley and Sons.

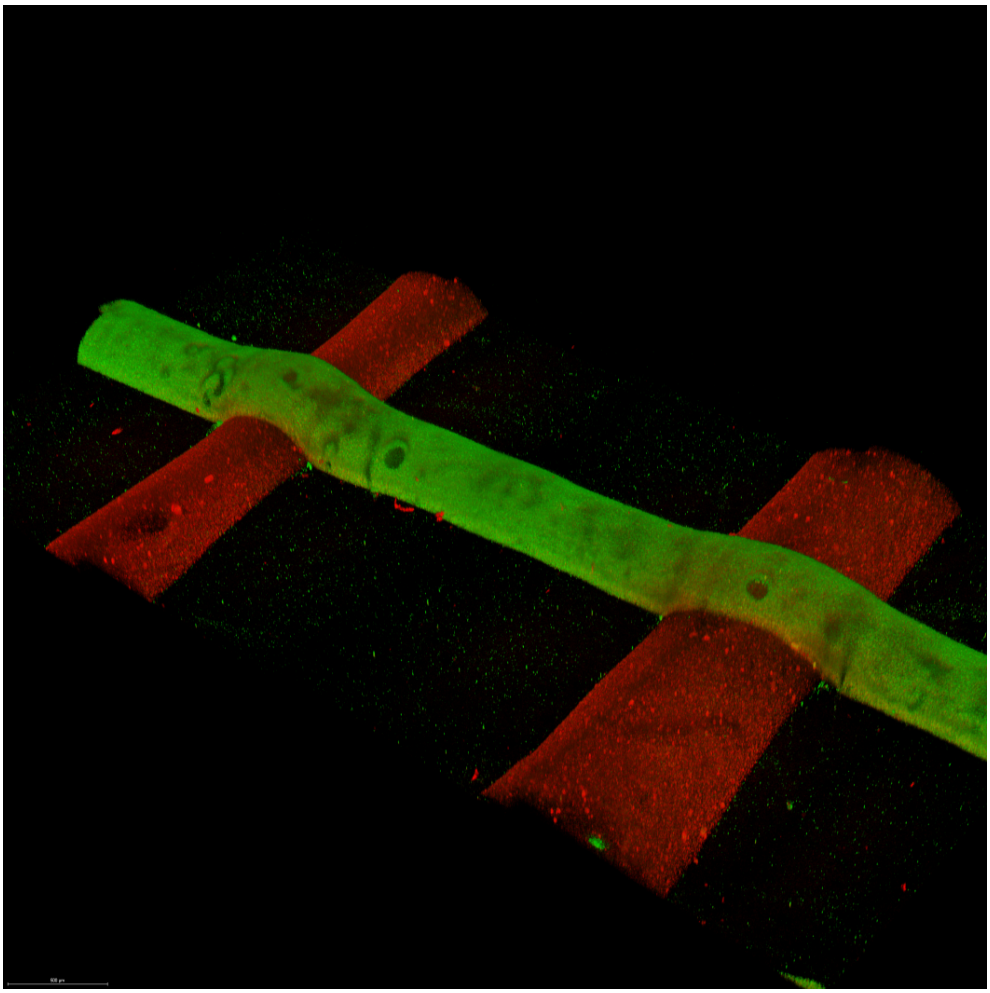

Figure 29: Two-component construct. MSN-NH_2 were labeled in red and MSN-COOH in green.

After the MSN-inks proved to be printable, the question whether the particle distribution within the constructs will be homogeneous or if they will be agglomerated and unevenly distributed arose. To reveal this an examination was performed by using high-resolution confocal microscopic images of stained particles in combination with a tile function combining the single images to a large overview without limiting the resolution. As shown in Figure 30, for a mixed sample containing both particles species, a homogeneous particle distribution all over the cross-section of a printed construct was shown. There was no sign of higher particle densities at the exterior, in the center of the printed strands or around air bubbles. Nevertheless, under further examination areas with bigger agglomerates and areas with smaller agglomerates were observed. The distribution of these areas was random and thus the particle

distribution could be considered homogeneous. Further, this conclusion could be supported by observations during microscopy (not shown here) and by the 3D reconstructs shown in this chapter. It revealed that the preparation was sufficient and that no segregation of particles occurred. Based on the results, one would not expect differences between printed samples ensuring comparability and reproducibility regarding particle release.

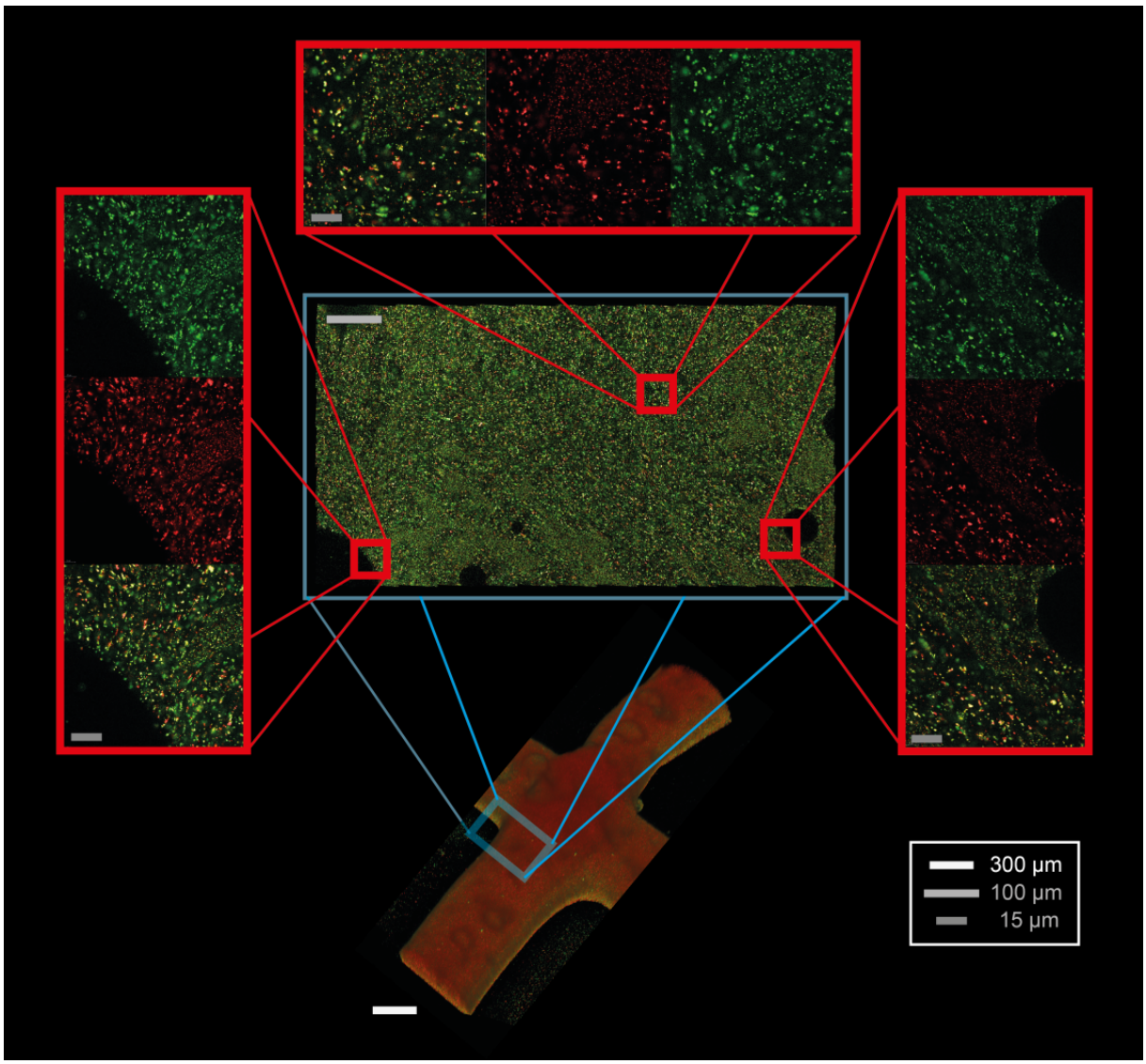

Figure 30: Confocal image of a section through a printed construct. The magnifications show the labeled COOH-functionalized particles (green) the labeled NH_2-functionalized particles (red) and both signals in one image. Reprinted with permission from [153]. Copyright (2018) John Wiley and Sons.

Particle release was investigated by printing two component structures in different geometries. One geometry was a cross-over of MSN-COOH and MSN-NH_2

containing inks and the other one was two parallel strands that did not touch each other. The experiment is illustrated in Figure 31. The constructs were stored in PBS and measured after time periods of 1 day, 3 weeks, 5 weeks, and 6 weeks. Depicted are only time points of 1 day after printing and 6 weeks after printing. For each of the time points, the PBS was exchanged. During printing, each strand type only contained one particle type but over time a migration of MSN was observed. The images correlated to overview 1 show the cross section and the upper pictures in Figure 31 are divided into the different signals. As shown after 1 day, the ATTO488 labeled MSN-COOH could just be found in the strand that was printed with this particle species only. In contrast, the ATTO647N labeled MSN-NH_2 could also be found within the strand initially containing the opposite species. After 6 weeks, the migration of the MSN-NH_2 particles was slightly stronger but more interestingly there were still no or only little MSN-COOH visible in the MSN-NH_2 strand. Overview 2 in Figure 31 shows the same experiments but for the parallel geometry. The left strand initially only contained ATTO647N labeled MSN-NH_2 the right strand ATTO488 labeled MSN-COOH. At day 1 after printing, neither of the strands showed the opposite particle type. 6 weeks after printing, some COOH particles could be found in the NH_2. After this time period, the signal of the MSN-NH_2 in the MSN-COOH was stronger than the other way. These experiments clearly revealed that the geometry had a huge impact on the particle release and that the release kinetics for both particle types were different and geometry dependent. Due to the charges of the particles in combination with the hydrogel being mainly negatively charged, because of the high hyaluronic acid content, this behavior could be explained by electrostatic forces between particles and hydrogel. The COOH–functionalized particles in combination with the likely charged hyaluronic acid will reveal a stronger negative potential than the strand containing NH_2 functionalized particles and hyaluronic acid. Due to this, the positively charged MSN-NH_2 will be attracted by the COOH containing ink and thus migrate into these strands. The smaller the distance, as in the cross-over constructs, the higher

the attractive force and the faster the migration as revealed by the experiments just discussed. In contrast to the MSN-NH_2, the MSN-COOH will rather be released into the PBS than into the printed strand containing MSN-NH_2 because the likely charged hyaluronic acid still present in the printed strand must still be less attractive than the PBS.

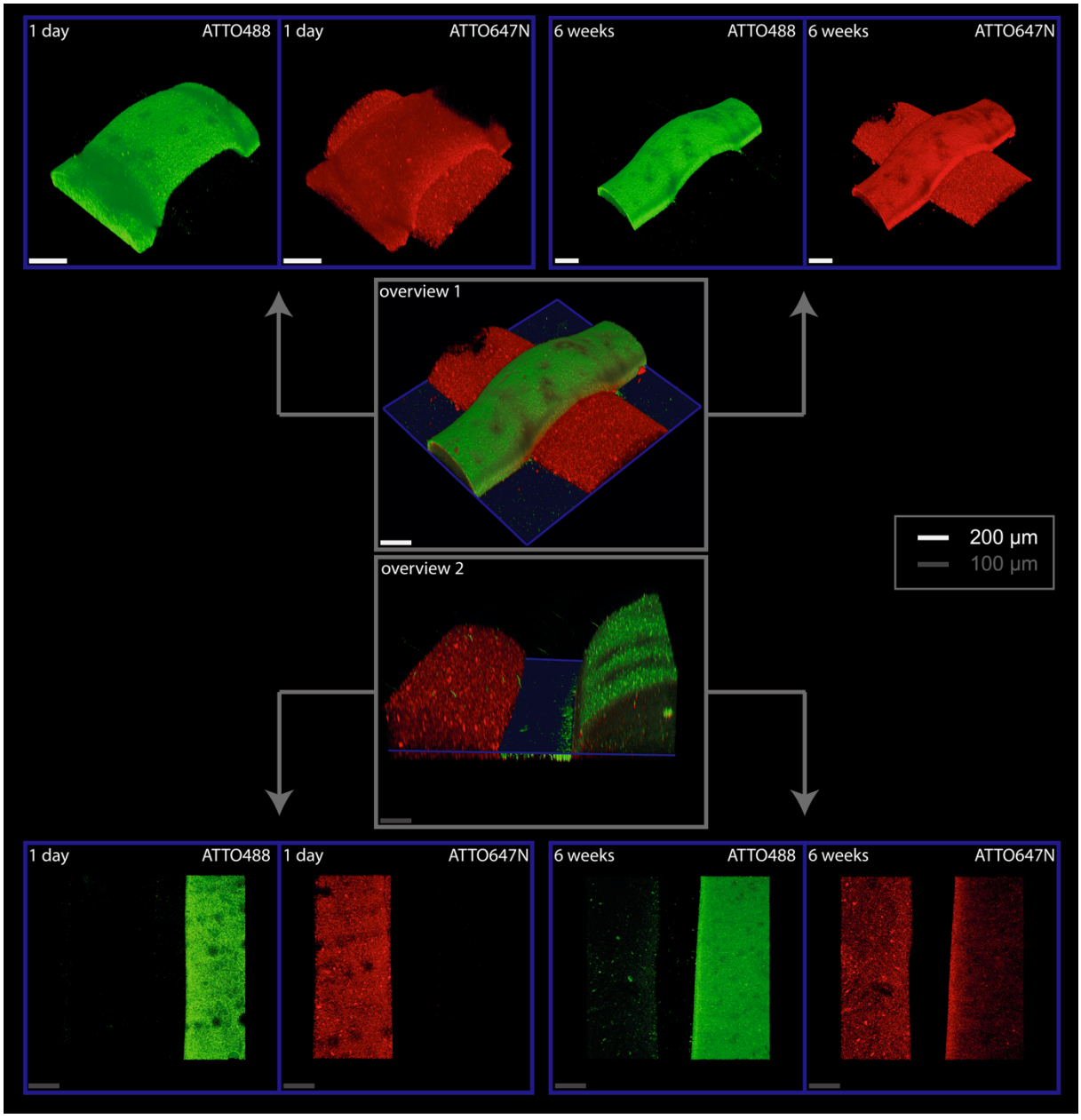

Figure 31: Particle migration into hydrogels with and without direct contact. Images correlated to overview 1 show a cross made of two strands each containing only one particle species directly after printing. 1 day after printing, the amino-functionalized particles migrated into the strand containing carboxy-functionalized particles whereas no COOH-functionalized particles could be found in the NH_2-functionalized particle containing strand. After 6 weeks,

the results were even clearer and only a few COOH functionalized particles could be found in the strand with the other particle type. The images below overview 2 show two parallel strands with no direct contact. Compared to the construct with direct contact 1 day after printing, there were no particles found in the stand with the other particles species. 6 weeks after printing, particles migrated into the strand that was not containing the other species whereas the signal of the ATTO647N label attached to the NH_2-functionalized particles was brighter in the carboxy-functionalized particle containing strand than vice versa. Reprinted with permission from [153]. Copyright (2018) John Wiley and Sons.

Chapter 4.4: Conclusion

This chapter describes an analysis where two established systems, MSN and bioinks based on polyglycidols and hyaluronic acid, were combined to gain temporal and spatial control of particles release. Using thorough rheological testing with oscillating and rotating setups it was possible to show that the particles did not influence the rheological properties of the inks. Neither the shear thinning properties of the printable ink nor the recovery were negatively influenced. This was an interesting observation because the particles were fluorescently stained and modified with COOH and NH_2 to change their charge. Taking into account that the ink itself is, due to the hyaluronic acid that also dominates its rheological properties, negatively charged, one could expect charge-based alterations. Furthermore, the ink printability was not changed by the particles and it was possible to print constructs as big as 12x12x3 mm^3 (16 layers) without structural collapse using extrusion based bioprinting. The printer setup enabled the fabrication of two-component constructs. This way two different geometries could be printed using ink loaded with MSN-COOH and MSN-NH_2: One with direct contact between the different materials and one without direct contact. Tracking the printed geometries while being stored in PBS, showed that in case of direct contact the MSN-NH_2 were able to quickly (< 1d) migrate into the strand that initially only contained MSN-COOH. In contrast, in case of a geometry without direct contact even after 6 weeks only few MSN-NH_2 could be found in the strands which previously only contained MSN-COOH. For both geometries even over a timeframe of 6 weeks no MSN-COOH could be found in the MSN-NH_2 containing strands. These observations showed that charge had an effect on particle release and

migration because positively charged MSN-NH_2 were attracted by the high negative net charge generated by MSN-COOH and MSN-NH_2 and, in case of direct contact, migrated into those strands. In case of no direct contact the potential of the surrounding liquid was more attractive than the MSN-NH_2 containing strands and thus the MSN-COOH were released into the solution. This experimental setup proved that the geometry had an impact on particle migration and release.

Chapter 5

Biofabrication of cell-loaded 3D spider silk constructs

This chapter was published as original research article:

Schacht, K.*; Jungst, T.*; Schweinlin, M.; Ewald, A.; Groll, J.[#]; Scheibel, T.[#] Biofabrication of cell-loaded 3D spider silk constructs. *Angewandte Chemie International Edition* **2015,** *54* (9), 2816-2820.

* Kristin Schacht and Tomasz Jüngst contributed equally.

[#] Thomas Scheibel and Jürgen Groll share corresponding authorship.

The article was re-written and supplemented with additional experiments to represents the work that was performed by Tomasz Jüngst.

The author contributions to the original research article are as follows:

Contributor	Contribution
Tomasz Jüngst	Designed and performed printing experiments; designed cell adhesion experiments on printed constructs and cell encapsulation studies; co-wrote and revised manuscript content
Kristin Schacht	Prepared hydrogel inks; designed and performed cell adhesion experiments on printed and un-printed spider silk hydrogels; designed and performed diffusion tests and chemical/physical analysis of the recombinant proteins; co-wrote and revised manuscript content
Matthias Schweinlin	Imaged cells using confocal microscopy; designed and planned sample preparation for confocal microscopy; performed cell-viability analysis; provided feedback on the manuscript
Andrea Ewald	Designed cell adhesion and cell-viability experiments as well as cell encapsulation studies
Jürgen Groll	Conceived and designed experiments; revised and provided feedback on the manuscript
Thomas Scheibel	Conceived and designed experiments; revised and provided feedback on the manuscript

Chapter 5.1: Introduction

This chapter describes the aim to address one of the main bottlenecks of biofabrication: the need for novel materials. Although this bottleneck was highlighted within recent reviews[39,117], most research groups continue working with, and further improve, established materials such as alginate[154] and gelatin-based systems.[51] The traditional approach to biofabrication (see Figure 32) involves using either materials to obtain structures that elicit biological response or materials maintaining certain shape fidelity. Therefore, it is crucial to shift this window of biofabrication towards novel material systems employing both a good shape fidelity and a good biological response by introducing novel strategies.[117] A promising material class to fulfill this transformation was developed by the group of Prof. Scheibel in Bayreuth, recombinant spider silk proteins. They proved to be non-immunogenic, cytocompatible, and are physically cross-linked.[155]

As demonstrated in this chapter, the material was dispensable without the need for additional thickeners or post-process cross-linking and it was possible to print cell-containing structures revealing good shape fidelity, making a first step towards the shift of the window of biofabrication. The following chapter focuses on testing and improving the printability of a new class of bioinks for robotic dispensing. Primarily the printer and the codes used to generate constructs and assure good shape fidelity at minimal material loss had to be set up and adjusted. Furthermore, the cell-material interaction was tested with human fibroblasts by seeding them onto printed constructs. The constructs were generated using recombinant spider silk hydrogels with and without a modification by RGD sequences. By printing inks containing viable cells, also the "prime discipline" of biofabrication was challenged.

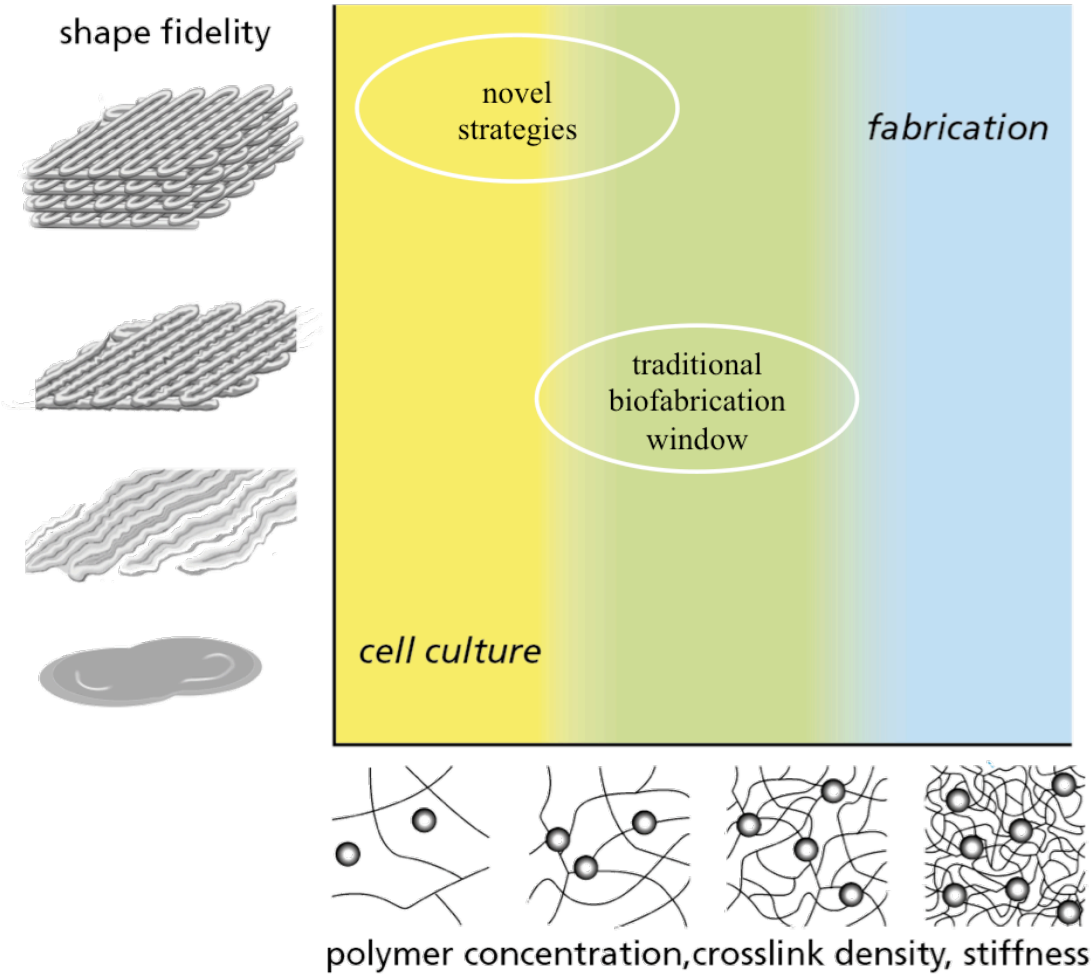

Figure 32: The window of biofabrication. Materials currently applied for biofabrication match the traditional biofabrication window and represent a compromise between properties optimized towards fabrication and thus high print fidelity and properties optimized for cell culture and thus biological response. This window needs to be shifted towards novel strategies implying shape fidelity and excellent biological response by developing new material systems. Reprinted with permission from [117]. Copyright (2018) John Wiley and Sons.

Chapter 5.2: Materials and methods

The recombinant spider silk protein hydrogels were prepared and pretested by the group of Prof. Scheibel.[155] 3D printing was performed using robotic dispensing and two different types of scaffolds, cell-free and cell-loaded, were generated with a bioprinter (3DDiscovery, regenHU). This device allows dispensing of hydrogels through two different approaches described in the following: the first print head (DD-

135N "syringe dispenser") operates based on a time-pressure principle. The valve controlling dispensing sits between the inlet of the pressurized air and the piston of the syringe (3cc syringe, Nordson EFD) that presses the materials towards the nozzle (interchangeable standard luer-lock precision needle, Nordson EFD). In the second approach, another print head (CF-300N/H "cell-friendly" print head) contains a special electromagnetic valve located just in front of the needle. A constant pressure on the piston of the syringe (3cc syringe, Nordson EFD) allows very precise dispensing compared to the other print head just described, with highly-limited delay between material flow and the according command sent to the printer as well as between the according command and the stop of dispensing. Working in a sterile environment is facilitated by the printer being located in a laminar-flow cabinet and by the possibility to autoclave all components in direct contact with the bioink. Further, dispensing was performed at room temperature. After fabrication, the constructs were imaged with a stereomicroscope (SteREO Discovery.V20, Carl Zeiss) to analyze the printing fidelity.

Cell-material interactions between fibroblasts and cell-free constructs were evaluated by seeding cells onto constructs composed of two layers of ink. The human fibroblasts (patient dermal fibroblast cells, G12660) were cultivated on the scaffolds using densities of 75 000 cells cm^{-2}. Further details for cell culture can be found in the literature.[155] To create cell-laden bioinks, the fibroblasts were added to highly concentrated (3 % w/v) spider silk solutions at densities of 1.2 million cells mL^{-1} and were gelled overnight at 37 °C and 95% relative humidity. Analysis of cell viability after seeding and printing was performed using a live/dead assay. The cells were stained using calcein A/M and Ethidium Homodimer I (both Invitrogen).[155] The green fluorescence of the viable cells and the red fluorescence of the dead cells were quantified upon analysis of the images taken with a fluorescence microscope (Carl Zeiss Axio Observer.Z1) and a confocal scanning microscope (Leica TCS SP8 STED) by Matthias Schweinlin.

Chapter 5.3: Results and discussion

The recombinant silk (eADF4(C16)) chosen for printing mimics the core sequence of the dragline silk of a European garden spider (*A. diadematus*). To be able to influence cell material interactions, also a version of recombinant silk hydrogel containing a RGD sequence covalently coupled to the protein (eADF4(C16)-RGD) was used.[155]

It could be shown that the material was printable independent from which print head was used. During pretesting, it was found that the "cell-friendly" print head equipped with the electromagnetic valve generated constructs with a higher printing fidelity because it was possible to generate strands with more consistent diameters. In robotic dispensing, discrepancies in the diameter of the dispensed filament can lead to disrupted strands. Due to the layer-by-layer assembly, an error within one layer will influence the quality of the following layers. Only if materials can span over gaps, which, from a printing point of view, is one of the most difficult features an ink can perform,[39] this phenomenon can be overcome. As displayed in Figure 33, the spider silk ink did not span between the strands but bigger errors could be bridged indicating the good printing properties of the ink.

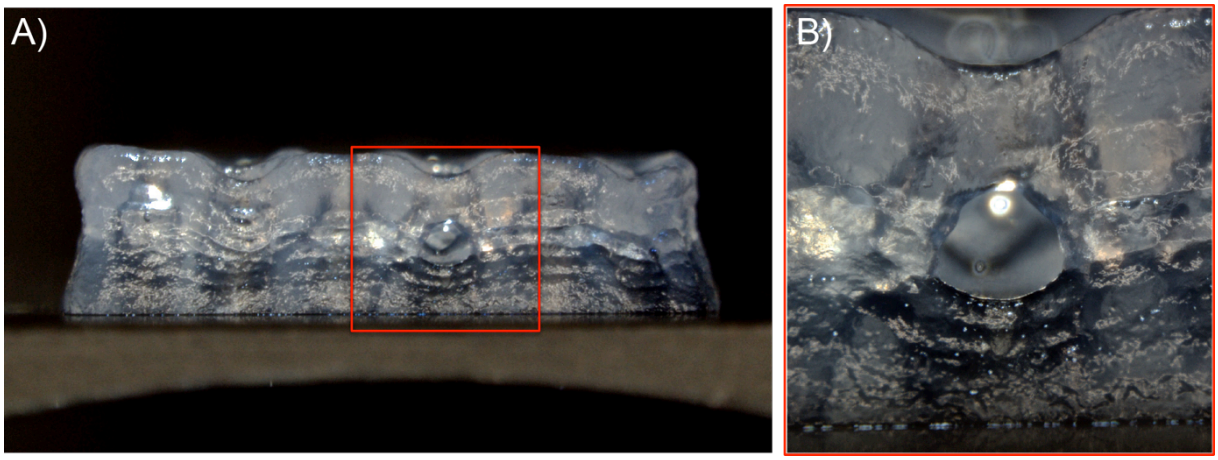

Figure 33: Filament disruption reducing print quality. A) shows a side view on a printed construct composed of 16 layers. Due to a disrupted strand the following layers were influenced resulting in a hole in the construct. B) shows a magnification of the hole marked with the red box in A).

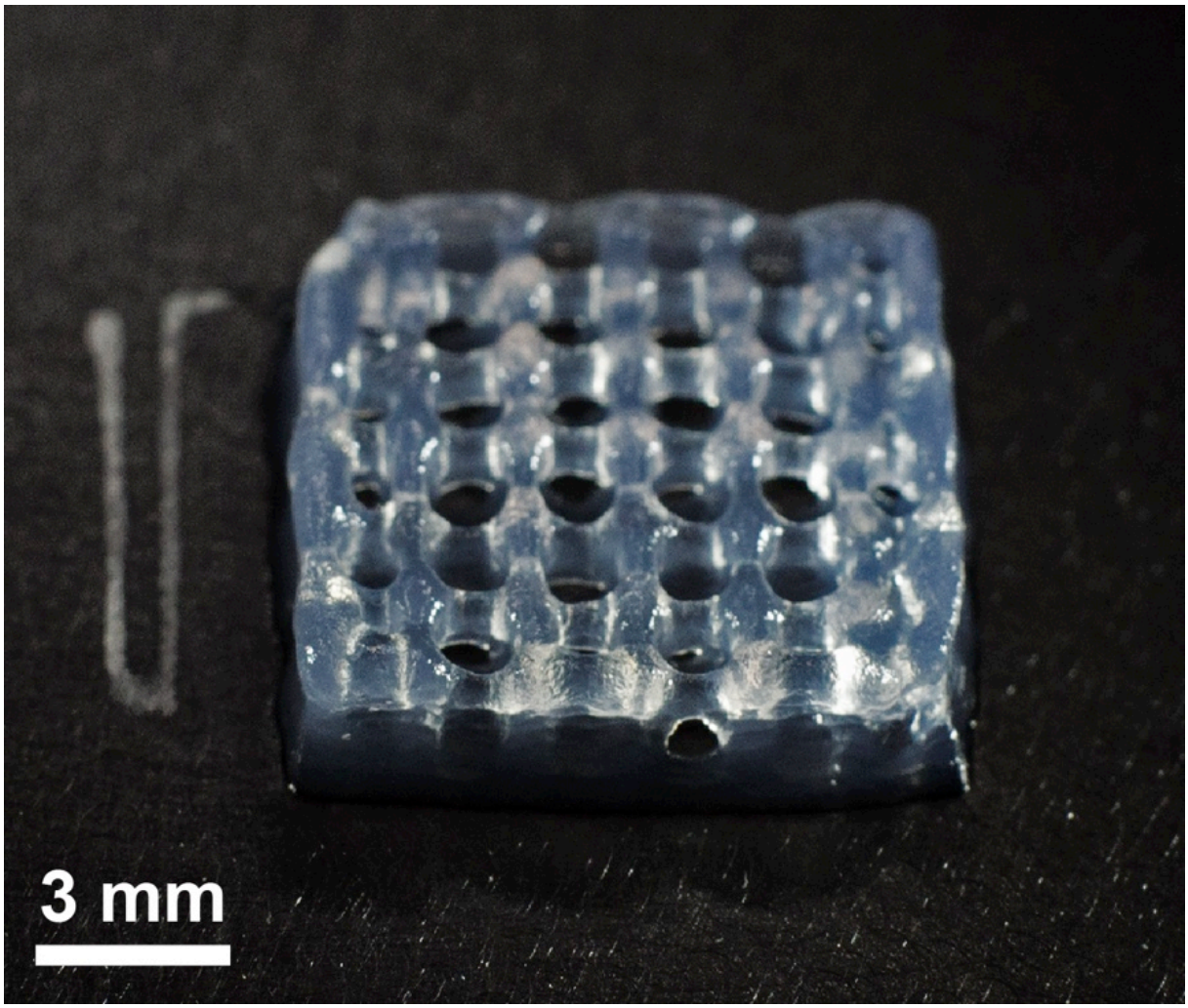

Figure 34: Printed construct. 16 layers were stacked on top of each other to generate this construct. Reprinted with permission from [155]. Copyright (2018) John Wiley and Sons.

Due to the viscoelastic properties enabling the ink to overcome bigger voids, it was possible to generate constructs as large as 12x12x3 mm (length x width x height) with a strand-center-to-strand-center distance of 2 mm, composed of 16 layers, not showing collapse of the pores generated in the z-direction (see Figure 34). The diameter of the nozzle used to dispense the ink was 0.3 mm and the pressure needed was 1.0 bar. Applying these parameters combined with a valve opening time of 700 µs resulted in filament diameters of 626 ± 8 µm. Based on the good printing fidelity of the generated constructs, it was decided to test the materials for printing anatomically-relevant geometries. A model mimicking a human ear was designed and printed as shown in Figure 35. Figure 35A shows the design comprised of three levels gaining height with the blue color getting darker. It was possible to closely reproduce

the model with a size of 42x23x4 mm. Furthermore, the porosity and the surface smoothness of the construct was influenced by changing the pressure during printing (increased by 0.3 bar). Interestingly, the material did not need post-process treatment or thickeners to be printable. As described in the introduction, established materials such as gelMA or alginate need UV irradiation, temperature changes, or ionic post process cross-linking to ensure the shape fidelity after dispensing and over longer periods of cell culture. In contrast to this, the recombinant spider silk inks developed and used in this collaboration were cross-linked by physical interactions (mainly β-sheet structures and hydrogen bonds) simplifying printing and handling of the constructs.[155]

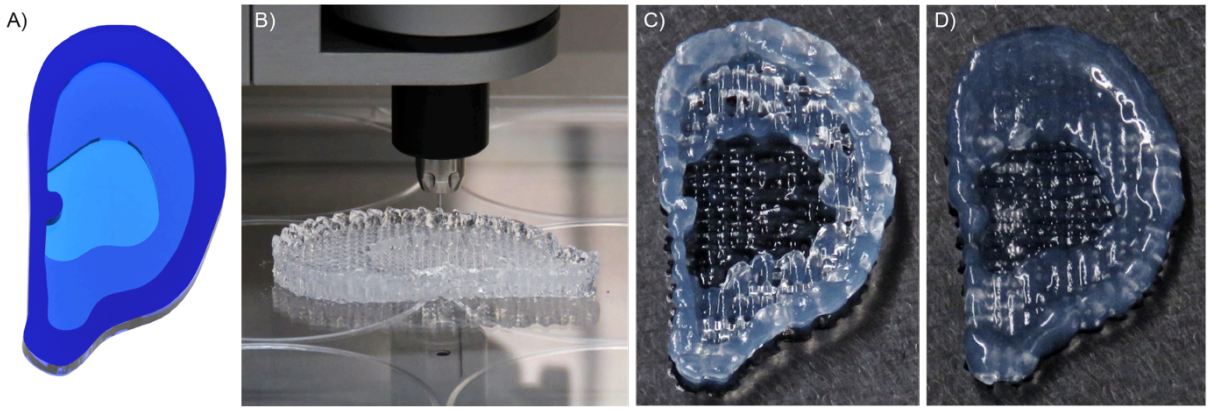

Figure 35: Printing of a construct mimicking a human ear. Based on a computer aided design file (A) a construct with a size of 42x23x4 mm was printed (B). By changing the pressure, the surface properties could be varied. At lower pressures (C) the filaments kept their shape, at higher pressures (D) a smoother surface and a construct with less porosity could be generated.

Based on these pretests, constructs were printed using the parameters mentioned above and cells were cultured on top of them. It was possible to print the constructs directly into 6-well-plates helping to ensure sterility as well as simplifying handling and cell culture. In contrast to the cell culture pretests,[155] where murine cell types were seeded onto disk like samples, here human derived fibroblast cells were cultured onto structured constructs to test cell–material interactions and the influence of the addition of RGD sequences on cellular behavior. As shown by live/dead staining after 24h of culture in Figure 36 the adhesion of fibroblasts was better on eADF4(C16)-RGD (Figure 36B) constructs than on those from eADF4(C16) (Figure 36A). To ensure

that the imaged cells were on the constructs and not underneath, further images with the focal plane being at the bottom of the well plate (Figure 36A´ and B´) were implemented. The live/dead assay also stained the construct itself in red. To prove that dead cells were still visible and thus it was possible to analyze them due to their brighter appearance dead cells were marked in Figure 36B and B´ with arrows indicating their position. To analyze if cells were able to infiltrate the constructs, 3D reconstructs of the samples were taken by confocal imaging. As shown in Figure 36C and C´ cells were not able to grow into the structures after 24h of cell culture.

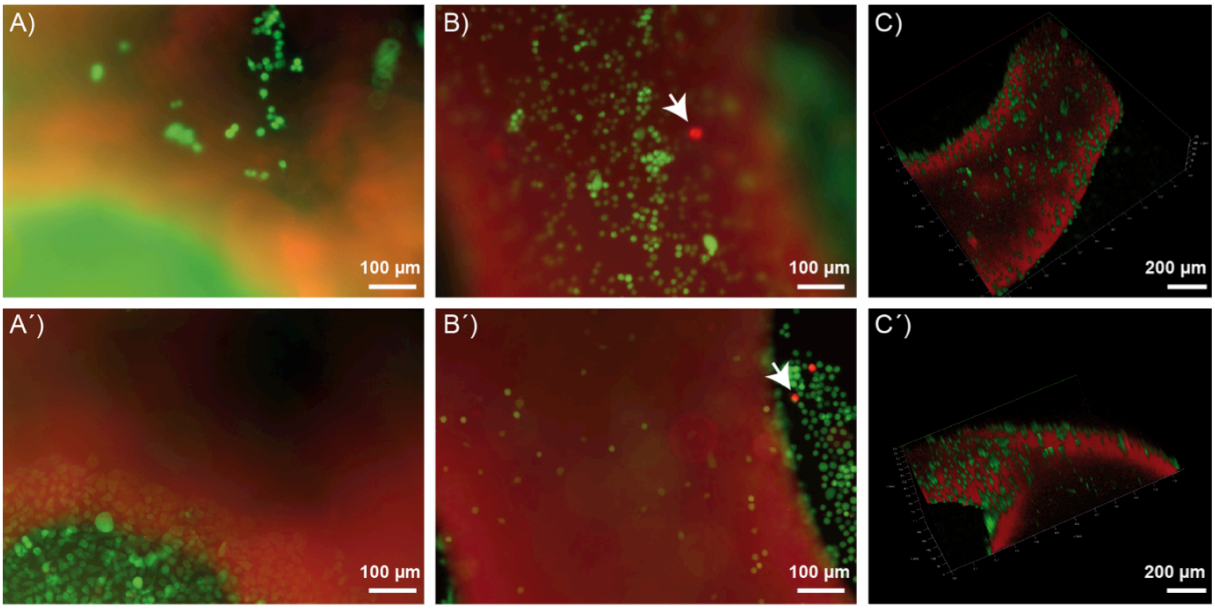

Figure 36: Human fibroblasts cultured on printed spider silk constructs. A and A´) show fluorescent microscopy images of a seeded eADF4(C16) construct after 24h of culture (A) focus on construct, A´) focus on well plate). B and B´) show fluorescent microscopy images of a seeded eADF4(C16) construct after 24h of culture (B) focus on construct, B´) focus on well plate). C and C´) show confocal 3D reconstruction of a printed eADF4(C16)-RGD sample after 48h of cell culture from different perspectives. Reprinted with permission from [155]. Copyright (2018) John Wiley and Sons.

To further analyze the suitability of the recombinant spider silk hydrogels as a novel ink system for biofabrication, cells were encapsulated at densities of 1.2 million cells mL^{-1} within the constructs and were printed. Here it is worth mentioning that this is the most difficult aspect in biofabrication and printing viable, encapsulated cells is one of the most challenging approaches in the field of biofabrication. It was noticed that the addition of cells did not influence the printing

fidelity of the bioink and the printing parameters using the "cell-friendly" print head only had to be varied slightly to receive comparable prints: The pressure had to be raised from 1.0 to 1.1 bar and the valve opening time had to be increased from 700 to 900 µs. Analysis of the cell viability was performed using live/dead assays after 24h, 48h, 72h, and 7d of culture. Figure 37A and B show florescent microscope images of live/dead stainings after 48h of culture. The construct depicted in Figure 37A shows cells within a printed construct whereas Figure 37B was taken with a not-printed reference. It was found that the cells were distributed homogeneously within the printed constructs. Furthermore, a detailed analysis revealed that only 70.1 ± 7.6 %[155] of the cells were viable 48h after printing. Compared to established ink systems such as alginate (about 90 % viability[154]) and gelMA (approximately 98 % viability[156]), these values seem to be significantly smaller. Nevertheless, taking into account the high printing fidelity and the fact that, when compared to the not-printed reference, printing itself did not significantly alter cell viability, the 97% relative survival of the cells is a very good starting point for further development of recombinant spider silk bioinks.[155] As shown in Figure 37A´ and B´, cells remained viable in the printed construct (Figure 37A´) as well as in the non-printed reference (Figure 37B´) over a culture period of at least 7d. To get a better feeling for the morphology of the cells embedded in the gels for 48h, confocal images were taken. Figure 37C and C´ show two of these confocal images (only one plane, not a 3D reconstruction) from a printed eADF4(C16) construct at different magnifications. It further displays the homogeneous distribution of the cells within the construct and especially at the higher magnification (Figure 37C´) were the spherical shape of the cells is clearly visible. This may be an indication for a dense polymer network where the cells cannot penetrate or alter.

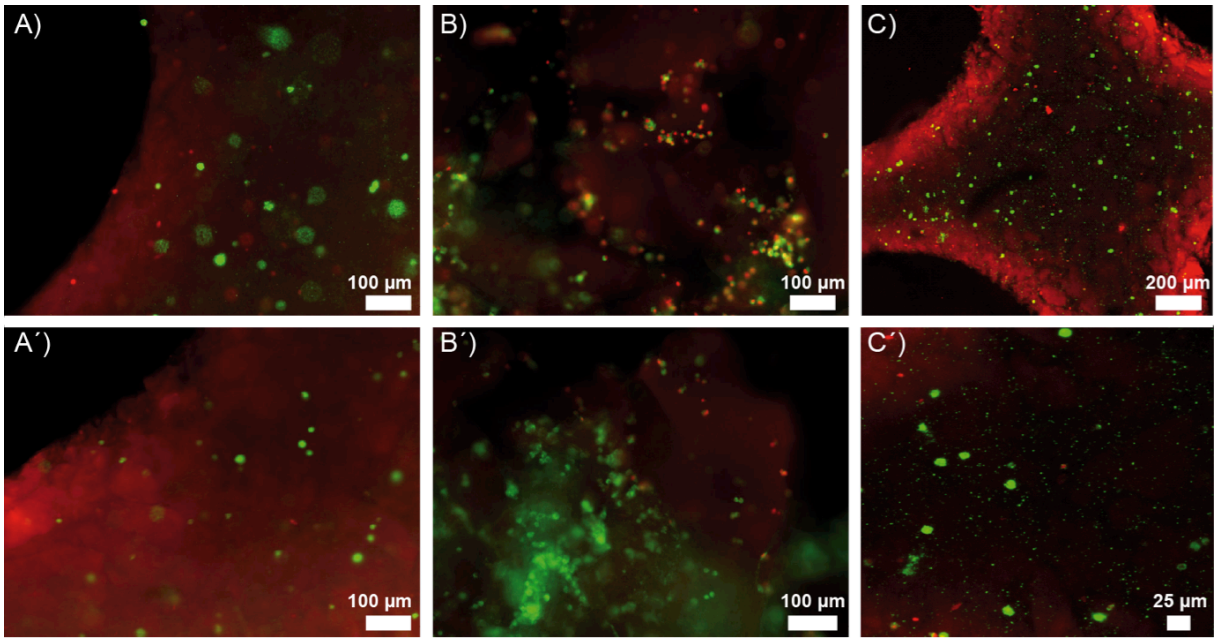

Figure 37: Human fibroblasts encapsulated in recombinant spider silk proteins. The figure shows fluorescent microscopy images of a printed eADF4(C16) construct after 48h (A) and 7d (A´) of culture. B and B´) show fluorescent microscopy images of a non-printed eADF4(C16) reference after 48h (B) and 7d (B´) of culture. C and C´) show confocal images of a printed eADF4(C16) sample after 48h of cell culture at different magnifications. Reprinted with permission from [155]. Copyright (2018) John Wiley and Sons.

Chapter 5.4: *Conclusion*

Within this chapter, one of the known bottlenecks in biofabrication, the limited amount of suitable materials, was addressed. Hydrogels from recombinant spider silk proteins could be printed. Although the quality of the prints was better using the "cell-friendly" print head equipped with an electromagnetic valve, the inks could also be processed with the "syringe dispenser" operating based on a time-pressure principle. Using needles with inner diameters of 0.3 mm and filament diameters of 626 ± 8 µm, the material could be dispensed. Furthermore, it was possible to generate constructs with different shapes in a layer-by-layer fashion. To test the influence of a RGD sequence coupled to the recombinant proteins on the behavior of human fibroblasts, non cell-loaded constructs were printed and cells were seeded on top of them. Cell attachment on structured, printed constructs was improved by the RGD sequence. Further, the potential of the material as novel bioink for biofabrication was tested by

printing recombinant spider silk protein hydrogels containing cells (1.2 million cells mL^{-1}). Although the cell survival of 70.1 ± 7.6 % was not as high as within established ink systems, the material also mastered this "prime discipline" of biofabrication. Based on these results, further experiments will be performed on the system to improve cell viability and to even further improve the printing fidelity. A crucial step will be the analysis of the impact of printing on the cells as analyzing the viability of cells using live/dead assays does not fully prove that cells can survive the process of printing without being altered. It will be important to test if they maintain normal function after fabrication by prolonged cell culture periods and in depth biological evaluations. Further, it will be important to test other cell types and match them to the applications envisioned for the final constructs.

Chapter 6

Summary / Zusammenfassung

Chapter 6.1: *Summary*

Chapter 6.2: *Zusammenfassung*

Chapter 6.1: Summary

Biofabrication is an advancing new research field that might, one day, lead to complex products like tissue replacements or tissue analogues for drug testing. Although great progress was made during the last years, there are still major hurdles like new types of materials and advanced processing techniques. The main **focus of this thesis** was to help overcoming this hurdles by challenging and improving existing fabrication processes like extrusion-based bioprinting but also by developing new techniques. Furthermore, this thesis assisted in designing and processing materials from novel building blocks like recombinant spider silk proteins or inks loaded with charged nanoparticles.

A novel 3D printing technique called Melt Electrospinning Writing (MEW) was used in **Chapter 3** to create tubular constructs from thin polymer fibers (roughly 12 µm in diameter) by collecting the fibers onto rotating and translating cylinders. The main focus was put on the influence of the collector diameter and its rotation and translation on the morphology of the constructs generated by this approach. In a first step, the collector was not moving and the pattern generated by these settings was analyzed. It could be shown that the diameter of the stationary collectors had a big impact on the morphology of the constructs. The bigger the diameter of the mandrel (smallest collector diameters 0.5 mm, biggest 4.8 mm) got, the more the shape of the generated footprint converged into a circular one known from flat collectors. In a second set of experiments the mandrels were only rotated. Increasing the rotational velocity from 4.2 to 42.0 rpm transformed the morphology of the constructs from a figure-of-eight pattern to a sinusoidal and ultimately to a straight fiber morphology. It was possible to prove that the transformation of the pattern was comparable to what was known from increasing the speed using flat collectors and that at a critical speed, the so called critical translation speed, straight fibers would appear that were precisely stacking on top of each other. By combining rotation and translation of the mandrel, it was possible to print tubular constructs with defined winding angles. Using

collections speeds close to the critical translation speed enabled higher control of fiber positioning and it was possible to generate precisely stacked constructs with winding angles between 5 and 60°.

In **Chapter 4** a different approach was followed. It was based on extrusion-based bioprinting in combination with a hydrogel ink system. The ink was loaded with nanoparticles and the nanoparticle release was analyzed. In other words, two systems, a printable polyglycidol/hyaluronic acid ink and mesoporous silica nanoparticles (MSN), were combined to analyze charge driven release mechanism that could be fine-tuned using bioprinting. Thorough rheological evaluations proved that the charged nanoparticles, both negatively charged MSN-COOH and positively charged MSN-NH_2, did not alter the shear thinning properties of the ink that revealed a negative base charge due to hyaluronic acid as one of its main components. Furthermore, it could be shown that the particles did also not have a negative effect on the recovery properties of the material after exposure to high shear. During printing, the observations made via rheological testing were supported by the fact that all materials could be printed at the same settings of the bioprinter. Using theses inks, it was possible to make constructs as big as 12x12x3 mm^3 composed of 16 layers. The fiber diameters produced were about 627±31 µm and two-component constructs could be realized utilizing the two hydrogel print heads of the printer to fabricate one hybrid construct. The particle distribution within those constructs was homogeneous, both from a microscopic and a macroscopic point of view. Particle release from printed constructs was tracked over 6 weeks and revealed that the print geometry had an influence on the particle release. Printed in a geometry with direct contact between the strands containing different MSN, the positively charged particles quickly migrated into the strand previously containing only negatively charged MSN-COOH. The MSN-COOH seemed to be rather released into the surrounding liquid and also after 6 weeks no MSN-COOH signal could be detected in the strand previously only containing MSN-NH_2. In case of a geometry without direct contact between the

strands, the migration of the positively charged nanoparticles into the MSN-COOH containing strand was strongly delayed. This proved that the architecture of the printed construct can be used to fine-tune the particle release from nanoparticle containing printable hydrogel ink systems.

Chapter 5 discusses an approach using hydrogel inks based on recombinant spider silk proteins processed via extrusion-based bioprinting. The ink could be applied for printing at protein concentrations of 3 % w/v without the addition of thickeners or any post process crosslinking. Both, the recombinant protein eADF4(C16) and a modification introducing a RGD-sequence to the protein (eADF4(C16)-RGD), could be printed revealing a very good print fidelity. The RGD modification had positive effect on the adhesion of cells seeded onto printed constructs. Furthermore, human fibroblasts encapsulated in the ink at concentrations of 1.2 million cells per mL did not alter the print fidelity and did not interfere with the crosslinking mechanism of the ink. This enabled printing cell laden constructs with a cell survival rate of 70.1±7.6 %. Although the cell survival rate needs to be improved in further trials, the approach shown is one of the first leading towards the shift of the window of biofabrication because it is based on a new material that does not need potentially harmful post-process crosslinking and allows the direct encapsulation of cells staying viable throughout the print process.

Chapter 6.2: Zusammenfassung

Die Biofabrikation ist ein junges und sehr dynamisches Forschungsgebiet mit viel Potential. Dieses Potential spiegelt sich unter anderem in den ambitionierten Zielen wieder, die man sich hier gesetzt hat. Wissenschaftler in diesem Gebiet wollen eines Tages beispielsweise funktionale menschliche Gewebe nachbilden, die aus patienteneigenen Zellen bestehen. Diese Gewebe sollen entweder für die Testung neuer Arzneimittel und Therapien oder sogar als Implantate einsetzt werden. Der Schlüssel zum Erfolg soll hier die Verwendung automatisierter Prozesse in Verbindung mit innovativen Materialien sein, die es ermöglichen, die Hierarchie und Funktion des zu ersetzenden natürlichen Gewebes nachbilden. Obwohl in den letzten Jahren große Fortschritte gemacht worden sind, gibt es immer noch Hürden, die überwunden werden müssen. **Ziel dieser Arbeit** war es deshalb, die derzeit eingeschränkte Auswahl kompatibler Materialien für die Biofabrikation zu erweitern und bereits etablierte Verfahren wie den extrusionsbasierten Biodruck noch besser verstehen zu lernen. Auch neue Verfahren, wie etwa das Melt Electrospinning Writing (MEW) sollten etabliert werden.

In **Kapitel 3** dieser Arbeit wurde das MEW dazu verwendet, tubuläre Strukturen zu fertigen, die sich aus Polymerfasern mit einem durchschnittlichen Durchmesser von nur etwa 12 µm zusammensetzen. Die mit Hilfe von Druckluft in Verbindung mit einer hohen elektrischen Spannung aus einer Nadelspitze austretende Polymerschmelze wurde hierbei auf zylinderförmigen Kollektoren mit Durchmessern zwischen 0.5 und 4.8 mm gesammelt. Auf diese Weise wurden röhrenförmige Faserkonstrukte generiert. Das Hauptaugenmerk lag auf dem Einfluss des Durchmessers, der Rotations- und Translationsbewegung des Kollektors auf die Morphologie der Faserkonstrukte. Hierzu wurden die Fasern erst auf unbewegten Kollektoren mit unterschiedlichen Durchmessern gesammelt und die entstehenden Muster analysiert. Es zeigte sich, dass das Fasermuster mit zunehmendem Durchmesser des Kollektors mehr den symmetrischen Konstrukten mit runder Grundfläche glich, die auch von

flachen Kollektoren bekannt sind. Je kleiner der Kollektordurchmesser wurde, desto ovaler wurde die Grundfläche der Muster, was den Einfluss der Krümmung deutlich machte. In weiteren Experimenten wurden die zylindrischen Kollektoren mit Geschwindigkeiten von 4,2 bis 42 Umdrehungen pro Minute um ihre Längsachse gedreht. Die von flachen Kollektoren bekannten Übergänge der Fasermorphologie konnten auch für runde Kollektoren bestätigt werden. So änderte sich die Morphologie mit zunehmender Geschwindigkeit der Oberfläche von einer achterförmigen Gestalt über eine sinusförmige Ausrichtung der Fasern hin zu einer geraden Linie. Der Einfluss des Kollektordurchmessers wurde auch hier deutlich, da sich etwa die Amplitude der bei Rotationsgeschwindigkeiten im Bereich sinusförmiger Ausrichtung abgelegten Fasern mit abnehmendem Radius erhöhte. Im nächsten Schritt wurde neben der Rotation der Kollektoren auch eine Translation induziert. Durch geeignete Kombination von Rotation und Translation konnten Konstrukte mit definiertem Wickelwinkel hergestellt werden. Es zeigte sich, dass die Wiedergabe des vorher kalkulierten Winkels unter Verwendung von Oberflächengeschwindigkeiten, die nahe am Übergang zur geraden Faserausrichtung waren, am besten war. Im Rahmen dieser Arbeit konnten Winkel zwischen 5 und 60° mit hoher Präzision wiedergegeben werden. Im Falle von sich wiederholenden Mustern konnte auch in Bezug auf die Stapelbarkeit der Fasern aufeinander eine hohe Präzision erreicht werden.

Kapitel 4 dieser Arbeit befasste sich mit dem extrusionsbasierten 3D-Druck. Das etabliere Verfahren wurde auf eine bisher wenig untersuchte Materialzusammensetzung von Nanopartikeln-beladenen Hydrogeltinten ausgeweitet. Die Tinte bestand aus einer Kombination von funktionalisierten Polyglyzidolen und einer unmodifizierten langkettingen Hyaluronsäure. Dieser wurden mesoporöse Silika-Nanopartikel mit unterschiedlicher Ladung zugesetzt und deren Freisetzung aus gedruckten Konstrukten mit einstellbarer Geometrien untersucht. Da die Hyaluronsäure selbst negativ geladen ist, wurde erwartet und auch

gezeigt, dass aminofunktionalisierte Partikel mit positiver Ladung langsamer freigesetzt werden als carboxylfunktionalisierte Partikel mit negativer Ladung. Interessanterweise änderten die Partikel nicht die rheologischen Eigenschaften der Tinte und es konnten Hydrogele, die mit positiv geladenen Partikeln beladen waren, bei den gleichen Druckparametern verdruckt werden, wie Hydrogele, die mit negativ geladenen Partikeln beladen waren. Die guten Druckeigenschaften der Tinten ermöglichten die präzise Fertigung von Konstrukten mit einer Größe von 12x12x3 mm^3, also von Konstrukten mit bis zu 16 aufeinanderfolgenden Lagen. Die Strangdurchmesser betrugen hierbei 627±31 µm und die Verteilung der Partikel innerhalb der Stränge war sehr homogen. Zudem konnten auch Strukturen gedruckt werden, bei denen beide Tintenarten, mit positiven und mit negativen Partikeln beladene Hydrogele, in einem Konstrukt kombiniert wurden. Hierbei zeigte sich, dass die Freisetzung der Partikel, die über 6 Wochen hinweg untersucht wurde, auch stark von der Geometrie der zwei-Komponenten-Konstrukte abhing. Insbesondere die Auswirkung des direkten Kontakts zwischen den Komponenten innerhalb eines Konstruktes war hier sehr deutlich. Wurden die Stränge über Kreuz aufeinander abgelegt und hatten direkten Kontakt an den Kreuzungspunkten, konnte beobachtet werden, dass die positiv geladenen Partikel aus ihrem System in das mit den negativ geladenen Partikeln wanderten. Wurden die Stränge ohne direkten Kontakt parallel nebeneinander abgelegt, wurden die positiv geladenen Partikel in umgebendes Medium freigesetzt, konnten aber selbst nach 6 Wochen nicht in den Strängen mit den negativ geladenen Partikeln nachgewiesen werden. Dies verdeutlicht, dass Geometrie und Ladung der Partikel einen Einfluss auf die Freisetzung der Partikel hatten und sich die Freisetzung der Partikel durch eine geschickte Kombination beider Parameter steuern lässt.

In Kapitel 5 dieser Arbeit wurde eine neue Materialklasse als Biotinte für den extrusionsbasierten Biodruck untersucht. Bei dem Material handelte es sich um Hydrogele auf Basis rekombinanter Spinnenseidenproteine. Diese konnten ab einer

Proteinkonzentration von 3 % Gew./Vol. ohne die Verwendung von Verdickungsmittel oder anderen Additiven und auch ohne eine nachträgliche Vernetzung verdruckt werden. Sowohl Hydrogele auf Basis des rekombinanten Proteins eADF4(C16) als auch eine mit einer RGD-Sequenz versehene Modifikation (eADF4(C16)-RGD) konnten mit einer hohen Formtreue verdruckt werden. Die RGD-Sequenz zeigte einen positiven Effekt auf das Anhaften von humanen Fibroblasten, die auf gedruckte Konstrukte ausgesät wurden. Zudem konnten mit Hilfe der Hydrogele auch zellbeladene Konstrukte gefertigt werden. Hierzu wurden die Hydrogele mit einer Zellsuspension so vermengt, dass eine finale Konzentration von 1,2 Millionen Zellen/ml erreicht wurde. Die beladenen Gele wurden verdruckt und es konnte eine Überlebensrate von 70,1±7,6 % nachgewiesen werden. Das in diesem Kapitel etablierte Materialsystem ermöglichte zum ersten Mal das Verdrucken lebender Zellen in einer neuen Klasse von Tinten, die weder die Beimengung von Verdickungsmittel noch einen zusätzlichen Nachhärtungsschritt für die Herstellung zellbeladener stabiler Konstrukte benötigt.

Acknowledgments

This thesis could not have been realized without the help of my colleagues, friends, and my family.

First, I would like to thank my supervisor Prof. Dr. Jürgen Groll for his great support during my thesis and beyond. It was a pleasure working in the highly productive environment you generated for the students. I got the chance to expand my skillset in a multidisciplinary chair and was also able to learn from your experience during many meetings and discussions. Due to your network, I was able to connect with and meet many interesting people. Furthermore, I got the chance to visit a broad range of labs and conferences and attend diverse meetings with industry and university delegates. Your fair mentoring in combination with the trust you put in my decisions and actions excellently prepared me for future challenges.

Thanks to Prof. Dr. Paul Dalton who gave me the opportunity to gain experience in the labs of QUT. It was excellent to discuss scientific and future directions getting great support at each level of my thesis. Also working with you at FMZ helped me to learn approaching problems from different perspectives. I enjoyed getting to know your visionary character and would like to thank you for your constant support.

Jörg Teßmar, it was a pleasure to work and share scientific questions with you. Your meticulous and organized way of solving problems shaped my own approach towards new problems and questions. The support I got was always appreciated and far beyond any possible expectations. Thanks!

During my thesis I had the chance to work on different topics and was very lucky to have great collaboration partners which significantly contributed to this thesis. Thanks to Marko, Urip, Anjali, and Prof. Dr. Dietmar W. Hutmacher for the great time and working environment I had in Brisbane. Thanks to Kristin and Prof. Dr. Thomas Scheibel for the collaboration and for everything I got to learn about recombinant spider silk proteins. Thank you Bernhard and Prof. Dr. Mika Lindén for the collaboration and for introducing me to the field of mesoporous silica nanoparticles.

Acknowledgments

The support and the great working environment at FMZ also played a crucial role in this thesis. Without the support, both professional and private, I would not have been able to enjoy my PhD so much and to be as productive. EVERYONE contributed to this thesis in one or the other way and thus I would like to thank the whole department and everyone I got to know and worked with! Nevertheless, I would like to point out some special individuals. Prof. Dr. Uwe Gbureck already supported me during my master thesis at FMZ and never stopped doing that during my time at FMZ. Thanks for your help on a professional and a private level. I would also like to point out Harald and Toni from the workshop where I spend hours, days or even month discussing and designing MEW devices and test setups. Only due to your experience - and maybe also the continuous coffee supply, you always provided ☺ – the machines and thus this work could be realized. Isabell, Simone, and Andrea, your support in the lab and around the lab was always highly appreciated. Thank you very much. During my time at FMZ I not only had the opportunity to work with excellent colleagues but also made friends I will remember for the rest of my live. Michael, Steffi, Kai, Tobi, Ilona, Matthias, Ana, and Martha: I don´t think I need to mention that I always enjoy the time with you and that you had a major impact on the work and on my character. Thanks for your never-ending support and for the unforgettable memories we share. Furthermore, I would like to thank the people I got to meet closer towards the end of my thesis. Willi, Julia, Gernot, Simone, Susanne, Laura, Sarah, Carina, Andrei, Moataz, and Johannes: Thank you for the collaboration and the open-minded exchange of ideas and experience.

Last but definitely not least, I would also like to thank the people I do not share professional experience with. Your support, especially during difficult times, was a basis for the success of this thesis. Sorry for the many hours you had to deal with my bad mood caused by failed experiments and thank you for being able to cheer me up. Thanks for the trust in me and for always being there to support me. Thank you, Julia, Sabine, Papa, Mama, Paul, Ela, Julian, and Lea!

References

(1) Ligon, S. C.; Liska, R.; Stampfl, J.; Gurr, M.; Mülhaupt, R. Polymers for 3D printing and customized additive manufacturing. *Chemical Reviews* **2017,** *117* (15), 10212-10290.

(2) Berman, B. 3D printing: The new industrial revolution. *Business Horizons* **2012,** *55* (2), 155-162.

(3) http://www.eos.info/presse/kundenrefe-renzen/Hueftimplantat-_additi-_gefertigt, 2018; Accessed: 04.01.2018.

(4) Murphy, S. V.; Atala, A. 3D bioprinting of tissues and organs. *Nature Biotechnology* **2014,** *32* (8), 773-785.

(5) Groll, J.; Boland, T.; Blunk, T.; Burdick, J. A.; Cho, D.-W.; Dalton, P. D.; Derby, B.; Forgacs, G.; Li, Q.; Mironov, V. A. et al. Biofabrication: Reappraising the definition of an evolving field. *Biofabrication* **2016,** *8* (1), 013001.

(6) Brown, T. D.; Slotosch, A.; Thibaudeau, L.; Taubenberger, A.; Loessner, D.; Vaquette, C.; Dalton, P. D.; Hutmacher, D. W. Design and fabrication of tubular scaffolds via direct writing in a melt electrospinning mode. *Biointerphases* **2012,** *7* (1-4), 1-16.

(7) Buenger, D.; Topuz, F.; Groll, J. Hydrogels in sensing applications. *Progress in Polymer Science* **2012,** *37* (12), 1678-1719.

(8) Mamaeva, V.; Niemi, R.; Beck, M.; Ozliseli, E.; Desai, D.; Landor, S.; Gronroos, T.; Kronqvist, P.; Pettersen, I. K.; McCormack, E.et al. Inhibiting notch activity in breast cancer stem cells by glucose functionalized nanoparticles carrying gamma-secretase inhibitors. *Molecular Therapy* **2016,** *24* (5), 926-936.

(9) Vendrely, C.; Scheibel, T. Biotechnological production of spider-silk proteins enables new applications. *Macromolecular Bioscience* **2007,** *7* (4), 401-409.

(10) Mironov, V.; Trusk, T.; Kasyanov, V.; Little, S.; Swaja, R.; Markwald, R. Biofabrication: A 21st century manufacturing paradigm. *Biofabrication* **2009,** *1* (2), 022001.

(11) Hutmacher, D. Additive manufacturing applied in the biomedical sciences-bioprinting, biofabrication, cell printing....? The need for definitions & norms. *Tissue Engineering Part A* **2015,** *21*, S10-S10.

(12) Guillemot, F.; Mironov, V.; Nakamura, M. Bioprinting is coming of age: Report from the international conference on bioprinting and biofabrication in bordeaux (3b'09). *Biofabrication* **2010,** *2* (1), 010201.

(13) Schon, B. S.; Hooper, G. J.; Woodfield, T. B. Modular tissue assembly strategies for biofabrication of engineered cartilage. *Annals of Biomedical Engineering* **2017**, *45* (1), 100-114.

(14) Hochleitner, G.; Jungst, T.; Brown, T. D.; Hahn, K.; Moseke, C.; Jakob, F.; Dalton, P. D.; Groll, J. Additive manufacturing of scaffolds with sub-micron filaments via melt electrospinning writing. *Biofabrication* **2015,** *7* (3), 035002.

(15) Brown, T. D.; Dalton, P. D.; Hutmacher, D. W. Melt electrospinning today: An opportune time for an emerging polymer process. *Progress in Polymer Science* **2016,** *56*, 116-166.

(16) Hochleitner, G.; Hümmer, J. F.; Luxenhofer, R.; Groll, J. High definition fibrous poly(2-ethyl-2-oxazoline) scaffolds through melt electrospinning writing. *Polymer* **2014,** *55* (20), 5017-5023.

(17) Dalton, P. D.; Klinkhammer, K.; Salber, J.; Klee, D.; Möller, M. Direct in vitro electrospinning with polymer melts. *Biomacromolecules* **2006,** *7* (3), 686-690.

(18) Jungst, T.; Muerza-Cascante, M. L.; Brown, T. D.; Standfest, M.; Hutmacher, D. W.; Groll, J.; Dalton, P. D. Melt electrospinning onto cylinders: Effects of rotational velocity and collector diameter on morphology of tubular structures. *Polymer International* **2015,** *64* (9), 1086-1095.

(19) Thibaudeau, L.; Taubenberger, A. V.; Holzapfel, B. M.; Quent, V. M.; Fuehrmann, T.; Hesami, P.; Brown, T. D.; Dalton, P. D.; Power, C. A.; Hollier, B. G.et al. A tissue-engineered humanized xenograft model of human breast cancer metastasis to bone. *Disease Models & Mechanisms* **2014,** *7* (2), 299-309.

(20) Dasdemir, M.; Topalbekiroglu, M.; Demir, A. Electrospinning of thermoplastic polyurethane microfibers and nanofibers from polymer solution and melt. *Journal of Applied Polymer Science* **2012,** *127* (3), 1901-1908.

(21) Nagy, Z. K.; Balogh, A.; Dravavolgyi, G.; Ferguson, J.; Pataki, H.; Vajna, B.; Marosi, G. Solvent-free melt electrospinning for preparation of fast dissolving drug delivery system and comparison with solvent-based electrospun and melt extruded systems. *Journal of Pharmaceutical Sciences* **2012,** *102* (2), 508-517.

(22) Mota, C.; Puppi, D.; Gazzarri, M.; Bártolo, P.; Chiellini, F. Melt electrospinning writing of three-dimensional star poly(ϵ-caprolactone) scaffolds. *Polymer International* **2013,** *62* (6), 893-900.

(23) Mazalevska, O.; Struszczyk, M. H.; Krucinska, I. Design of vascular prostheses by melt electrospinning-structural characterizations. *Journal of Applied Polymer Science* **2012,** *129* (2), 779-792.

(24) Dalton, P. D.; Joergensen, N. T.; Groll, J.; Moeller, M. Patterned melt electrospun substrates for tissue engineering. *Biomedical Materials* **2008,** *3* (3), 034109.

(25) Detta, N.; Brown, T. D.; Edin, F. K.; Albrecht, K.; Chiellini, F.; Chiellini, E.; Dalton, P. D.; Hutmacher, D. W. Melt electrospinning of polycaprolactone and its blends with poly(ethylene glycol). *Polymer International* **2010,** *59* (11), 1558-1562.

(26) Darby, R. *Chemical engineering fluid mechanics*; 2 ed.; Marcel Dekker Inc.: New York, 2001.

(27) Fang, J.; Zhang, L.; Sutton, D.; Wang, X.; Lin, T. Needleless melt-electrospinning of polypropylene nanofibres. *Journal of Nanomaterials* **2012,** *2012*, 1-9.

(28) Hacker, C.; Jungbecker, P.; Silk, G.; Gries, T.; Thomas, H.; Möller, M. Electrospinning of polymer melt: Steps toward an upscaled multi-jet process. *Proceedings of the International Conference on Latest Advances in High Tech Textiles and Textile-Based Materials* **2009**, 71-76.

(29) Collins, G.; Federici, J.; Imura, Y.; Catalani, L. H. Charge generation, charge transport, and residual charge in the electrospinning of polymers: A review of issues and complications. *Journal of Applied Physics* **2012,** *111* (4), 044701.

(30) Taylor, G. Electrically driven jets. *Proceedings of the Royal Society of London A: Mathematical, Physical and Engineering Sciences* **1969,** *313* (1515), 453-475.

(31) Jain, E.; Scott, K. M.; Zustiak, S. P.; Sell, S. A. Fabrication of polyethylene glycol-based hydrogel microspheres through electrospraying. *Macromolecular Materials and Engineering* **2015,** *300* (8), 823-835.

(32) Li, D.; Xia, Y. N. Electrospinning of nanofibers: Reinventing the wheel? *Advanced Materials* **2004,** *16* (14), 1151-1170.

(33) Ramakrishna, S.; Fujihara, K.; Teo, W.-E.; Lim, T.-C.; Ma, Z. *An introduction to electrospinning and nanofibers*; World Scientific, 2005.

(34) Lyons, J.; Ko, F. Feature article: Melt electrospinning of polymers: A review. *Polymer News* **2005,** *30* (6), 170-178.

(35) Hochleitner, G.; Youssef, A.; Hrynevich, A.; Haigh, J. N.; Jungst, T.; Groll, J.; Dalton, P. D. Fibre pulsing during melt electrospinning writing. *BioNanoMaterials* **2016,** *17* (3-4), 159-171.

(36) Brown, T. D.; Edin, F.; Detta, N.; Skelton, A. D.; Hutmacher, D. W.; Dalton, P. D. Melt electrospinning of poly(ϵ-caprolactone) scaffolds: Phenomenological observations associated with collection and direct writing. *Materials Science & Engineering C: Materials for Biological Applications* **2014,** *45*, 698-708.

(37) Brun, P. T.; Audoly, B.; Ribe, N. M.; Eaves, T. S.; Lister, J. R. Liquid ropes: A geometrical model for thin viscous jet instabilities. *Physical Review Letters* **2015,** *114* (17), 174501.

(38) Brown, T. D.; Dalton, P. D.; Hutmacher, D. W. Direct writing by way of melt electrospinning. *Advanced Materials* **2011,** *23* (47), 5651-5657.

(39) Jungst, T.; Smolan, W.; Schacht, K.; Scheibel, T.; Groll, J. Strategies and molecular design criteria for 3D printable hydrogels. *Chemical Reviews* **2016,** *116* (3), 1496-1539.

(40) Skardal, A.; Atala, A. Biomaterials for integration with 3D bioprinting. *Annals of Biomedical Engineering* **2015**, *43* (3), 730-746.

(41) Lim, K. S.; Schon, B. S.; Mekhileri, N. V.; Brown, G. C. J.; Chia, C. M.; Prabakar, S.; Hooper, G. J.; Woodfield, T. B. F. New visible-light photoinitiating system for improved print fidelity in gelatin-based bioinks. *ACS Biomaterials Science & Engineering* **2016**, *2* (10), 1752-1762.

(42) Stichler, S.; Jungst, T.; Schamel, M.; Zilkowski, I.; Kuhlmann, M.; Bock, T.; Blunk, T.; Tessmar, J.; Groll, J. Thiol-ene clickable poly(glycidol) hydrogels for biofabrication. *Annals of Biomedical Engineering* **2017,** *45* (1), 273-285.

(43) Stichler, S.; Bock, T.; Paxton, N.; Bertlein, S.; Levato, R.; Schill, V.; Smolan, W.; Malda, J.; Tessmar, J.; Blunk, T.et al. Double printing of hyaluronic acid/poly(glycidol) hybrid hydrogels with poly(epsilon-caprolactone) for msc chondrogenesis. *Biofabrication* **2017,** *9* (4), 044108.

(44) Ozbolat, I. T.; Hospodiuk, M. Current advances and future perspectives in extrusion-based bioprinting. *Biomaterials* **2015,** *76*, 321-343.

(45) Landers, R., Albert-Ludwigs-Universität Freiburg i. Br., 2004.

(46) Ozbolat, I. T.; Chen, H.; Yu, Y. Development of 'multi-arm bioprinter' for hybrid biofabrication of tissue engineering constructs. *Robotics and Computer-Integrated Manufacturing* **2014,** *30* (3), 295-304.

(47) Chung, J. H. Y.; Naficy, S.; Yue, Z. L.; Kapsa, R.; Quigley, A.; Moulton, S. E.; Wallace, G. G. Bio-ink properties and printability for extrusion printing living cells. *Biomaterials Science* **2013,** *1* (7), 763-773.

(48) Ahn, S.; Lee, H.; Puetzer, J.; Bonassar, L. J.; Kim, G. Fabrication of cell-laden three-dimensional alginate-scaffolds with an aerosol cross-linking process. *Journal of Materials Chemistry* **2012,** *22* (36), 18735.

(49) Rowley, J. A.; Madlambayan, G.; Mooney, D. J. Alginate hydrogels as synthetic extracellular matrix materials. *Biomaterials* **1999,** *20* (1), 45-53.

(50) Pereira, R. F.; Bártolo, P. J. 3D bioprinting of photocrosslinkable hydrogel constructs. *Journal of Applied Polymer Science* **2015,** *132* (48), 42458.

(51) Loessner, D.; Meinert, C.; Kaemmerer, E.; Martine, L. C.; Yue, K.; Levett, P. A.; Klein, T. J.; Melchels, F. P.; Khademhosseini, A.; Hutmacher, D. W. Functionalization, preparation and use of cell-laden gelatin methacryloyl-based

hydrogels as modular tissue culture platforms. *Nature Protocols* **2016,** *11* (4), 727-746.

(52) Schuurman, W.; Levett, P. A.; Pot, M. W.; van Weeren, P. R.; Dhert, W. J. A.; Hutmacher, D. W.; Melchels, F. P. W.; Klein, T. J.; Malda, J. Gelatin-methacrylamide hydrogels as potential biomaterials for fabrication of tissue-engineered cartilage constructs. *Macromolecular Bioscience* **2013,** *13* (5), 551-561.

(53) Melchels, F. P. W.; Dhert, W. J. A.; Hutmacher, D. W.; Malda, J. Development and characterisation of a new bioink for additive tissue manufacturing. *Journal of Materials Chemistry B* **2014,** *2* (16), 2282-2289.

(54) Kang, H. W.; Lee, S. J.; Ko, I. K.; Kengla, C.; Yoo, J. J.; Atala, A. A 3D bioprinting system to produce human-scale tissue constructs with structural integrity. *Nature Biotechnology* **2016,** *34* (3), 312-319.

(55) Strobl, G. R. *The physics of polymers*; Springer: Berlin, 2007.

(56) Rubinstein, M.; Colby, R. H. *Polymers physics*; Oxford University Press: Oxford, 2003.

(57) Shenoy, A. V. *Rheology of filled polymer systems*; Kluwer Academic Publishers: Dordrecht, 1999.

(58) Barnes, H. A.; Hutton, J. F.; Walters, K. *An introduction to rheology*; Elsevier: Amsterdam, 1989.

(59) Bird, R. B.; Armstrong, R. C.; Hassager, O. *Dynamics of polymeric liquids*; John Willey & Sons: New York, 1987.

(60) Ferry, J. D. *Viscoelastic properties of polymers*; John Wiley & Sons: New York, 1980.

(61) Mewis, J.; Wagner, N. J. Thixotropy. *Advances in Colloid and Interface Science* **2009,** *147-148*, 214-227.

(62) Barnes, H. A. Thixotropy - a review. *Journal of Non-Newtonian Fluid Mechanics* **1997,** *70* (1), 1-33.

(63) Yan, K. C.; Nair, K.; Sun, W. Three dimensional multi-scale modelling and analysis of cell damage in cell-encapsulated alginate constructs. *Journal of Biomechanics* **2010,** *43* (6), 1031-1038.

(64) Aguado, B. A.; Mulyasasmita, W.; Su, J.; Lampe, K. J.; Heilshorn, S. C. Improving viability of stem cells during syringe needle flow through the design of hydrogel cell carriers. *Tissue Engineering, Part A* **2012,** *18* (7-8), 806-815.

(65) Lewis, J. A. Colloidal processing of ceramics. *Journal of the American Ceramic Society* **2000,** *83* (10), 2341-2359.

(66) Macosko, C. W. *Rheology: Principles, measurements, and applications*; Wiley-VCH: New York, 1994.

(67) Mewis, J.; Wagner, N. J. *Colloidal suspension rheology*; Cambridge University Press: Cambridge, 2012.

(68) Krieger, I. M. Rheology of monodisperse latices. *Advances in Colloid and Interface Science* **1972,** *3* (2), 111-136.

(69) Goodwin, J. W.; Hughes, R. W. *Rheology for chemists: An introduction*; Royal Society of Chemistry: Cambridge, 2000.

(70) Bergenholtz, J. Theory of rheology of colloidal dispersions. *Current opinion in colloid & interface science* **2001,** *6* (5), 484-488.

(71) Lewis, J. A. Direct-write assembly of ceramics from colloidal inks. *Current Opinion in Solid State and Materials Science* **2002,** *6* (3), 245-250.

(72) Ahn, B. Y.; Shoji, D.; Hansen, C. J.; Hong, E.; Dunand, D. C.; Lewis, J. A. Printed origami structures. *Advanced Materials* **2010,** *22* (20), 2251-2254.

(73) Ahn, B. Y.; Duoss, E. B.; Motala, M. J.; Guo, X.; Park, S.-I.; Xiong, Y.; Yoon, J.; Nuzzo, R. G.; Rogers, J. A.; Lewis, J. A. Omnidirectional printing of flexible, stretchable, and spanning silver microelectrodes. *Science* **2009,** *323* (5921), 1590-1593.

(74) Hanson Shepherd, J. N.; Parker, S. T.; Shepherd, R. F.; Gillette, M. U.; Lewis, J. A.; Nuzzo, R. G. 3D microperiodic hydrogel scaffolds for robust neuronal cultures. *Advanced Functional Materials* **2011,** *21* (1), 47-54.

(75) Smay, J. E.; Gratson, G. M.; Shepherd, R. F.; Cesarano, J.; Lewis, J. A. Directed colloidal assembly of 3D periodic structures. *Advanced Materials* **2002,** *14* (18), 1279-1283.

(76) Schmid-Schönbein, H.; Wells, R.; Goldstone, J. Influence of deformability of human red cells upon blood viscosity. *Circulation Research* **1969,** *25* (2), 131-143.

(77) Winkler, R. G.; Fedosov, D. A.; Gompper, G. Dynamical and rheological properties of soft colloid suspensions. *Current opinion in colloid & interface science* **2014,** *19* (6), 594-610.

(78) Vlassopoulos, D.; Cloitre, M. Tunable rheology of dense soft deformable colloids. *Current opinion in colloid & interface science* **2014,** *19* (6), 561-574.

(79) Singh, S. P.; Chatterji, A.; Gompper, G.; Winkler, R. G. Dynamical and rheological properties of ultrasoft colloids under shear flow. *Macromolecules* **2013,** *46* (19), 8026-8036.

(80) Huang, C.-C.; Winkler, R. G.; Sutmann, G.; Gompper, G. Semidilute polymer solutions at equilibrium and under shear flow. *Macromolecules* **2010,** *43* (23), 10107-10116.

(81) Huang, C. C.; Sutmann, G.; Gompper, G.; Winkler, R. G. Tumbling of polymers in semidilute solution under shear flow. *EPL (Europhysics Letters)* **2011,** *93* (5), 54004.

(82) Huber, B.; Harasim, M.; Wunderlich, B.; Kröger, M.; Bausch, A. R. Microscopic origin of the non-newtonian viscosity of semiflexible polymer solutions in the semidilute regime. *ACS Macro Letters* **2014,** *3* (2), 136-140.

(83) De Gennes, P.; Leger, L. Dynamics of entangled polymer chains. *Annual Review of Physical Chemistry* **1982,** *33* (1), 49-61.

(84) Watanabe, H. Viscoelasticity and dynamics of entangled polymers. *Progress in Polymer Science* **1999,** *24* (9), 1253-1403.

(85) Larson, R. G.; Desai, P. S. Modeling the rheology of polymer melts and solutions. *Annual Review of Fluid Mechanics* **2015,** *47* (1), 47-65.

(86) Raimondi, M. T.; Eaton, S. M.; Nava, M. M.; Laganà, M.; Cerullo, G.; Osellame, R. Two-photon laser polymerization: From fundamentals to biomedical application in tissue engineering and regenerative medicine. *Journal of Applied Biomaterials & Biomechanics* **2012,** *10*, 55-65.

(87) Wust, S.; Muller, R.; Hofmann, S. Controlled positioning of cells in biomaterials-approaches towards 3D tissue printing. *Journal of Functional Biomaterials* **2011,** *2* (3), 119-154.

(88) Melchels, F. P.; Feijen, J.; Grijpma, D. W. A review on stereolithography and its applications in biomedical engineering. *Biomaterials* **2010,** *31* (24), 6121-6130.

(89) Chrisey, D. B.; Pique, A.; McGill, R.; Horwitz, J.; Ringeisen, B.; Bubb, D.; Wu, P. Laser deposition of polymer and biomaterial films. *Chemical Reviews* **2003,** *103* (2), 553-576.

(90) Ringeisen, B. R.; Othon, C. M.; Barron, J. A.; Young, D.; Spargo, B. J. Jet-based methods to print living cells. *Biotechnology Journal* **2006,** *1* (9), 930-948.

(91) Schiele, N. R.; Corr, D. T.; Huang, Y.; Raof, N. A.; Xie, Y.; Chrisey, D. B. Laser-based direct-write techniques for cell printing. *Biofabrication* **2010,** *2* (3), 032001.

(92) Gruene, M.; Pflaum, M.; Hess, C.; Diamantouros, S.; Schlie, S.; Deiwick, A.; Koch, L.; Wilhelmi, M.; Jockenhoevel, S.; Haverich, A. Laser printing of three-dimensional multicellular arrays for studies of cell–cell and cell–environment interactions. *Tissue Engineering, Part C: Methods* **2011,** *17* (10), 973-982.

(93) Guillemot, F.; Souquet, A.; Catros, S.; Guillotin, B.; Lopez, J.; Faucon, M.; Pippenger, B.; Bareille, R.; Remy, M.; Bellance, S.et al. High-throughput laser printing of cells and biomaterials for tissue engineering. *Acta Biomaterialia* **2010,** *6* (7), 2494-2500.

(94) Koch, L.; Deiwick, A.; Schlie, S.; Michael, S.; Gruene, M.; Coger, V.; Zychlinski, D.; Schambach, A.; Reimers, K.; Vogt, P. M.et al. Skin tissue generation by laser cell printing. *Biotechnology and Bioengineering* **2012,** *109* (7), 1855-1863.

(95) Michael, S.; Sorg, H.; Peck, C. T.; Koch, L.; Deiwick, A.; Chichkov, B.; Vogt, P. M.; Reimers, K. Tissue engineered skin substitutes created by laser-assisted bioprinting form skin-like structures in the dorsal skin fold chamber in mice. *PLoS One* **2013,** *8* (3), e57741.

(96) Nahmias, Y.; Schwartz, R. E.; Verfaillie, C. M.; Odde, D. J. Laser-guided direct writing for three-dimensional tissue engineering. *Biotechnology and Bioengineering* **2005,** *92* (2), 129-136.

(97) Koch, L.; Kuhn, S.; Sorg, H.; Gruene, M.; Schlie, S.; Gaebel, R.; Polchow, B.; Reimers, K.; Stoelting, S.; Ma, N.et al. Laser printing of skin cells and human stem cells. *Tissue Engineering, Part C: Methods* **2010,** *16* (5), 847-854.

(98) Barron, J. A.; Ringeisen, B. R.; Kim, H.; Spargo, B. J.; Chrisey, D. B. Application of laser printing to mammalian cells. *Thin Solid Films* **2004,** *453-454*, 383-387.

(99) Lin, Y.; Huang, G.; Huang, Y.; Tzeng, T. R. J.; Chrisey, D. Effect of laser fluence in laser‐assisted direct writing of human colon cancer cell. *Rapid Prototyping Journal* **2010,** *16* (3), 202-208.

(100) Ringeisen, B. R.; Kim, H.; Barron, J. A.; Krizman, D. B.; Chrisey, D. B.; Jackman, S.; Auyeung, R.; Spargo, B. J. Laser printing of pluripotent embryonal carcinoma cells. *Tissue Engineering* **2004,** *10* (3-4), 483-491.

(101) Barron, J. A.; Wu, P.; Ladouceur, H. D.; Ringeisen, B. R. Biological laser printing: A novel technique for creating heterogeneous 3-dimensional cell patterns. *Biomedical Microdevices* **2004,** *6* (2), 139-147.

(102) Catros, S.; Guillotin, B.; Bačáková, M.; Fricain, J.-C.; Guillemot, F. Effect of laser energy, substrate film thickness and bioink viscosity on viability of endothelial cells printed by laser-assisted bioprinting. *Applied Surface Science* **2011,** *257* (12), 5142-5147.

(103) Wilson, W. C., Jr.; Boland, T. Cell and organ printing 1: Protein and cell printers. *The Anatomical Record Part A: Discoveries in Molecular, Cellular, and Evolutionary Biology* **2003,** *272A* (2), 491-496.

(104) Boland, T.; Xu, T.; Damon, B.; Cui, X. Application of inkjet printing to tissue engineering. *Biotechnology Journal* **2006,** *1* (9), 910-917.

(105) Calvert, P. Inkjet printing for materials and devices. *Chemistry of Materials* **2001,** *13* (10), 3299-3305.

(106) de Gans, B. J.; Duineveld, P. C.; Schubert, U. S. Inkjet printing of polymers: State of the art and future developments. *Advanced Materials* **2004,** *16* (3), 203-213.

(107) Derby, B. Bioprinting: Inkjet printing proteins and hybrid cell-containing materials and structures. *Journal of Materials Chemistry* **2008,** *18* (47), 5717-5721.

(108) Derby, B. Inkjet printing of functional and structural materials: Fluid property requirements, feature stability, and resolution. *Annual Review of Materials Research* **2010,** *40* (1), 395-414.

(109) Martin, G. D.; Hoath, S. D.; Hutchings, I. M. Inkjet printing - the physics of manipulating liquid jets and drops. *Journal of Physics: Conference Series* **2008,** *105*, 012001.

(110) Saunders, R. E.; Derby, B. Inkjet printing biomaterials for tissue engineering: Bioprinting. *International Materials Reviews* **2014,** *59* (8), 430-448.

(111) Singh, M.; Haverinen, H. M.; Dhagat, P.; Jabbour, G. E. Inkjet printing-process and its applications. *Advanced Materials* **2010,** *22* (6), 673-685.

(112) Xu, T.; Jin, J.; Gregory, C.; Hickman, J. J.; Boland, T. Inkjet printing of viable mammalian cells. *Biomaterials* **2005,** *26* (1), 93-99.

(113) Setti, L.; Fraleoni-Morgera, A.; Ballarin, B.; Filippini, A.; Frascaro, D.; Piana, C. An amperometric glucose biosensor prototype fabricated by thermal inkjet printing. *Biosensors & Bioelectronics* **2005,** *20* (10), 2019-2026.

(114) Derby, B. Printing and prototyping of tissues and scaffolds. *Science* **2012,** *338* (6109), 921-926.

(115) Ferris, C. J.; Gilmore, K. G.; Wallace, G. G.; In het Panhuis, M. Biofabrication: An overview of the approaches used for printing of living cells. *Applied Microbiology and Biotechnolnology* **2013,** *97* (10), 4243-4258.

(116) Billiet, T.; Vandenhaute, M.; Schelfhout, J.; Van Vlierberghe, S.; Dubruel, P. A review of trends and limitations in hydrogel-rapid prototyping for tissue engineering. *Biomaterials* **2012,** *33* (26), 6020-6041.

(117) Malda, J.; Visser, J.; Melchels, F. P.; Juengst, T.; Hennink, W. E.; Dhert, W. J. A.; Groll, J.; Hutmacher, D. W. 25th anniversary article: Engineering hydrogels for biofabrication. *Advanced Materials* **2013,** *25* (36), 5011-5028.

(118) Chang, C. C.; Boland, E. D.; Williams, S. K.; Hoying, J. B. Direct-write bioprinting three-dimensional biohybrid systems for future regenerative

therapies. *Journal of Biomedical Materials Research, Part B: Applied Biomaterials* **2011,** *98* (1), 160-170.

(119) Dababneh, A. B.; Ozbolat, I. T. Bioprinting technology: A current state-of-the-art review. *Journal of Manufacturing Science and Engineering-Transactions of the ASME* **2014,** *136* (6), 061016.

(120) Ozbolat, I. T.; Yu, Y. Bioprinting toward organ fabrication: Challenges and future trends. *IEEE Transactions on Biomedical Engineering* **2013,** *60* (3), 691-699.

(121) Lewis, J. A. Direct ink writing of 3D functional materials. *Advanced Functional Materials* **2006,** *16* (17), 2193-2204.

(122) Hutmacher, D. W.; Woodfield, T. B.; Dalton, P. D. In *Tissue engineering*; 2 ed.; Elsevier: London, 2014.

(123) Hutmacher, D. W.; Woodfield, T. B.; Dalton, P. D.; Lewis, J. A. In *Tissue engineering*; 1 ed.; Academic Press: Burlington, 2008.

(124) Shoichet, M. S.; Gentile, F. T.; Winn, S. R. The use of polymers in the treatment of neurological disorders - a discussion emphasizing encapsulated cell therapy. *Trends in Polymer Science* **1995,** *3* (11), 374-380.

(125) Zheng, Y.; Chen, J.; Craven, M.; Choi, N. W.; Totorica, S.; Diaz-Santana, A.; Kermani, P.; Hempstead, B.; Fischbach-Teschl, C.; Lopez, J. A.et al. In vitro microvessels for the study of angiogenesis and thrombosis. *Proceedings of the National Academy of Sciences of the United States of America* **2012,** *109* (24), 9342-9347.

(126) Lynam, D.; Bednark, B.; Peterson, C.; Welker, D.; Gao, M.; Sakamoto, J. S. Precision microchannel scaffolds for central and peripheral nervous system repair. *Journal of Materials Science: Materials in Medicine* **2011,** *22* (9), 2119-2130.

(127) Tran, R. T.; Choy, W. M.; Cao, H.; Qattan, I.; Chiao, J.-C.; Ip, W. Y.; Yeung, K. W. K.; Yang, J. Fabrication and characterization of biomimetic multichanneled crosslinked-urethane-doped polyester tissue engineered nerve guides. *Journal of Biomedical Materials Research Part A* **2014,** *102* (8), 2793-2804.

(128) Lee, S. H.; Yoon, J. W.; Suh, M. H. Continuous nanofibers manufactured by electrospinning technique. *Macromolecular Research* **2002,** *10* (5), 282-285.

(129) Panseri, S.; Cunha, C.; Lowery, J.; Del Carro, U.; Taraballi, F.; Amadio, S.; Vescovi, A.; Gelain, F. Electrospun micro- and nanofiber tubes for functional nervous regeneration in sciatic nerve transections. *BMC Biotechnology* **2008,** *8*, 39.

(130) Dalton, P. D.; Shoichet, M. S. Creating porous tubes by centrifugal forces for soft tissue application. *Biomaterials* **2001,** *22* (19), 2661-2669.

(131) Koroleva, A.; Gill, A. A.; Ortega, I.; Haycock, J. W.; Schlie, S.; Gittard, S. D.; Chichkov, B. N.; Claeyssens, F. Two-photon polymerization-generated and micromolding-replicated 3D scaffolds for peripheral neural tissue engineering applications. *Biofabrication* **2012,** *4* (2), 025005.

(132) Yan, J.; Huang, Y.; Chrisey, D. B. Laser-assisted printing of alginate long tubes and annular constructs. *Biofabrication* **2013,** *5* (1), 015002.

(133) Cui, T.; Terlecki, R.; Atala, A. Tissue engineering in urethral reconstruction. *Archivos Espanoles De Urologia* **2014,** *67* (1), 29-34.

(134) Son, S.-R.; Franco, R.-A.; Bae, S.-H.; Min, Y.-K.; Lee, B.-T. Electrospun plga/gelatin fibrous tubes for the application of biodegradable intestinal stent in rat model. *Journal of Biomedical Materials Research Part B: Applied Biomaterials* **2013,** *101B* (6), 1095-1105.

(135) Hung, S.-H.; Chen, P.-Y.; Tai, C.-C.; Chou, C.-H.; Cheng, W.-L.; Tseng, H. Development of tracheal scaffolds using hybridization of plla coil skeleton and electrospun structures. *Journal of Medical and Biological Engineering* **2014,** *34* (3), 218-223.

(136) Atala, A.; Kasper, F. K.; Mikos, A. G. Engineering complex tissues. *Science Translational Medicine* **2012,** *4* (160), 160rv112-160rv112.

(137) Venkatraman, S.; Boey, F.; Lao, L. L. Implanted cardiovascular polymers: Natural, synthetic and bio-inspired. *Progress in Polymer Science* **2008,** *33* (9), 853-874.

(138) Berner, A.; Boerckel, J. D.; Saifzadeh, S.; Steck, R.; Ren, J.; Vaquette, C.; Zhang, J. Q.; Nerlich, M.; Guldberg, R. E.; Hutmacher, D. W.et al. Biomimetic tubular nanofiber mesh and platelet rich plasma-mediated delivery of bmp-7 for large bone defect regeneration. *Cell and Tissue Research* **2012,** *347* (3), 603-612.

(139) Dalton, P. D.; Mey, J. Neural interactions with materials. *Frontiers in Bioscience* **2009,** *14*, 769-795.

(140) Dahlin, R. L.; Kasper, F. K.; Mikos, A. G. Polymeric nanofibers in tissue engineering. *Tissue Engineering Part B: Reviews* **2011,** *17* (5), 349-364.

(141) Xu, C. Y.; Inai, R.; Kotaki, M.; Ramakrishna, S. Aligned biodegradable nanotibrous structure: A potential scaffold for blood vessel engineering. *Biomaterials* **2004,** *25* (5), 877-886.

(142) Subramanian, A.; Krishnan, U. M.; Sethuraman, S. Fabrication, characterization and in vitro evaluation of aligned plga-pcl nanofibers for neural regeneration. *Annals of Biomedical Engineering* **2012,** *40* (10), 2098-2110.

(143) Wang, H. B.; Mullins, M. E.; Cregg, J. M.; Hurtado, A.; Oudega, M.; Trombley, M. T.; Gilbert, R. J. Creation of highly aligned electrospun poly-l-lactic acid fibers for nerve regeneration applications. *Journal of Neural Engineering* **2009,** *6* (1), 016001.

(144) Sun, Z.; Deitzel, J. M.; Knopf, J.; Chen, X.; Gillespie, J. W., Jr. The effect of solvent dielectric properties on the collection of oriented electrospun fibers. *Journal of Applied Polymer Science* **2012,** *125* (4), 2585-2594.

(145) Kumbar, S. G.; James, R.; Nukavarapu, S. P.; Laurencin, C. T. Electrospun nanofiber scaffolds: Engineering soft tissues. *Biomedical Materials* **2008,** *3* (3), 034002.

(146) Xu, C. Y.; Inai, R.; Kotaki, M.; Ramakrishna, S. Electrospun nanofiber fabrication as synthetic extracellular matrix and its potential for vascular tissue engineering. *Tissue Engineering* **2004,** *10* (7-8), 1160-1168.

(147) Bashur, C. A.; Ramamurthi, A. Aligned electrospun scaffolds and elastogenic factors for vascular cell-mediated elastic matrix assembly. *Journal of Tissue Engineering and Regenerative Medicine* **2012,** *6* (9), 673-686.

(148) Cipitria, A.; Skelton, A.; Dargaville, T. R.; Dalton, P. D.; Hutmacher, D. W. Design, fabrication and characterization of pcl electrospun scaffolds-a review. *Journal of Materials Chemistry* **2011,** *21* (26), 9419-9453.

(149) Han, T.; Reneker, D. H.; Yarin, A. L. Buckling of jets in electrospinning. *Polymer* **2007,** *48* (20), 6064-6076.

(150) Wiltschka, O.; Böcking, D.; Miller, L.; Brenner, R. E.; Sahlgren, C.; Lindén, M. Preparation, characterization, and preliminary biocompatibility evaluation of particulate spin-coated mesoporous silica films. *Microporous and Mesoporous Materials* **2014,** *188*, 203-209.

(151) Ahlfeld, T.; Cidonio, G.; Kilian, D.; Duin, S.; Akkineni, A. R.; Dawson, J. I.; Yang, S.; Lode, A.; Oreffo, R. O. C.; Gelinsky, M. Development of a clay based bioink for 3D cell printing for skeletal application. *Biofabrication* **2017,** *9* (3), 034103.

(152) Gaharwar, A. K.; Avery, R. K.; Assmann, A.; Paul, A.; McKinley, G. H.; Khademhosseini, A.; Olsen, B. D. Shear-thinning nanocomposite hydrogels for the treatment of hemorrhage. *ACS Nano* **2014,** *8* (10), 9833-9842.

(153) Baumann, B.; Jungst, T.; Stichler, S.; Feineis, S.; Wiltschka, O.; Kuhlmann, M.; Linden, M.; Groll, J. Control of nanoparticle release kinetics from 3D printed hydrogel scaffolds. *Angewandte Chemie International Edition* **2017,** *56* (16), 4623-4628.

(154) Jia, J.; Richards, D. J.; Pollard, S.; Tan, Y.; Rodriguez, J.; Visconti, R. P.; Trusk, T. C.; Yost, M. J.; Yao, H.; Markwald, R. R.et al. Engineering alginate as bioink for bioprinting. *Acta Biomaterialia* **2014,** *10* (10), 4323-4331.

(155) Schacht, K.; Jungst, T.; Schweinlin, M.; Ewald, A.; Groll, J.; Scheibel, T. Biofabrication of cell-loaded 3D spider silk constructs. *Angewandte Chemie International Edition* **2015,** *54* (9), 2816-2820.

(156) Billiet, T.; Gevaert, E.; De Schryver, T.; Cornelissen, M.; Dubruel, P. The 3D printing of gelatin methacrylamide cell-laden tissue-engineered constructs with high cell viability. *Biomaterials* **2014,** *35* (1), 49-62.